

AN AGENT-BASED MODEL OF CRYOPROTECTANT  
EQUILIBRATION IN SECONDARY STAGE PREANTRAL  
OVARIAN FOLLICLES

A Thesis Submitted to the  
College of Graduate and Postdoctoral Studies  
in Partial Fulfillment of the Requirements  
for the degree of Master of Science  
in the Department of Biology  
University of Saskatchewan  
Saskatoon

By

Joseph E.S. Abrams

©Joseph E.S. Abrams, November 2021. All rights reserved. Unless otherwise noted,  
copyright of the material in this thesis belongs to the author.

## PERMISSION TO USE

In presenting this thesis in partial fulfilment of the requirements for a postgraduate degree from the University of Saskatchewan, I agree that the Libraries of this University may make it freely available for inspection. I further agree that permission for copying of this thesis in any manner, in whole or in part, for scholarly purposes may be granted by the professor or professors who supervised my thesis work or, in their absence, by the Head of the Department or the Dean of the College in which my thesis work was done. It is understood that any copying or publication or use of this thesis or parts thereof for financial gain shall not be allowed without my written permission. It is also understood that due recognition shall be given to me and to the University of Saskatchewan in any scholarly use which may be made of any material in my thesis.

Requests for permission to copy or to make other use of material in this thesis in whole or part should be addressed to:

Head of the Department of Biology  
Collaborative Science Research Building  
112 Science Place  
University of Saskatchewan  
Saskatoon, Saskatchewan S7N 5E2  
Canada

Or

Dean  
College of Graduate and Postdoctoral Studies  
University of Saskatchewan  
116 Thorvaldson Building, 110 Science Place  
Saskatoon, Saskatchewan S7N 5C9  
Canada

# ABSTRACT

Young cancer patients have limited options for fertility treatment when facing gonadotoxic treatment. One promising fertility treatment for young cancer patients is the cryopreservation of immature ovarian follicles followed by maturation and subsequent reimplantation. However, preantral ovarian follicles currently have lower post-thaw success rates compared to mature oocytes and embryos. Previous research suggests that damage to vital intercellular connections, Transzonal Projections (TZPs), occurs during the cryopreservation process and may account for the observed lower post-thaw success rate in this tissue. It is likely that cryoprotective agent (CPA) equilibration is the cryopreservation step during which TZP damage occurs. Constructing a biologically relevant model of CPA equilibration and the associated damage may allow for improved protocols as measured by increased post-thaw success rates. Agent-based models are a promising technique to capture steps in the cryopreservation process, such as CPA equilibration. In this thesis, I conducted a series of experiments with typical CPAs and nonpermeating solutes at different temperatures using preantral ovarian follicles from a non-human primate (Rhesus monkeys) to measure TZP damage. In these experiments, I also estimated relevant permeability parameters within the tissue. I found that the majority of TZP damage was likely the result of mechanical forces that occurred during the cell volume reduction phase of CPA equilibration. Furthermore, through these experiments, I demonstrate that for this tissue type, parameters collected either during monolayer or single-cell experiments can be used to construct full tissue models. Using the derived experimental parameters and available literature values, I constructed and validated a 3-D agent-based model to capture CPA equilibration in preantral ovarian follicles. My agent-based model utilizes parallel computing on an average desktop computer and allows for the rapid design and testing of CPA equilibration protocols. The model I constructed can account for both mechanical and toxic damage. Importantly, my model accurately captures the experimental damage to TZPs in the majority of simulations. Lastly, I propose several theoretically improved cryopreservation protocols for preantral ovarian follicles. The research presented in this thesis demonstrates that agent-based models can be utilized to capture steps in the cryopreservation *in silico* and represents a non-invasive, less costly means to test and improve CPA equilibration protocols.

# ACKNOWLEDGEMENTS

First and foremost, I would like to thank Dr. James Benson for being a teacher and mentor as well as a supervisor. I would also like to thank Dr. Mary Zelinski, Dr. Alison Ting, and Jessica Stanley for providing me with experimental data, fielding a ton of questions, and offering me great insight into ovarian tissue preservation. I want to thank my committee members Dr. Tracy Marchant and Dr. Chris Soteris, for their excellent questions, comments, and feedback and for tolerating my occasional long-windedness. I want to thank Dr. Paul Macklin and Dr. Randy Heiland for their help with PhysiCell and their hospitality online and in person. Additionally, I would like to thank the Benson lab group, particularly Frankie Tu and Dominick Olver, who helped me do the first pass of cell-circling, a trial by fire. I would also like to thank Dr. Robyn Shuttleworth for her invaluable editing and help with Latex. I want to thank Dr. Maajid Bhat, who taught me invaluable lab skills. I want to thank Dr. Corinna Kashuba, Dr. Kurtis Swekla, and all the students with the veterinary department who taught a “physics and math guy” skills he never anticipated needing. I want to thank Breanne Bevelander, who helped me by doing yet more cell circling. Additionally, I would like to thank the funding agencies who made this research possible, the NIH and NSERC. I would also like to acknowledge biorender.com and inkscape which I used extensively in creating several of the figures for this thesis.

I would also like to thank my friends at the U of S who have been a font of joy and several of whom have helped with this project by listening to presentations or editing drafts. I would also like to thank my mother, Tobi Abrams, and my late father, Jack Abrams, who instilled a lifelong love of math and science and let me blow all my bar mitzvah money on an IBM Aptiva where I first learned to code. Lastly, I would be remiss if I did not thank my partner Deborah Hawkshaw. I could not have done this without your love, support, and tireless editing. I love you very much. Thank you, everyone.

This thesis is dedicated to my family, for those who are still here and those who are gone.

# CONTENTS

<b>Permission to Use</b>	<b>i</b>
<b>Abstract</b>	<b>ii</b>
<b>Acknowledgements</b>	<b>iii</b>
<b>Contents</b>	<b>v</b>
<b>List of Tables</b>	<b>vii</b>
<b>List of Figures</b>	<b>viii</b>
<b>List of Abbreviations</b>	<b>x</b>
<b>1 General Introduction</b>	<b>1</b>
1.1 Chapter Overview	1
1.2 Cryopreservation: an overview	1
1.3 Cryopreservation induced damage	4
1.4 Mass Transport	6
1.5 Vitrification	7
1.6 Modeling in cryopreservation	9
1.7 A Brief Overview of Agent-Based Modeling	11
1.8 Preantral Ovarian Follicles	14
1.9 Purpose and Objectives	17
1.10 Thesis Structure	17
<b>2 Experimental Determination of Model Parameters</b>	<b>19</b>
2.1 Chapter Overview	19
2.2 Introduction	19
2.3 Hypothesis	25
2.4 Materials and Methods	26
2.4.1 Animals and Tissue Collection	26
2.4.2 Experimental Design	27
2.4.3 Volumetric Change and Fitting Permeability Parameters	28
2.4.4 Experiment 2 - Damage to TZPs	28
2.4.5 Statistical Analysis of TZP score	29
2.4.6 Analysis of Circularity	30
2.5 Results	30
2.5.1 Volumetric change and model parameters	30
2.6 Discussion	36
2.7 Conclusion	42
<b>3 A 3D Agent-Based Model</b>	<b>43</b>
3.1 Chapter Overview	43
3.2 Introduction	43
3.3 Mathematical Model	47
3.3.1 Assumptions	47
3.3.2 PhysiCell: selection and comparison	48
3.3.3 Mechanics	58
3.3.4 Toxicity Model	61

3.4	Testing and Construction of the Model: A road map for future agent-based models . . . . .	62
3.5	Overview of 3D model . . . . .	64
3.6	Numerical Testing . . . . .	68
3.7	Parameter Fitting . . . . .	69
3.8	Simulation of Experimental Data . . . . .	71
3.9	Further Modeling . . . . .	80
3.10	Sensitivity of Parameters . . . . .	83
3.11	Theoretically Improved Protocols . . . . .	87
3.12	Discussion . . . . .	87
3.13	Conclusion . . . . .	94
<b>4</b>	<b>General Discussion</b>	<b>96</b>
	<b>References</b>	<b>98</b>
	<b>Appendix A</b>	<b>121</b>

# LIST OF TABLES

2.1	Table shows estimated permeability parameters at 22 °C for oocytes located within preantral ovarian follicles where $n$ is the number of oocytes. . . . .	31
2.2	Mean normalized TZP score for non-permeating addition treatments at 22 °C as well as the Dunnett test p-value. A * indicates a statistically significant difference from the treatment control (1xPBS at 22 °C). The sample size $n$ is the number of follicles. . . . .	33
2.3	Mean normalized TZP score for non-permeating addition treatments at 37 °C as well as the Dunnett test p-value. A * indicates a statistically significant difference from the treatment control (1xPBS at 37 °C). The sample size $n$ is the number of follicles. . . . .	33
2.4	Mean normalized TZP score for non-permeating addition treatments at 4 °C as well as the Dunnett test p-value. A * indicates a statistically significant difference from the treatment control (1xPBS at 4 °C). The sample size $n$ is the number of follicles. . . . .	33
2.5	Mean normalized TZP score for permeating addition treatments at 22 °C as well as the Dunnett test p-value. A * indicates a statistically significant difference from the treatment control (1xPBS at 22 °C). The sample size $n$ is the number of follicles. . . . .	34
2.6	Pairwise comparison of temperature within PBS treatment groups (Tukey). Statistically significant groups are marked with *. . . . .	35
2.7	Results of pairwise comparison of permeating treatments using Tukey test. No significant differences were found in the normalized mean TZP scores between permeating cryoprotectants. . . . .	36
3.1	Table of state parameters. . . . .	52
3.2	Table of cell specific parameters. . . . .	53
3.3	Table of additional cell and system parameters used in my model. . . . .	54
3.4	Table of cell specific permeability parameters. . . . .	55
3.5	Table of simulation concentrations. . . . .	56
3.6	Mean absolute error in oocyte volume calculated for different values of $dt$ . . . . .	70
3.7	Results of R-squared for spring constant fitting. Note that for the nonpermeating spring fit, 0.5xPBS was given the same experimental TZP Score as 1xPBS. . . . .	70
3.8	The different permeability parameters that were tested to assess sensitivity. $P_s$ was varied from typical ethylene glycol values by doubling (high) and halving (low) the value. . . . .	83
3.9	Table shows the TZP score of varying (or not varying) the solute permeability for the oocyte and/or granulosa cells up and down by 50%. . . . .	85
3.10	TZP score varies as spring constants are varied from the fitted parameters. The dark band indicates the fitted spring constants. In each case, two spring constants were held fixed at the fitted value while the third was varied. . . . .	86
A0	This figure shows the mean max volume change of whole follicle volume as well as the Dunnett test p-value comparing the 1xPBS control for each respective temperature. No max change in whole follicle volume differed significantly from control. . . . .	121

# LIST OF FIGURES

1.1	Phase diagram showing glass transition. The black arrowed path is a typical single step vitrification protocol. $T_g$ is the glass transition $T_h$ is the heterogeneous ice nucleation region and $T_m$ is the temperature of melting, between $T_h$ and $T_g$ a liquid is said to be supercooled.	8
1.2	This figure shows the subtle difference between a Cellular Automata model (top) and an Agent-Based model (bottom). The V squares show a Von Neumann neighborhood while the M squares show a Moore neighborhood. Note that the movement and replication of agent-based agents can be lattice independent and can happen anywhere in real space. . . . .	12
1.3	Chart showing the development (left to right) of a typical ovarian follicle and oocyte from primordial to antral. Bottom row shows the change in oocyte size through development and relative size between secondary stage oocyte and its surrounding granulosa cells. . . . .	15
2.1	This figure shows how the mechanical forces within the tissue are approximated with a combination of permeability parameters and spring constants. $k_{\text{Basement}}$ , $k_{\text{Granulosa}}$ , and $k_{\text{TZP}}$ are relative spring constants for springs which simulate the forces between granulosa cells and the basement membrane, between granulosa cells and between granulosa cells and the oocyte, respectively. The color of the parameters match the color of the cell type to which they correspond. . . . .	24
2.2	Box plot of the mean normalized TZP scores for each PBS treatment, the different colors correspond to different temperatures. . . . .	32
3.1	A labeled 2D cross section of a preantral ovarian follicle. Image is a Z-slice from a confocal microscopy imaging where F-actin has been stained green. Oocyte is $\sim 115 \mu\text{m}$ in diameter. .	48
3.2	A 2D cross section of the simulated ovarian follicle. Region containing voxels set to Dirichlet conditions (initial boundary conditions) are indicated in blue. . . . .	50
3.3	Schematic shows three springs with their corresponding spring constants. The wavy green line represents the basement membrane of the follicle. Red spheres are granulosa cells and the large blue spheres is the oocyte. The color of the parameters match the color of the cell type to which they correspond. . . . .	59
3.4	Change in position of a granulosa cell during an hour long simulation equilibrating in 15% ethylene glycol. (a) Shows x-coordinate, (b) y- coordinate, and (c) z-coordinate of the granulosa cell. . . . .	61
3.5	This set of 5 cells (1 oocyte in blue and 4 granulosa cells in red) serves to test the neighbourhoods and spring connections between cells. Cells are not to scale. . . . .	63
3.6	Flow chart of code run order. It is important to note that while each state is calculated in parallel, some states must be done before others (i.e. toxicity is calculated after volume). . .	65
3.7	An exterior view of the simulated follicle (drawn using Wolfram Research, Inc., Mathematica, Version 12.3, Champaign, IL (2021)). . . . .	67
3.8	Normalized oocyte volume over time for different values of $dt$ in seconds. . . . .	69
3.9	A 2D cross section of the simulated ovarian follicle that lies in the x-y plane(axis not shown). Sample granulosa cells, oocyte and whose follicle are marked in color. . . . .	72
3.10	Simulation results for equilibration in 15% (w/w) ethylene glycol. (a) Shows the normalized change in volume for the whole follicle, oocyte and 4 test granulosa cells from each layer along the positive $y$ -axis. (b) Shows the TZP distance and the mean TZP score where the dotted grey line is the associated experimental value for fitting mean TZP score under the same conditions. . . . .	73
3.11	Simulation results for equilibration in 15% (w/w) glycerol. (a) Shows the normalized change in volume for the whole follicle, oocyte and 4 test granulosa cells from each layer along the positive $y$ -axis. (b) Shows the TZP distance and the mean TZP score where the dotted grey line is the associated experimental value for fitting mean TZP score under the same conditions.	74

3.12	Simulation results for equilibration in a mixture of 15%et (w/w) glycerol and 15%et (w/w) ethylene glycol. <b>(a)</b> Shows the normalized change in volume for the whole follicle, oocyte and 4 test granulosa cells from each layer along the positive $y$ -axis. <b>(b)</b> Shows the TZP distance and the mean TZP score where the dotted grey line is the associated experimental value for fitting mean TZP score under the same conditions. . . . .	75
3.13	Simulation results for equilibration in 0.5xPBS. <b>(a)</b> Shows the normalized change in volume for the whole follicle, oocyte and 4 test granulosa cells from each layer along the positive $y$ -axis. <b>(b)</b> Shows the TZP distance and the mean TZP score where the dotted grey line is the associated experimental value for fitting mean TZP score under the same conditions. Note that the green dashed line indicates the likely anomalously low mean TZP score from experiment at this temperature (see Chapter 2); spring constants were fitted using the value at the grey dotted line. . . . .	76
3.14	Simulation results for equilibration in 1xPBS. <b>(a)</b> Shows the normalized change in volume for the whole follicle, oocyte and 4 test granulosa cells from each layer along the positive $y$ -axis. <b>(b)</b> Shows the TZP distance and the mean TZP score where the dotted grey line is the associated experimental value for fitting mean TZP score under the same conditions. . . . .	77
3.15	Simulation results for equilibration in 2xPBS. <b>(a)</b> Shows the normalized change in volume for the whole follicle, oocyte and 4 test granulosa cells from each layer along the positive $y$ -axis. <b>(b)</b> Shows the TZP distance and the mean TZP score where the dotted grey line is the associated experimental value for fitting mean TZP score under the same conditions. . . . .	78
3.16	Simulation results for equilibration in 5xPBS. <b>(a)</b> Shows the normalized change in volume for the whole follicle, oocyte and 4 test granulosa cells from each layer along the positive $y$ -axis. <b>(b)</b> Shows the TZP distance and the mean TZP score where the dotted grey line is the associated experimental value for fitting mean TZP score under the same conditions. . . . .	79
3.17	Time lapse cross section showing increasing toxicity (darkening color) in cells with time. . . .	80
3.18	Changes in TZP score during equilibration in 15% ethylene glycol while activating/deactivating tissue mechanics as well as activating/deactivating tissue uptake. . . . .	81
3.19	Simulation of equilibration to Ethylene Glycol followed by equilibration in holding media. <b>(a)</b> Shows the normalized change in volume for the whole follicle, oocyte and 4 test granulosa cells from each layer along the positive $y$ -axis. <b>(b)</b> Shows the mean TZP distance and TZP score, with a grey dashed line showing the expected TZP score from experiments. . . . .	82
3.20	The oocyte and granulosa cell volume response and TZP score during equilibration in 15% ethylene glycol while $P_s$ is halved (low), doubled (high) or remains the same (normal) for the granulosa cells and/or the oocyte. <b>(a)</b> Shows the oocyte volume response. <b>(b)</b> Shows granulosa cell volume response. <b>(c)</b> Shows change in TZP score. . . . .	84
3.21	Reconstructed TZPs from electron micrographs. Figure used under Creative Commons licence from Baena and Teraski [13]. . . . .	85
3.22	Simulation of 2-step CPA equilibration. <b>(a)</b> Shows the normalized change in volumes while <b>(b)</b> shows the mean TZP distance and TZP score. . . . .	88
3.23	Simulation of 4-step CPA equilibration. <b>(a)</b> Shows the normalized change in volumes while <b>(b)</b> shows the mean TZP distance and TZP score. . . . .	89

## LIST OF ABBREVIATIONS

2P	two-parameter
ABM	agent-based model
ANOVA	analysis of variance
CPA	cryoprotective agent
DMSO	dimethyl sulfoxide
EG	ethylene glycol
GLY	glycerol
GV	germinal vesicle
HM	holding media
IVM	in vitro maturation
IVF	in vitro fertilization
MAE	mean absolute error
NHP	non-human primate
NIH	National Institutes of Health
NSERC	Natural Sciences and Engineering Research Council of Canada
OHSU	Oregon Health and Science University
ODE	ordinary differential equation
ONPRC	Oregon National Primate Research Center
PDE	partial differential equation
PBS	phosphate buffered saline
PEG	polyethylene glycol
SUC	sucrose
TZP	transzonal projection

# 1 GENERAL INTRODUCTION

## 1.1 Chapter Overview

This first chapter provides an overview of the cryopreservation process, followed by a discussion of cryopreservation-induced damage. After providing the broad strokes, this chapter focuses on explaining cryopreservation-induced damage in terms of two key components: the mass transport of water and so-called cryoprotective agents into and out of cells and the methods by which samples are cooled and rewarmed. In particular, special attention is paid to the method of cooling known as vitrification. Vitrification has become the predominant method in preserving numerous samples, including reproductive tissues, which are the focus of the work in this thesis. After explaining the principles of cryopreservation, this chapter contains a section summarizing the valuable work done to capture and improve cryopreservation using quantitative models. A section follows this explaining how agent-based modeling could be an essential tool for constructing these quantitative models, as well as a brief overview of agent-based modeling in general. Having introduced cryopreservation and associated modeling, this chapter then briefly introduces preantral ovarian follicles, which is the focus of the modeling in this thesis. Lastly, this chapter outlines the purpose and objectives of this thesis and gives a general guide to the structure of the thesis as a whole.

## 1.2 Cryopreservation: an overview

Cryopreservation, a branch of cryobiology, is the body of techniques used to slow or suspend life at cold temperatures [152]. The primary goal of cryopreservation is to preserve a biological sample by reducing metabolic activity while limiting the destruction of the physical integrity, function, and viability of the sample. Biological systems remain intact at extremely low temperatures, but they are susceptible to the

cryopreservation process that gets them there [70].

In general, the process of cryopreservation has four sequential steps. First, samples must be selected, isolated, and equilibrated in their holding media. The initial physiological condition of cells and tissues appears to affect the cryopreservation process [16]. Many cryopreservation protocols begin by selecting tissues and cells that meet some metric, indicating their likelihood of being usable post-thaw. For example, selection criteria may involve only including oocytes that are both symmetric and have a centrally located nucleus [185]. There is an ongoing question of how to identify features for selecting tissues and cells, particularly oocytes, that will survive cryopreservation and/or maturation [16, 90, 204, 210]. Researchers are making progress in understanding which oocytes and embryos to use for fertility treatment; for example, Yanez et al. have shown that non-invasibly-determined mechanical properties of the zygote can predict outcomes in embryos. [90, 204, 210].

The second step is equilibrating chemical cryoprotectants (cryoprotective agents, or CPAs) into the selected biological sample. Since most cryoprotectant equilibration protocols involve the addition of hyperosmotic media that permeate the cells, this part of the equilibration process is often referred to as loading cryoprotectants. The majority of samples require the addition of CPAs, which serve to protect the sample during cooling and warming through a variety of actions. While all of the exact protective effects of CPAs are not fully understood, cryoprotectants appear to serve many functions, including depressing the freezing point, balancing osmotic forces, reducing relative salt concentrations, and reducing the formation of intracellular ice. Additionally, cryoprotectants shield lipids from free radicals, stabilize membranes, alter membrane phase transitions, and perform many other possibly essential functions [61, 163, 213, 216].

There are many cryoprotective agents available; however, molecules with a high permeability to the cells within a given sample, so-called permeating CPAs, are favoured. Examples of the most commonly used CPAs are ethylene glycol (EG), dimethyl sulfoxide (DMSO), 1,2-propanediol (PEG), or glycerol (GLY). Additionally, some simple sugars such as trehalose or sucrose can function as CPAs and be used externally or loaded directly into the cell [145, 177, 218]. However, while CPAs offer protective effects during the cryopreservation process, they also exhibit varying degrees of cytotoxicity. Experiments show that this toxicity is cell-type, concentration, and time-dependent [51].

Consequently, successful cryopreservation protocols require that the cryoprotectants provide greater protection than they do toxicity related damage. Determining the appropriate type and concentration of CPA for a given sample often requires an extensive experimentation process. The ability to model protocols *in silico* is increasingly valuable in determining potential CPA equilibration protocols or in optimizing preexisting ones [25, 173].

The third step, once CPAs are equilibrated, is that the sample must be cooled. This cooling process is where the biological sample must pass through the aqueous solution liquid-solid phase transition and face the danger of hypothermic damage [70, 203]. The primary sources of hypothermic damage to the sample are the formation of intracellular ice and the damage acquired from the osmotic effects of concentrating solutes as ice forms within the sample. [70, 138]. During cooling, under certain conditions, water can experience a meta-stable phase transition where the water transitions into an amorphous solid, or glass, a process called vitrification: within a vitrified region, there is no ice crystal formation. If the solute concentration is high enough within the sample, and the cooling rate is fast enough, an entire sample may be vitrified. In such a sample, ice crystallization cannot be observed, even under electron microscopy. This whole-sample vitrification allows one to avoid many forms of hypothermic damage, but at a potential cost, as toxic concentrations of CPA must be added to the sample to achieve full sample vitrification.

While increasing solute concentrations causes the still liquid portions of the sample to supercool, some of the intercellular and intracellular spaces may become vitrified during slower cooling, and this leads to some confusion in the terminology. Cryobiologists use the term vitrification specifically to mean whole sample vitrification and sometimes synonymously for rapid cooling. Vitrification and rapid cooling are not necessarily the same thing. Vitrification merely requires a cooling rate faster than the critical cooling rate, a rate at which a solution becomes an amorphous glass. This rate is fast enough that substantial crystallization cannot occur before the reduction in thermal energy (cooling) makes crystallization no longer possible; however, practically, this rate is relatively rapid in comparison to the rate of other cooling methods. The different cooling protocols, with intracellular ice formation or vitrification, are generally classified into the broad categories of slow cooling and rapid cooling. For clarity, in the rest of this thesis, the two general types of cooling protocols are vitrification, which strictly means whole sample vitrification, and non-vitrification

cooling.

Lastly, the biological sample must be returned to its physiologically normal state, rewarmed, and usually equilibrated in media free of CPAs. In rewarming, also called thawing, the solution phase transition is approached again but from the other side. Since the energy in the system increases, the potential for microscopic, less dangerous ice crystals to form larger more dangerous aggregate ice crystals emerges; this detrimental process is called recrystallization. For vitrified samples, the warming rate for a sample should be significantly higher than the cooling rate to avoid recrystallization or devitrification, which is the spontaneous formation of ice in a vitrified sample. Even in non-vitrification cooling, there is a risk of additional damage from recrystallization, thus in both vitrification and non-vitrification methods, warming rates must usually be higher than the cooling rate used [70, 102, 203]. In addition to rewarming, the CPAs must be washed from the sample while managing the osmotic forces as concentrations within the cell interiors and exteriors change.

### 1.3 Cryopreservation induced damage

During the cryopreservation process, biological samples experience damage from the changing thermal and solution conditions. Damage at the cellular level during cryopreservation has been explored over the last several decades and is broadly understood. Firstly, cryopreservation damage results from the disequilibrium of chemical potential induced by adding CPAs to the sample. Briefly, the addition of permeating CPAs causes the cells to first rapidly lose water and then subsequently swell as CPAs pass through the plasma membrane and exert osmotic forces on the cell until a new equilibrium is reached [68, 69, 139]. The cells also experience a change in chemical potential as the solution temperature is changed. During these processes, cell chemistry disruption can trigger oxidative agents [123], apoptosis and necrosis [31, 208], membrane phase transitions [73, 217], or other forms of damage or damaging events [100, 127, 152, 199]. As previously mentioned, CPAs can induce cytotoxicity damage that varies widely by cell type, species, concentration, temperature, and duration of exposure [11, 29, 62].

In non-vitrification cooling, there is a balance between cytotoxicity damage exerted by CPAs and damage induced by ice formation. For example, if the concentration of CPA is high, and the cooling rate is sufficiently

low, then the intracellular concentration of solutes increases, reducing the likelihood of intracellular ice formation. Intracellular ice formation is correlated with low cell survival and is a chief form of damage in non-vitrification protocols [138, 152]. Additionally, extracellular ice formation increases the solute concentration around and within cells leading to large osmotic gradients. This extreme osmotic pressure can damage cells until low temperatures prevent transport or chemical activity [136]. The freeze concentration prevents intercellular ice formation and leads cells to dehydration or internal supercooling [70, 160]. The concentration of internal solutes also offsets the damage non-permeating salts do in the absence of CPAs; especially as these concentrations become very high during freeze concentration [136]. If the cooling rate and solute concentration are not correctly adjusted, cells may experience lethal intercellular ice. Extracellular ice can also damage the extracellular matrix on cell exteriors [220].

In the case of vitrification protocols, a very high concentration of CPA is used to avoid all ice formation. This amount of CPA is almost always toxic, and the equilibration with this high concentration leads to extreme osmotic forces on the cells. Fortunately, CPA toxicity does cease when temperatures are low enough that chemical kinetics are virtually non-existent, but upon rewarming, it reemerges. In fact, there is a higher risk of ice nucleation damage on rewarming, although this form of damage is still present in non-vitrification protocols. The advantages of rapid cooling and even more rapid rewarming encourage the use of rates that are as rapid as possible; unfortunately, the larger the volume, the more challenging rapid temperature changes become. In practice, these cooling and warming rate challenges can be overcome by high CPA concentrations, and because of this, most of the damage occurs during vitrification when the initial high concentrations of solutes and CPAs are added or by chilling injury [63]. Additionally, under some conditions, the integrity of tissues is damaged from the thermal stresses of vitrification forming macroscopic cracks, known as fractures [153, 158].

At the tissue level, another form of damage occurs namely mechanical or toxic damage to the intercellular connections and tissue structural elements [17, 37, 111, 147]. This type of damage can destroy essential connections between cells and disrupt tissue-level morphology. I hypothesize that this type of tissue damage is caused in large part due to the nonhomogeneous shrinking and swelling of volume change during CPA equilibration and the corresponding strain that this places on intercellular connections, as further elaborated

on in Chapter 2. CPAs may also have a chemical effect on cellular connectivity [12].

## 1.4 Mass Transport

During the CPA equilibration step of tissue cryopreservation, mass transport is governed by diffusion in the interstitial space and either channel-regulated transport through the plasma membrane, diffusion through the plasma membrane or some combination of channel-regulated and diffusive transport. In general, CPAs diffuse through the sample solution until they reach the cell or tissue boundary, at which point permeable CPAs begin to pass through the plasma membrane, and cryobiologists label these CPAs as permeating. On the cellular level, all CPAs induce an osmotic gradient causing cells to undergo volumetric changes. Initially, the higher solute concentration outside of the cell causes water to leave via osmosis, which results in rapid cell shrinking. Simultaneously, the low concentration of solute inside the cell causes membrane-permeable CPAs to move into the cell. However, the plasma membrane is less permeable to CPAs than water, and as a result, the CPAs move more slowly into the cell. After the initial loss of water, water moves back in with the increasing intercellular CPA concentration; this concurrent movement of water and CPA swells the cell to a new equilibrium volume larger than the original volume. This shrink-swell process can occur once or repeatedly during protocols utilizing stepwise addition of increasingly higher concentrations of CPA.

Several different mathematical models capture CPA equilibration. Compared to the earlier Kedem-Katchalsky model [112], the two-parameter model captures CPA equilibration with a set of coupled ordinary differential equations [116]. The permeability of water and CPA and the initial conditions for water volume and CPA concentration entirely inform these equations [25, 28, 110, 116, 219]. The “two-parameter” equation in the multisolute form can be written as

$$\begin{aligned}
 \frac{dV_w}{dt} &= -L_p ART \left( M_s^e + M_n^e - M_n^i - \frac{\sum_{n=1}^k \delta_n S_n}{V_w} \right), \\
 \frac{dS_1}{dt} &= P_{s,1} A \left( M_s^e - \frac{\delta_1 S_1}{V_w} \right), \\
 \frac{dS_2}{dt} &= P_{s,2} A \left( M_s^e - \frac{\delta_2 S_2}{V_w} \right), \\
 &\vdots \\
 \frac{dS_k}{dt} &= P_{s,k} A \left( M_s^e - \frac{\delta_k S_k}{V_w} \right).
 \end{aligned} \tag{1.1}$$

These coupled equations describe the change in intercellular volume of water  $V_w$  and moles of the  $n^{\text{th}}$  solute,  $S_n$ . The parameters which affect the movement of solute and water into and out of the cell include the membrane water permeability  $L_p$ , frequently referred to in the literature as the hydraulic conductivity,  $A$  which is the surface area of the cell exterior,  $R$  which is the gas constant, and  $T$  which is the temperature of the cell and immediately surrounding solution. Additionally,  $M_s^e$  is the total osmolality of the permeating solutes exterior to the cell whereas  $M_n^e$  is the total osmolality of all the non-permeating solutes exterior to the cell.  $M_n^i$  is the internal osmolality of nonpermeating solutes and  $\frac{\sum_{n=1}^k \delta_n S_n}{V_w}$  is the total internal osmolality of all  $k$  permeating solutes. Note that these equations are formulated in terms of osmolality which is equivalent to the difference in chemical potential, and that the difference in chemical potential is what ultimately drives the movement of water and solute. The  $\delta_n$  term is a conversion factor from molarity to osmolality for a given solute. The  $\delta_n$  term is temperature dependent. In the  $\frac{dS_k}{dt}$  equation  $P_{s,n}$  is the permeability of the  $n^{\text{th}}$  solute. On the time scale and concentration scales relevant to CPA equilibration, most salts are considered non-permeating [25].

Bound within the cell is a fraction of osmotically inactive water. If a cell behaves as an ideal osmometer, then a linear fit of the Boyle-van 't Hoff relationship allows the determination of the osmotically active and inactive portion of the water volume [24, 139, 156]. This Boyle-van 't Hoff equation is given by

$$\frac{V}{V_0} = (1 - b) \frac{\pi_0}{\pi} + \frac{V_b}{V_0}, \quad (1.2)$$

where  $V$  is cell volume,  $V_0$  is the isotonic volume,  $V_b$  is the osmotically inactive volume of water,  $\pi_0$  is the isosmotic osmolality, and  $\pi$  is the osmolality at the point where the cell volume is  $V$ . Exposing a cell to various concentrations of non-permeating solutes informs the Boyle-van 't Hoff plot. Using linear regression, it is possible to determine the osmotically inactive fraction water.

## 1.5 Vitrification

A primary goal of cryopreservation protocols is to limit the amount of intracellular ice formation. Eliminating all ice formation is achieved via vitrification (generally, but not necessarily, rapid cooling). Vitrification occurs by reducing the energy of water molecules in a sample before ice crystallization can occur. If a liquid is cooled

to the glass transition temperature before significant crystallization can occur, the liquid will vitrify and no longer have the thermal energy required for ice nucleation. In pure water, this requires cooling rates on the order of  $10^7$  °C/min [203], which is impossible with the volumes of water necessary to hold biological tissue samples. However, as solute concentration increases in a liquid, it becomes easier to transition to the glass phases, since the unstable supercooled region (between the melting transition  $T_m$  and the heterogeneous ice nucleation transition  $T_h$ ) can either be avoided or reached at a higher temperature, as demonstrated in the phase diagram in Figure 1.1 (below). CPAs can also have solute specific effects that aid achieving the glass transition, including increasing viscosity, as well as thermodynamically stabilizing the glass state [63].

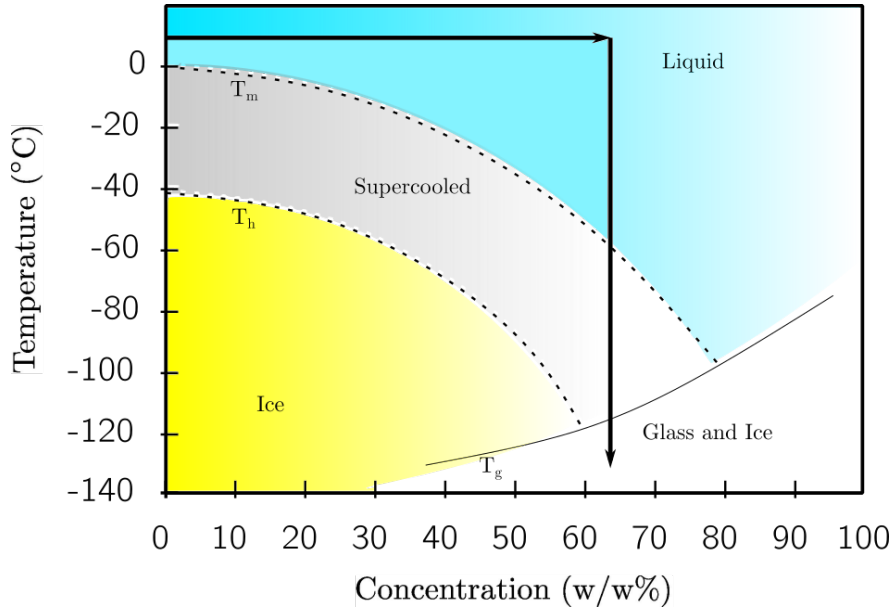


**Figure 1.1:** Phase diagram showing glass transition. The black arrowed path is a typical single step vitrification protocol.  $T_g$  is the glass transition  $T_h$  is the heterogeneous ice nucleation region and  $T_m$  is the temperature of melting, between  $T_h$  and  $T_g$  a liquid is said to be supercooled.

Increasing the concentration of CPAs can lower the critical cooling rate required to achieve vitrification. The critical cooling rate is the minimum cooling rate for the liquid fraction of a given solution to reach the glass transition without significant crystallization. The glass transition is the semi-stable phase transition line for an amorphous, vitrified, solid, shown in Figure 1.1 with the label  $T_g$ . The exact way in which a given solute lowers the critical cooling rate depends on the solutes involved. In vitrification protocols, CPAs can

protect cells from hypothermic damage and function to increase solution viscosity, stabilize the amorphous (vitrified) state, and in some cases, interrupt or block ice nucleation events. Practically, this leads to a protocol that requires minimizing the osmotic and cytotoxicity damage incurred from high concentrations of CPAs. The larger the volume of the sample, the slower it can be cooled, and thus the higher the concentration of CPAs needed to achieve whole sample vitrification. A prime example of this challenge is whole-organ cryopreservation, where the limitations of CPA equilibration and its concomitant toxicity are a critical hurdle to successful organ banking [75].

While non-vitrification cooling is a viable means of cryopreservation, vitrification has proven advantages. Vitrification allows for high survival rates as compared to fresh tissue, requires no specialized slow freezer equipment, and is more time-efficient, especially in a clinical setting [84, 115, 183, 184]. As such, at least with respect to the cryopreservation of reproductive tissues, vitrification has become the preferred method.

## 1.6 Modeling in cryopreservation

Modeling in cryopreservation research involves pairing observed phenomena with fundamental equations from biology, chemistry, and physics. To date, cryopreservation modeling has been instrumental in understanding the underlying biophysics and chemistry of why different protocols work for different biological samples. Modeling in cryobiology has widely been used for the rational design and optimization of cryopreservation protocols [51, 105, 109, 121].

Quantitative models of cooling cells date back to as early as the 1960s with the work of Peter Mazur [135]. In later work, Mazur proposed a set of ordinary differential equations that describes the mass transport of water and solutes through, into, and out of cells during cooling in the presence of ice with temperature dependency [136]. Mazur, Leibo, and Chu further proposed a heuristic model of the survival of cells dependent on the concentration of CPA and cooling rate known as the two-factor hypothesis, or “inverted U” [137]. At Cryo2017, in Heifei, China, Benson proposed expanding this heuristic by including extremely rapid vitrification cooling rates, which may avoid CPA toxicity, solution injury, and intracellular ice formation, possibly naming it the “inverted N” [85].

During CPA equilibration, classical water and solute transport models exist, such as the Kedem-Katchalsky

model or the two-parameter model [116], that accurately describe the movement of solutes and water using several measurable variables. In these models, mass transport is a function of the difference in chemical potentials across the cell's plasma membrane and the cell-type dependent permeabilities to those solutes. These transport models have been essential for understanding CPA and freezing induced osmotic changes in cells and tissues [219]. Using transport models is essential to designing protocols that avoid exceeding osmotic limits and cytotoxic damage because they allow damage to be controlled and predicted.

Models of the nucleation of ice have been crucial for designing protocols that minimize ice damage or avoid it altogether [9], despite a somewhat heated debate to this day over the exact underlying mechanics [3, 70, 106, 144]. All of these models capture essential damage to varying degrees. While intracellular ice formation modeling is a valuable part of understanding non-vitrification cooling, employing protocols that rely on vitrification avoids this type of damage during cooling [63].

Vitrification protocols avoid the damage that occurs during ice formation; however, in order to do this successfully, these protocols require the addition of far higher CPA concentrations. These high concentrations are necessary because they lower the critical cooling rate, and higher cooling rates (e.g.,  $> 10^3$  °C/min ) are challenging to achieve in practice for tissues, as mentioned previously in Section 1.3 and Section 1.5. This protocol decision then shifts the focus of damage models away from ice nucleation and toward toxicity and osmotic damage during CPA equilibration. For example, models such as the toxicity cost function model by Benson et al. [29], the hamster pancreatic islet model by Benson et al. [27] or the triphasic model by Abazari et al. [1] focus much more on the transport and corresponding toxicity of CPAs. Despite this, ice formation model utilization occurs in informing rewarming. During rewarming, the sample risks devitrification, and researchers have constructed several models for understanding and avoiding any ice formation during this process [34, 104, 214].

Modeling not only speeds up the search of vast parameter spaces but by applying models to already existing data models can also generate hypotheses for testing; in the case of this thesis, I demonstrate a model built on single-cell parameters that can be used to model heterogeneous tissue consisting of individual cells. Tissue modeling that can scale upwards from single-cell parameters would be especially beneficial since so much data has already been collected on single cells. Additionally, parameters for modeling input are

significantly easier to measure for single-cells isolated from tissue than to measure those same parameters in tissue, e.g., microscopy measurements of volume are far more accessible in an isolated, single cell, than in the interior of a tissue.

## 1.7 A Brief Overview of Agent-Based Modeling

Agent-based modeling has emerged as a relatively new and powerful, technique for simulating tissues *in silico* [131, 176, 196]. Agent-based tissue modeling conceptually builds on treating cells as agents operating under a set of rules that are unique to each cell type, e.g., all red blood cells behave the same way in response to a stimulus. These rules can be specified based on the type of agent (i.e., red blood cell vs. white blood cell), location within the simulation environment (i.e., located in high vs. low oxygen concentration areas) or conditional situations (i.e., a white blood cell is attached to another cell in the environment). This form of modeling allows for specific knowledge about the cell types and environmental conditions to be accounted for in the model and scales up to larger volumes (i.e., tissues). As such, agent-based models can potentially capture tissue-scale effects such as cell-to-cell connections, ice formation, environmental interactions, tissue scale mass transport like that from vessels and bulk sources, and cell scale effects like apoptosis, necrosis, localized volume change, and membrane phase transitions [23, 66, 72, 77, 124]. Agent-based modeling is of particular interest in cryobiology because most current models do not capture both scales of effects.

The idea of agent-based modeling traces its roots to von Neumann machines. Dr. John von Neumann was interested in the idea of machines that could replicate new machines. Theoretical modeling of such devices led conceptually to cellular automata models. These models define cellular automata as fixed agents on a grid, or lattice, that operate under a given set of agent-type or lattice-location rules. These cellular automata can have multiple states; for example, they could have the state on or off or the state black, red, or green. The area around a particular agent is called its neighbourhood. Neighborhoods are primarily defined by spatial proximity, usually, but not always they consist of adjacent agents. In general, neighborhoods determine the distance of interactions between agents or between agents and environmental features. Figure 1.2 presents an example of a cellular automata model as well as an Agent-Based model. The most famous cellular automata model is John Conway’s “Game of Life” [20]. Cellular Automata models have been used

to study how systems evolve solely based on varying their initial conditions while under a fixed set of rules [20, 38].

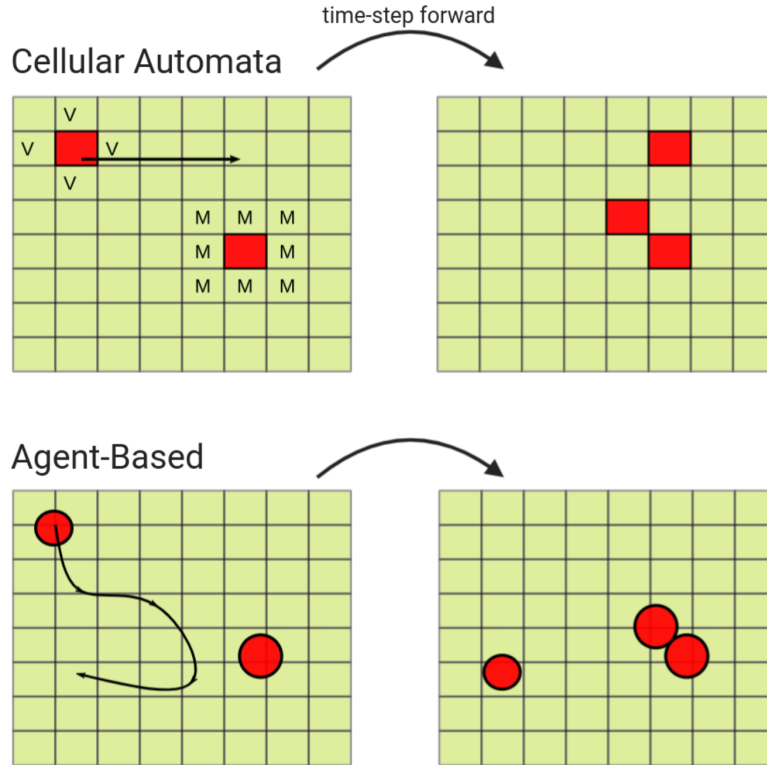


**Figure 1.2:** This figure shows the subtle difference between a Cellular Automata model (top) and an Agent-Based model (bottom). The V squares show a Von Neumann neighborhood while the M squares show a Moore neighborhood. Note that the movement and replication of agent-based agents can be lattice independent and can happen anywhere in real space.

Cellular automata models lend themselves to simulating interactions of discrete objects intuitively, and they have applications across many fields [14, 20, 21, 150, 200]. They have been used extensively in multiple subfields of biology as they are an excellent tool for modeling agents that replicate; however, discrete grids, where automata can only be at fixed locations, limit these models [6, 21]. This subtle distinction between fixed agents and fixed neighborhoods vs. agents that move through time and space is the usual definitional difference between Cellular Automata and Agent-Based Models; however the literature varies slightly on the

exact terminology [21, 44].

The ability for agents and neighborhoods to evolve from their original location in time and space allows for agent-based models to capture diverse, emergent, and complex processes [6, 131]. A simple example that highlights agent-based modeling at work is the addition of a spatial component to population modeling; a more thorough review of agent-based population modeling can be found in the text by Grow and Van Bavel [79]. In this example, when two animal “agents” meet, they have some chance of mating and producing offspring, eating each other or any number of preprogrammed actions, a stochastic process that can only occur when animals are in proximity. This process can then probabilistically adjust the “state” of pregnancy. The model operates in a virtual environment that can include the actual topography and relevant features of a particular animal’s environment, i.e., agents being attracted to food or repelled by natural boundaries. This model captures population dynamics in a more nuanced way that takes into account spatial and temporal conditions that a more traditional differential equation model lacks; however, it is more computationally costly and requires more experimentation to determine these extra parameters. As computational capability grows, agent-based models have become increasingly sophisticated. Agent-based models whose base agent unit is a cell are sometimes referred to as cell-based models; although, this terminology is not always clear. However, cells are hardly the limit for agent-based models, with some going to even smaller and more computational numerous agents such as molecules [6, 32, 49, 154, 176, 187].

While agent-based modeling can be a powerful tool for modeling cell interactions and tissues, it does have limitations. An imperfect understanding of the biomechanisms leads to flawed model assumptions. It can be challenging to extrapolate mechanisms down to the cell agent-level from complex emergent tissue-level behaviors that appear in experiments. Such extrapolation is already a defining problem of cell biology and makes the top-down construction of agent-based models challenging [6, 77]. Additionally, stochastic or emergent behavior is often sensitive to perturbations in parameters, which makes fitting difficult and requires experiments with high precision of measurement data [77]. The only way to construct useful agent based models is the virtuous cycle of pairing benchtop experiments with simulation based hypotheses testing. [74, 83].

Another drawback of agent-based modeling is the difficulty in using traditional mathematical modeling

analysis [6, 77, 140, 176]. While traditional equations and algorithms often govern discrete agents, the emergent system behavior from discrete units is not necessarily easily understood in the traditional frameworks of parameter sensitivity analysis or bifurcation analysis [6]. Researchers are often left using statistical methods to analyze their model in much the same way a more traditional biologist might analyze a sample [6]. This analysis often involves computing the output for a given model numerous times to conduct a statistical comparison. Repeated full-scale simulations lead to a high computation cost. Despite the availability of parallelization in agent-based modeling, computation time and memory usage can expand non-linearly with the number of agents implemented [6, 191]. The nature of agent-based modeling can also make these models difficult to run in a distributed environment, compounding the computational cost [6, 77, 191]. While these drawbacks generally apply to agent-based models, a more detailed discussion about the benefits and detriments of agent-based modeling, specifically in cryobiology, is given in Chapter 3.

The rational development and optimization of cryopreservation protocols for tissues requires many different factors to be accounted for, and doing this solely by laboratory experiment is time-consuming and resource-intensive (i.e., use of massive factorial experiments). Agent-based modeling offers an excellent vertical translation of models, that is, these models lend themselves to readily simulating lab-bench phenomena from first principles for testing hypothesis [6, 140]. As such, *in silico* experiments using agent-based models can take preexisting knowledge within the field and begin to elucidate new experiments and critical parameters in designing and improving cryopreservation protocols. Repeatedly refining and interpreting these models with data from new experiments produces a greater understanding of the underlying fundamental cryobiology involved and can inform improvements in clinical settings.

## 1.8 Preantral Ovarian Follicles

Mammals are born with all or much of their supply of oocytes, and each oocyte has the potential to develop from a single follicle [202]. The follicles begin as primary follicles and progress through several stages of development until a sufficiently developed oocyte begins to form a separation from its surrounding cumulus cells, known as the antrum, and finally, a mature oocyte is developed within the antrum and eventually released from the ovarian tissue, see Figure 1.3. This process is primarily controlled and regulated via

hormonal signaling [98]. During the maturation of an oocyte, known as folliculogenesis, the follicle contains only a few basic cell types consisting of the oocyte, granulosa cells, cumulus cells, and a few surrounding theca cells. Together the granulosa cells and oocyte are contained within a basement membrane called the basal lamina. The development and maturation of an oocyte depend heavily on the surrounding granulosa cells and their connections to the oocyte via specialized cytoplasmic extensions known as transzonal projections, TZPs [13, 60].

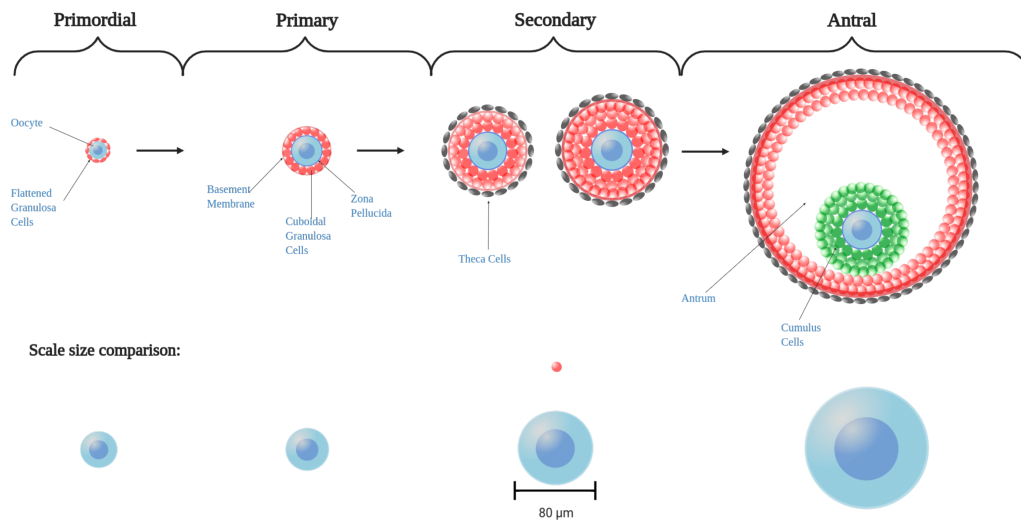


**Figure 1.3:** Chart showing the development (left to right) of a typical ovarian follicle and oocyte from primordial to antral. Bottom row shows the change in oocyte size through development and relative size between secondary stage oocyte and its surrounding granulosa cells.

Follicular development is classified based on size, the formation of the basal lamina, the appearance of the zona pellucida, the presence of the antrum, and the number of layers of cumulus cells surrounding the oocyte. While any stage follicle before the formation of the antrum (primordial, primary, and secondary) is considered preantral, for simplicity, in this thesis, preantral follicles shall refer to secondary stage follicles unless otherwise specified. Secondary stage follicles develop from primary follicles, have not yet formed an antrum, and are follicles with 2-4 layers of granulosa cells surrounding the zona pellucida while a theca layer

surrounds the basal lamina [47, 211]. Secondary stage follicles have become a target for cryopreservation with recent success occurring in mice [81], humans [162, 198], sheep [40], pigs [33], cats [134, 155] and non-human primates [184].

The primary interest in cryopreserving preantral ovarian follicles is the ability to restore fertility, particularly in young cancer patients. Loss of fertility is a common side effect of many cancer treatments, including radiation and chemotherapy [194]. While there are many challenges associated with preserving preantral follicles, including *in vitro* maturation, this treatment offers many potential benefits over the current alternatives [165, 166, 175, 182]. Current fertility preservation treatment options include the cryopreservation of embryos, mature oocytes and experimentally, the cryopreservation and subsequent autologous transplantation of strips of ovarian tissue.

These methods each have drawbacks. Cryopreserving embryos involves legal and ethical issues and requires delays for conception via either sperm donor or partner [58, 141, 192]. Preserving mature oocytes usually requires ovarian stimulation, which can delay cancer treatment by weeks and may cause adverse reactions in some oncology patients [39, 118, 186]. Reimplantation of mature tissue or cortical strips increases the risk of reimplantation of cancerous cells, and fertility only lasts for a limited time post-transplant [39, 114, 181]. Of these treatment options, only reimplantation and maturation of immature ovarian follicles are available to prepubertal cancer patients, and both are still considered experimental treatments in North America [174].

Additionally, preservation of mature oocytes is not a viable option for prepubertal patients, and the only technique currently available to them requires the preservation of ovarian tissues followed by *in vitro* maturation or autologous transplant of cortical strips followed by *in vitro* fertilization (IVF) [114, 148]. Prepubertal individuals are a growing group of patients needing fertility preservation as the rates of successful treatment of childhood cancers increase [114].

In contrast to the above existing treatments, the removal, preservation, and subsequent *in vitro* maturation of immature ovarian follicles offers a possibly better alternative. Increasing successful post-thaw maturation of preantral ovarian follicles to similar rates for mature oocytes would likely render immature oocyte preservation the main treatment route for oncology patients. As mentioned previously, cryopreservation and maturation of immature ovarian follicles eliminate the legal and ethical issues of embryo cryopreservation. It removes the

need for and risks of ovarian stimulation, and it avoids the possibility of reimplantation of cancerous cells from cortical strips. The treatment is available to both pre- and postpubertal women. The procedure requires less time, less expensive drugs, less patient monitoring, and lower risks [114, 178]. However, the cryopreservation and maturation of immature follicles are still challenging in humans and model mammal species. While live births have occurred from *in vitro* matured oocytes [88], these live births were from non-cryopreserved tissue. Cryopreservation damages preantral ovarian follicles and makes their maturation less likely than that of fresh tissue [45, 178]. Therefore, it is critical to make improvements to the cryopreservation process and understand the source of this cryo-induced damage.

Previously, tissue and cell models have increased the success of cryopreservation protocols [51, 105, 109, 157]. This thesis describes a novel agent-based model employed to develop such an improved cryopreservation protocol. This protocol could potentially increase not just the number of follicles intact post-thaw, but their success during *in vitro* maturation by improving the survival of cell-to-cell connections.

## 1.9 Purpose and Objectives

This thesis aims to demonstrate that 3D agent-based models of CPA equilibration can accurately capture tissue level damage and mass transport in preantral ovarian follicles. My specific objectives are to develop, employ, and fit a 3D agent-based model of CPA equilibration to experimental data that accurately captures:

1. Intercellular connections, particularly those associated with transzonal projections and the basement.
2. Accurate mass transport of water and CPA(s) into and out of the cells.
3. Intercellular connections within the tissue and the associated movement of cells.

## 1.10 Thesis Structure

This thesis comprises four chapters. **Chapter 1: General Introduction** covers a brief overview of cryopreservation and its associated modeling with an emphasis on vitrification and CPA equilibration as well as basic oocyte and follicle anatomy. **Chapter 2: Experimental Determination of Model Parameters**

covers experimental data and analysis to determine modeling parameters for an agent-based model of pre-antral ovarian follicles with data was collected from rhesus monkeys (*Macaca mulatta*), a model non-human primate species. This chapter also covers the importance of cryopreservation for fertility treatment and justifies the use of non-human primates as a model study species. **Chapter 3: A 3D Agent-Based Model** explains in detail all model components, how they fit and work together, as well as a brief but thorough overview of PhysiCell, the software underlying the agent-based model employed in this thesis. This chapter also discusses the advantages and disadvantages of the model as well as some of the computational and numerical challenges encountered. **Chapter 4: General Discussion** summarizes and explores the results of both the experiment and the corresponding model, challenges faced in this type of experimentation and modeling, and also discusses additional considerations for preantral ovarian follicle models. This chapter includes a discussion of future directions for this work.

## 2 EXPERIMENTAL DETERMINATION OF MODEL PARAMETERS

### 2.1 Chapter Overview

This chapter presents the two experiments performed in rhesus monkey tissue to determine model-relevant parameters for agent-based modeling of secondary stage preantral ovarian follicles. The first experiment measured the permeability parameters for cells within intact follicles as these parameters have not been previously measured. The second experiment measured the intactness of TZPs after experiencing various CPA or non-permeating solute equilibration treatments. This chapter is organized roughly into an experimental introduction, hypotheses, methods and material, results, discussion, and a conclusion section.

### 2.2 Introduction

Many cancer treatments are gonadotoxic and severely reduce the chance of reproduction post-cancer [114, 174]. Recent increases in post-cancer treatment survival rates for female patients, particularly young patients, have highlighted the need to improve post-cancer fertility treatments outcomes [56, 114, 182]. Currently, there are several options to preserve a patient's reproductive cells and thereby their fertility until remission. These options include the cryopreservation of embryos, mature oocytes, ovarian cortical strips, immature ovarian follicles, and the collection of multiple ovarian cell types for the development of artificial ovaries [57, 92, 114, 128, 171].

Of current fertility preservation treatment options, only embryo and mature oocyte cryopreservation are non-experimental and considered frontline fertility preservation treatments [80, 114]. While both embryo and mature oocyte cryopreservation have relatively high success rates [87], they are associated with several drawbacks. The cryopreservation of embryos and mature oocytes can delay cancer treatment since ovarian

stimulation is required. Ovarian stimulation may present additional risks to cancer patients as some types of cancer can be aggravated by the treatment and patients are more likely to experience negative side effects [161]. There is also the risk that patients will experience ovarian hyperstimulation syndrome, a rare but potentially fatal complication [39, 53, 188]. Furthermore, embryo and mature oocyte cryopreservation are not always viable treatment options for all cancer patients as they require patients to be post-pubertal. Embryo cryopreservation is additionally restrictive in that patients require a sexual partner or sperm donor. The aforementioned treatment options and in particular, embryo cryopreservation, come with a suite of legal and ethical issues; for example, Italy legally banned embryo cryopreservation between 2004 and 2009 due to ethical concerns [58, 64, 67].

Embryo and mature oocyte cryopreservation are not possible in prepubertal patients due to the absence of mature reproductive tissues. Fertility preservation treatment for prepubertal patients requires immature reproductive tissues to be surgically extracted, preserved, and matured *in vitro* [182]. One treatment option currently being tested involves dissecting a patient's ovaries and cryopreserving them as cortical strips—approximately 1 mm x 1 mm x 10 mm strips of the ovarian cortex. Once a patient is cancer-free, the cortical piece can be warmed and autologously transplanted; this both restores the patient's endocrine function and provides a return of fertility via oocyte removal from the transplanted tissue in conjunction with IVF [129, 181]. While autologous transplantation is an increasingly viable option and has the ability to restore endocrine function, there is a risk of reintroducing cancerous cells into the patient with some types of cancer [36]. Additional risks include ischemic damage to the tissue during reimplantation and time limits on the reproductive window as the tissue eventually fails to function, lasting on average only 26.9 months [181]. Alternative treatment options for prepubertal patients involve the collection, cryopreservation and *in vitro* maturation (IVM) of immature oocytes. IVM can be performed either before or after cryopreservation; however, recent studies suggest that cryopreserving before IVM leads to better or equal outcomes [113, 178]. Regardless of the order of IVM and cryopreservation, when a patient is ready to have children, the mature oocytes can undergo IVF and be reimplanted into the patient.

Preservation of earlier stage follicles has been proposed as the first-line method for oocyte cryopreservation in all patients due to its numerous advantages [82]. To wit, IVM of immature oocytes after cryopreserva-

tion eliminates the risk of reintroducing cancerous cells, avoids the logistical, ethical, and legal issues of cryopreserved embryos, is available to all patients, removes the need to delay treatment risk, and avoids the risks associated with ovarian stimulation. Despite the benefits of IVM, successful post-thaw recovery and maturation of ovarian follicles in humans are limited [113, 182]. Improvements in IVM post-thaw recovery could make this treatment a mainstay of fertility preservation and offer prepubescent patients another viable alternative.

In addition to challenges improving post-thaw survival, preserving reproductive tissues requires the maintenance of complex morphological structures. Tissue level damage occurring during cryopreservation may prevent oocyte maturation even if the oocyte and surrounding cumulus cells survive vitrification. A known location of tissue-level damage in preantral ovarian follicles is the transzonal projections (TZPs), as first discussed in Section 1.8. As highlighted in the 2013 review by Brambillasca et al. [35], in a number of studies, researchers demonstrate that damage occurs to TZPs during cryopreservation in a variety of different mammalian species. There are several possible causes of TZP damage, including excessive mechanical forces and CPA toxicity. These sensitive structural connections are essential for cell development, and damage to them may explain in part the reduction in the maturation of vitrified vs. fresh ovarian follicles.

Improving post-thaw survival and maturation can be accomplished by optimizing cryopreservation models to minimize damage [85, 107]. As discussed in Section 3.3, mathematical models have been successfully used to improve cryopreserved cells and tissues' survival and recovery. However, to date, none of the models commonly used in cryopreservation account for intercellular connections. Given that damage to the intercellular connections is a possible culprit in poor post-thaw recovery and maturation outcomes, a mathematical model that includes this feature could prove critical. For such a model to be useful, it must include parameters that accurately account for processes in which damage accrues during cryopreservation.

Modeling in cryopreservation is often divided into separate models for each of the three steps of cryopreservation - CPA (cryoprotective agent) equilibration, sample cooling, and sample rewarming. Briefly, as discussed in Chapter 1, CPA equilibration is where cryoprotective agents are added in an attempt to minimize ice formation and other forms of damage that occur during cryopreservation. A substantial amount of damage accrued during cryopreservation occurs during CPA equilibration [27, 63]. Thus, CPA equilibration

is a critical step in modeling and minimizing damage.

Existing CPA equilibration models work under the paradigm that maintaining cell volumes between specific volume limits will improve samples' survival and viability by reducing membrane damage due to osmotic forces. In tissues, these rapid osmotic changes in cells during CPA equilibration distort morphological structures and apply atypical forces to the tissue's various connections [25, 111]. While previous tissue models exist [1, 27], to my knowledge, this thesis is the first time cell-to-cell connection forces have been included with cell-to-cell mass transport in a cryobiological tissue model. Additionally, while toxicity from CPAs affects the cells [85], CPAs in tissues may also disrupt tissue components chemically. For example, a mixture of ethylene glycol, dimethyl sulfoxide, and sucrose was shown to damage TZPs and disrupt microtubules in germinal vesicle (GV) stage ovarian follicles from rhesus monkeys [193].

In individual cells, CPA equilibration is governed largely by osmosis and results in volumetric changes that can be modeled using the “two-parameter” (2P) model that describes the motion of osmotically active water volume into and out of a cell and the movement of permeating solutes (i.e. CPA's) [116]. In this model, salts, ions, and non-permeating CPAs are assumed to remain outside the cell during the CPA equilibration process; while so called permeating CPAs pass through the membrane into the cell interior. Note that this 2P model can be easily extended to multiple solutes as

$$\begin{aligned}
\frac{dV_w}{dt} &= -L_p ART \left( M_s^e + M_n^e - M_n^i - \frac{\sum_{n=1}^k \delta_n S_n}{V_w} \right), \\
\frac{dS_1}{dt} &= P_{s,1} A \left( M_s^e - \frac{\delta_1 S_1}{V_w} \right), \\
\frac{dS_2}{dt} &= P_{s,2} A \left( M_s^e - \frac{\delta_2 S_2}{V_w} \right), \\
&\vdots \\
\frac{dS_k}{dt} &= P_{s,k} A \left( M_s^e - \frac{\delta_k S_k}{V_w} \right).
\end{aligned} \tag{2.1}$$

In this equation, as mentioned in Chapter 1,  $L_p$  corresponds to the permeability parameter for water also known as the hydraulic conductivity, and  $P_{s,k}$  represents a given solute's permeability, and we note that these parameters are also temperature dependent. In fact, this temperature dependence almost always follows an Arrhenius relationship given by

$$L_p = L_{p_0} \exp(-E_a/RT - T_0). \tag{2.2}$$

In this equation  $L_{p_0}$  and  $T_0$  are the reference water permeability and reference absolute temperature.  $L_p$  is the hydraulic conductivity at absolute temperature  $T$ ,  $R$  is the gas constant and  $E_a$  is the activation energy. The activation energy may be determined by a linear regression of  $\ln(L_p)$  vs  $1000/RT$  [146]. The same relationship exists for  $P_s$  exchanged with  $L_p$ .

Using the 2P model requires knowing the amount of free water in the cell, also known as, the osmotically active fraction. The Boyle-van 't Hoff equation gives the relationship between a ratio of volumes and the osmotically active water fraction of a cell. In many cells, this equation describes a linear relationship, and a so-called Boyle-van 't Hoff plot yields easy extrapolation of the osmotically active fraction of the cell at the intercept indicating the ‘osmotically inactive volume’,  $b$ . The Boyle-van 't Hoff equation is

$$\frac{V}{V_0} = (1 - b) \frac{\pi_0}{\pi} + b, \quad (2.3)$$

where  $V$  is cell volume,  $V_0$  is the isotonic volume,  $b$  is the non-osmotically active fraction of water,  $\pi_0$  is the isosmotic osmolality, and  $\pi$  is the osmolality at the point where the cell volume is  $V$ .

Additionally, in practice, cells and tissues are equilibrated with CPAs by either adding a CPA to the media the sample sits in or by placing the sample into a new media containing CPA. This process can be done in a single step, multiple steps or with a continuous flow to achieve the final desired concentration of CPA [221]. The way in which CPAs, ions and salts move through the media and through the interstitial spaces during the equilibration process alters the osmotic response of the sample; in many cases this movement external to the tissue is largely the result of diffusion [27]. Diffusion in cell suspensions and in tissues has previously been modeled in a number of different ways, often relying on continuum approaches with phenomenological diffusion constants [7]. I model diffusion using BioFVM, a built in diffusion solver within the PhysiCell software [72], more details of how this model captures diffusion are given in Chapter 3.

The osmotic response of cells in tissues puts stresses and strains not just on cellular components but on the vital tissue level connections between cells. To fully account for the mechanical damages incurred during CPA equilibration and freezing in tissues, models should also describe the state of these tissue connections. In modeling ovarian follicles, I represent the connections between cells as springs extending directly from one membrane to the next, along the shortest path between cells (Figure 2.1).

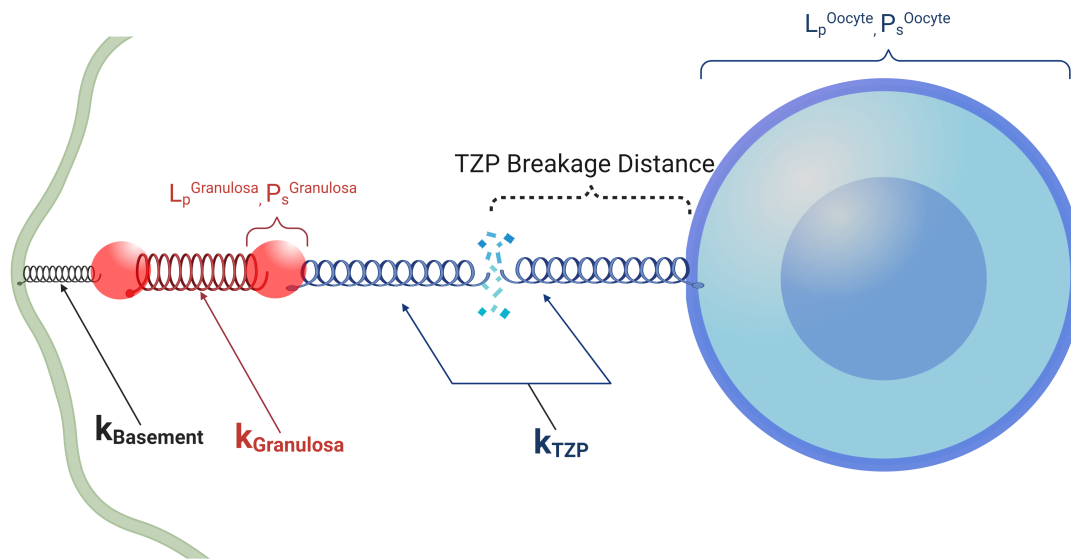


**Figure 2.1:** This figure shows how the mechanical forces within the tissue are approximated with a combination of permeability parameters and spring constants.  $k_{Basement}$ ,  $k_{Granulosa}$ , and  $k_{TZP}$  are relative spring constants for springs which simulate the forces between granulosa cells and the basement membrane, between granulosa cells and between granulosa cells and the oocyte, respectively. The color of the parameters match the color of the cell type to which they correspond.

The springs are then described by Hooke's Law parameters [89]. The spring connections that extend between the oocyte and granulosa represent the connections of the TZPs and they simulate the forces experience by their biological counterpart including breaking when they are stretched too far. The TZP score is a measure of the intactness of the connections between the granulosa cells and oocyte; this score is determined by measuring the fluorescence of stained F-actin in the space immediately adjacent and exterior to the oocyte, a space traversed by the TZP filaments predominantly made of F-actin. Lastly, tissue CPA equilibration models should include parameters that describe the CPA toxicity. Toxicity cost functions can be used as a proxy for toxicity damage; this cost function has specific toxicity rate parameters defined for a given cell. The model does not include toxicity damage to intercellular connections or to other structural features such as the basement membrane. Also not accounted for in this model is the extracellular matrix, ECM; instead, the model lumps any ECM forces into the general treatment of connections.

Model parameters must be determined via experimentation since they are considered CPA-, species-, and tissue-dependent. Permeability parameters have been measured for either mature oocytes or preantral

denuded oocytes in humans [91, 190], sheep [5, 54], bovine [59, 133], mice [59, 91, 117], and rarely non-human primates [108, 179, 215]. While measurements of oocyte permeability values have been taken in denuded oocytes, to my knowledge, there are no published measurements of oocyte CPA permeability within intact follicles. Obtaining sufficient tissue to measure these parameters in humans is difficult and costly. Thus, it is typical to use model species to obtain biologically relevant parameters when human tissues are unavailable. Given the similarity between non-human primate reproduction and human reproduction, non-human primates are considered one of the best model species for reproductive tissues [108, 180, 189].

In collaboration with colleagues from the Oregon Science and Health University (OSHU), we conducted experiments on secondary preantral ovarian follicles in adult female rhesus monkeys (*Macaca mulatta*) to determine model parameters. Non-human primates exhibit the same basic follicular structure and cell types as human reproductive tissue, and as such it is expected that only some membrane-specific parameters change between humans and non-human primate ovarian follicle tissue; this implies conservation of underlying cryopreservation relevant mechanisms and easily adjusting the parameters and their associated predictions using future human tissue measurements.

In order to verify that oocyte permeability parameters within follicles match those of denuded oocytes, we exposed secondary stage ovarian follicles to different treatments of permeating and non-permeating cryoprotectants (addition). These treatments include hyper- and hypoosmotic concentrations of PBS at different temperatures as well as treatments with 1M sucrose, 15% Ethylene glycol (EG), 15% glycerol (GLY) and a mixture of 15% EG with 15% GLY all at room temperature. The non-PBS treatments were exposed to the additional treatment of being equilibrated back to holding media (HM) (removal). We looked at volumetric changes of the whole follicle as well as the oocyte. Additionally, we measured the TZP score after these treatments to correlate volume change with TZP score.

## 2.3 Hypothesis

I hypothesized that secondary stage primate ovarian follicles experienced damage during cryopreservation due to mechanical forces during CPA equilibration. Based on this, I predicted that the differential shrinking of the whole follicle volume compared to the oocyte volume would mechanically damage the connections

between granulosa cells and the oocyte; this implied that exposure to increased concentrations of non-permeating solutes would correspond with increased damage to TZPs and greater distances between the oocyte and granulosa cell layers. I predicted the same trend would exist for permeating solutes; however, permeating solutes would do less overall damage at approximately the same osmolality. Additionally, the effect of temperature on TZPs would be an increase in damage corresponding to an increase in temperature. Additionally, I hypothesized that oocytes within follicles would exhibit the same osmotic response as those that have been denuded; therefore, interfollicular oocytes would have the same permeability parameters as denuded immature oocytes previously measured in the literature.

## 2.4 Materials and Methods

All reagents were purchased from Sigma (St. Louis, MO, USA) unless otherwise noted. Experiments were conducted by Dr. Mary Zelinski, Dr. Alison Ting and Jessica Stanley in Portland, OR. Once data was collected, I measured volumes of collected images and performed all statistical analyses.

### 2.4.1 Animals and Tissue Collection

Three adult female rhesus monkeys (*Macaca mulatta*) were housed and cared for at the Oregon National Primate Research Center (ONPRC) for this study. At ONPRC, individuals are paired and held in cages placed in a room with temperature and light regulation. Individuals had unrestricted access to water and were fed Purina monkey chow (Ralston-Purina, Richmond, IN, USA) twice, daily. In addition to the standard diet, individuals were also provided with fresh fruit and/or vegetables once daily. Animal use and care at the Oregon National Primate Research Center (ONPRC) followed the National Institutes of Health (NIH) Guide for the Care and Use of Laboratory Animals. ONPRC Animal Care and Use Committee approved all animal use protocols.

For all individuals ( $n = 3$ ), ovarian tissue was collected via necropsy or laparoscopically (total  $n = 152$ ) within the first few days of the menstruation. Once the ovarian tissue was extracted from the individuals, they were processed in 3-(N-morpholino) propanesulfonic acid (MOPS)-buffered tissue holding media (HM; CooperSurgical Inc., Trumbull, CT, USA) supplemented with 15% (v/v) serum protein substitute (SPS,

CooperSurgical Inc.) and 29 mg/ml of the antioxidant L-ascorbic acid 2-phosphate sesquimagnesium salt hydrate (ascorbic acid phosphate) at 37 °C. Specifically, ovaries were sliced with a Stadie-Riggs tissue slicer (Thomas Scientific, Swedesboro, NJ, USA) into cortical slices which were then incubated to maintain viability during the experiment. The 3 x 3 mm<sup>2</sup> cortical ovarian slices were incubated in HM with 5% CO<sub>2</sub> at 37 °C until they were needed for the experiments.

Prior to experimentation, follicles were manually dissected out of the incubated ovarian slices under a dissecting microscope using a 25-gauge needle. Secondary stage preantral ovarian follicles with a diameter between 120-250 µm were then selected manually; this size range corresponds to secondary stage-ovarian follicles with 3 to 4 layers of granulosa cells. Follicles were then treated with collagenase and washed in HM. A second round of selection occurred to remove any follicles with abnormalities following the criteria described in Xu et al. [207]. Briefly, follicles were selected based on having at least three layers of granulosa cells with no clear antral cavity, an intact basement membrane with attached stroma, and a visible, centrally located, oocyte. Standard petri dishes were prepared containing a minimum of 3 follicles held briefly in holding media to equilibrate until the experiments (described below) were conducted.

## 2.4.2 Experimental Design

All experiments conducted were completed across three days, such that all ovarian follicles used in a day were from one individual.

Follicles were randomly assigned to one of fifteen treatment groups to measure whole follicle and oocyte volumetric change. Treatment groups consisted of eight different solutions of solutes dissolved in HM, and these are 0.5x Phosphate Buffered Saline (PBS), 1xPBS, 2xPBS, 5xPBS, 1 M Sucrose, 15% w/w Glycerol (GLY), 15% w/w Ethylene Glycol (EG) and 15% w/w EG mixed with 15% w/w GLY. Each PBS solution was further separated into one of three different temperature groups (37 °C, 22 °C, 4 °C). All non-PBS treatments were conducted at 22 °C and 37 °C. All PBS treatment groups were equilibrated in HM at the appropriate temperature before further experimentation took place. The osmolality of each solution was measured each day of experimentation to ensure the correct concentration had been prepared.

For efficiency, multiple follicles were grouped in dishes and exposed to treatment simultaneously; equi-

libration was achieved by quickly substituting holding media in the dish with the appropriate treatment solution. Follicles were exposed to the treatment solution for 5 minutes, which is enough time for a complete reduction to the smallest cell volume and partial volume recovery based on previous literature data [108, 179]. After exposure to treatment, ( $n = 127$ ) follicles in each CPA treatment group were processed to measure damage to TZPs (see below for description), and the remaining follicles ( $n = 23$ ) were returned back to holding media. Follicles exposed to non-permeating treatments were not equilibrated back to holding media.

### 2.4.3 Volumetric Change and Fitting Permeability Parameters

Inverted microscopes (Olympus CK 40) with attached digital cameras (Olympus DP11) captured photomicrographs every five seconds immediately before treatment and throughout the duration of the experiment (a change from holding media to treatment solution and back). Camera 1 captured exposure at 37 °C, camera 2 at 4 °C, and camera 3 at 22 °C. Each image collected throughout the experiment was labeled with the date, treatment type, and animal. Due to the variability of follicles collected from ovaries and decreasing viability with time after removal, sample sizes are unbalanced. Measurements of follicles that moved out of frame during the experiment were discarded.

Images were analyzed by hand circling the exterior follicle boundary and oocyte boundary using Fiji's circle tool [169]. The area of this circle was then calculated using the built-in measure feature. Volumes were calculated based on the assumption of spherical follicles and spherical oocytes. Permeability parameters were estimated using a grid search to minimize the sum of square differences. For oocytes whose initial volume was missing, an initial value was estimated assuming the data fit the two-parameter model. Parameters were averaged within treatments. The code was written in Wolfram Mathematica [201].

### 2.4.4 Experiment 2 - Damage to TZPs

After exposure to solution treatments, a portion of follicles ( $n = 150$ ) were removed from solution treatment and stained with phalloidin. This staining has been shown to highlight TZPs [60]. These follicles were then fixed and examined under a fluorescent confocal microscope. The best z-slice image was selected from each follicle based on contrast, noise, and visibility of the oocyte. From this best z-slice multiple measurements of

the fluorescence in a 1-pixel thick circle around the zona pellucida, the region spanned by TZPs were taken. Those images that contained a large amount of noise or unusual fluorescence were reanalyzed using a higher threshold. Once an image was measured, all of the measurements for a particular image were averaged into a TZP score. This score was then normalized to the 1xPBS average score; again, 1xPBS served as the control. This process was performed on follicles removed after 5 min of exposure to loading treatments ( $n = 127$ ) and for follicles that were equilibrated back to holding media ( $n = 23$ ). This is similar to the methodology demonstrated by El-Hayek et al. in 2018 [60].

#### 2.4.5 Statistical Analysis of TZP score

For each treatment, TZP scores were normalized to the average TZP score for the 1xPBS at 22 °C this normalization assumes that the control treatment had little to no damage to TZPs and makes the normalized TZP score a fraction of intact TZPs. The 1xPBS treatment has osmolality very similar to holding media and normal physiological conditions and therefore was considered a control; there was no measurable change in oocyte or follicular volume when follicles are equilibrated to 1xPBS.

Data for 1M Sucrose was only obtained from Animal B so this treatment group was excluded from statistical tests that had an animal effect, or where  $n = 3$  was of insufficient statistical power.

A type III analysis of variance (ANOVA) was performed due to the unbalanced treatment groups, to determine if the solution, individual, or temperature had an effect on normalized TZP score; solution and temperature were tested for mixed effects. Post-hoc analysis and pairwise comparison tests were conducted to determine which, if any, specific treatments had statistically significant effects. A pairwise comparison Tukey test was conducted between “loading” and “unloading” groups to see if there was additional damage when follicles were equilibrated back to holding media. Finally, a Shapiro-Wilks test was also performed for normality but the normalized TZP scores failed this test with a  $p < .05$  ( $p = 0.03962$ ). While normality of residuals is an assumption of ANOVA they are relatively robust and still viable, see Glass et al. [76]. All analysis was performed using the R programming language (Version 4.0.3) in the RStudio environment (RStudio: Integrated Development for R. RStudio, PBC, Boston, MA, Version 1.4.1103).

## 2.4.6 Analysis of Circularity

While performing image analysis, a high degree of non-spherical shrinkage was noted in the confocal imagery. Correlation was tested between circularity and TZP score in the  $z$ -stack image. In this case, circularity is defined as  $2\pi r/p$ , where  $p$  is the measured perimeter and  $r$  is the radius of an equivalent disk. Oocyte circularity was calculated by isolating the image of the oocyte from the confocal images mentioned above; in this process, a boundary was drawn around the oocyte with the exterior cleared, then thresholding and binary transformation of the image was performed in Fiji [169]. In some images missing sections of the oocyte boundary were manually filled in. Once a binary oocyte boundary was isolated, it was processed through Mathematica’s “ComponentMeasures” function [201].

## 2.5 Results

In general, TZP damage occurred in all CPA equilibration treatments. Volumetric measurements of oocytes were used to estimate the permeability parameters.

### 2.5.1 Volumetric change and model parameters

A Dunnett test was performed to compare the maximum change in measured whole follicle area against the control treatment in each temperature regime. This test shows that there was no statistically significant difference between the 1xPBS control group and the maximum change in the whole follicle area of any treatments regardless of temperature, see Appendix A. Thus, no further analysis of whole follicle volume change was performed.

Conversely, volumetric changes in the interiorly located oocyte were more prominent. Hyperosmotic non-permeating treatment induced shrinking in the oocyte; whilst hypoosmotic treatments lead to oocyte swelling. Data to construct a Boyle van ‘t Hoff plot were limited, therefore a literature value was used for fitting. The osmotically inactive fraction,  $V_b$ , for immature oocytes is estimated most recently from previous literature value as  $0.288 \pm .0366$  [108]. In simulation, this value was rounded to 0.29.

Table 2.1 summarizes the results of estimating the permeability parameters for the oocytes. No oocyte

volume data were obtained for solutions containing 1 M sucrose. Since TZP score only showed a significant effect of temperature for treatment in 0.5xPBS, oocytes were only fit for permeability parameters at 22 °C.

**Table 2.1:** Table shows estimated permeability parameters at 22 °C for oocytes located within preantral ovarian follicles where  $n$  is the number of oocytes.

Treatment	$L_p$ ( $\mu\text{m}/\text{sec}$ )	$P_s$ ( $\mu\text{m}/\text{sec}/\text{atm}$ )	$n$
PBS	$0.013 \pm 0.00$	N/A	1
EG	$0.014 \pm 0.007$	$0.077 \pm 0.038$	2
GLY	$0.007 \pm 0.002$	$0.107 \pm 0.018$	3
EG with GLY	$0.005 \pm 0.004$	$P_{s,EG} = 0.7980.776, P_{s,GLY} = 1.150.621$	3

### TZP Score Results

A comparison of the animal control groups shows a statistically significant difference between animal A and the other two animals, with animal A having an abnormally low TZP score for the 1xPBS control treatment; therefore, data from animal A were excluded from further TZP analysis. This data removal included TZP scores from permeating CPAs at 37 °C.

A comparison between the equilibration and removal of EG, GLY and EG with GLY showed no statistically significant differences in TZP score. There were not enough data to determine if damage in 1 M sucrose was significantly different between treatment and returning the follicles to holding media.

A statistically significant effect of treatment was observed on normalized TZP score (Type III ANOVA,  $F(1,7) = 3.6216$ ,  $p = 0.0049$ ). A statistically significant effect of animal was not found ( $p > 0.05$ ). Further analysis of treatment looked at permeating CPAs and control, and within non-permeating treatments separately due to the differences in osmotic response between the two groups as well as due to PBS treatments being performed at multiple temperatures.

Within the non-permeating treatment groups (PBS and sucrose), PBS concentration had a significant effect (TYPE III ANOVA,  $F(1,3) = 5.8061$ ,  $p = 0.0019$ ) and temperature had a significant effect (TYPE III ANOVA,  $F(1,2) = 4.4027$ ,  $p = 0.01793$ ); however, there was no statistically significant interaction between temperature and treatment, see Figure 2.2. Post-hoc Dunnett test (see Tables 2.2–2.4) within each PBS

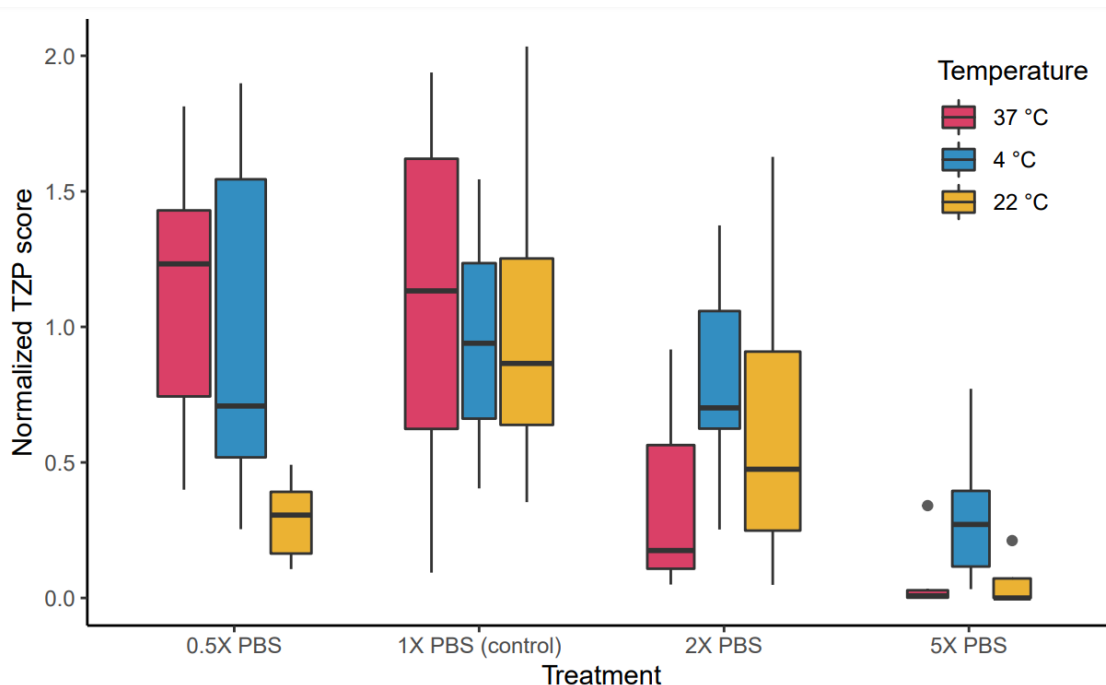


**Figure 2.2:** Box plot of the mean normalized TZP scores for each PBS treatment, the different colors correspond to different temperatures.

temperature group showed a statistically significant effect between control and all other treatment groups at 22 °C ( $p < 0.05$ ). Sucrose was only compared against PBS at 22 °C, since TZP data were only available at this temperature. At 37 °C and 4 °C there was no statistically significant difference between the control and any of the other treatment groups; it is worth noting that a pairwise comparison test showed that at 37 °C there was a small statistically significant difference between the control group and 5xPBS (Tukey method post hoc,  $t(45) = 2.672$ ,  $p = 0.0495$ ). The mean TZP scores at 22 °C for 0.5xPBS, 1xPBS, 2xPBS, 5xPBS and 1M Sucrose was  $0.3677 \pm 0.08$ ,  $1.00 \pm 0.22$ ,  $0.3677 \pm 0.13$ ,  $0.0896 \pm 0.06$ , and  $0.2221 \pm 0.21$ , respectively. At 37 °C the mean TZP score for 0.5xPBS, 1xPBS, 2xPBS, and 5xPBS was  $1.0965 \pm 0.23$ ,  $0.8680 \pm 0.26$ ,  $0.3194 \pm 0.17$  and  $0.1235 \pm 0.10$ , respectively. At 4 °C the mean TZP score for 0.5xPBS, 1xPBS, 2xPBS, and 5xPBS was  $0.9688 \pm 0.30$ ,  $0.7275 \pm 0.22$ ,  $0.6646 \pm 0.18$  and  $0.2574 \pm 0.10$ , respectively. See Tables 2.2–2.5 for a summary of these results.

**Table 2.2:** Mean normalized TZP score for non-permeating addition treatments at 22 °C as well as the Dunnett test p-value. A \* indicates a statistically significant difference from the treatment control (1xPBS at 22 °C). The sample size  $n$  is the number of follicles.

Treatment	Mean Normalized TZP Score	n	molality (mmol/kg)	molarity (mol/L)	Dunnett Test p-value
0.5xPBS	0.3677 ± 0.08	6	187	0.1861	0.0121*
1xPBS	1.00 ± 0.22	6	323	0.3206	X
2xPBS	0.3677 ± 0.13	6	643	0.6346	0.0121*
5xPBS	0.0896 ± 0.06	4	1600	1.551	0.0007*
1 M Sucrose	0.2221 ± 0.21	3	X	1	0.0114*

**Table 2.3:** Mean normalized TZP score for non-permeating addition treatments at 37 °C as well as the Dunnett test p-value. A \* indicates a statistically significant difference from the treatment control (1xPBS at 37 °C). The sample size  $n$  is the number of follicles.

Treatment	Mean Normalized TZP Score	n	molality (mmol/kg)	molarity (mol/L)	Dunnett Test p-value
0.5xPBS	1.0965 ± 0.23	6	187	0.1861	0.7781
1xPBS	0.8680 ± 0.26	6	323	0.3206	X
2xPBS	0.3194 ± 0.17	6	643	0.6346	0.1791
5xPBS	0.1235 + 0.10	4	1600	1.551	0.0853

**Table 2.4:** Mean normalized TZP score for non-permeating addition treatments at 4 °C as well as the Dunnett test p-value. A \* indicates a statistically significant difference from the treatment control (1xPBS at 4 °C). The sample size  $n$  is the number of follicles.

Treatment	Mean Normalized TZP Score	n	molality (mmol/kg)	molarity (mol/L)	Dunnett Test p-value
0.5xPBS	0.9688 ± 0.30	5	187	0.1861	0.8446
1xPBS	0.7275 ± 0.22	2	323	0.3206	X
2xPBS	0.6646 ± 0.18	3	643	0.6346	0.9968
5xPBS	0.2574 ± 0.10	4	1600	1.551	0.5034

**Table 2.5:** Mean normalized TZP score for permeating addition treatments at 22 °C as well as the Dunnett test p-value. A \* indicates a statistically significant difference from the treatment control (1xPBS at 22 °C). The sample size  $n$  is the number of follicles.

Treatment	Mean Normalized TZP Score	n	molality (mmol/kg)	molarity (mol/L)	Dunnett Test p-value
15% GLY	$0.2341 \pm 0.09$	6	2158	2.2	0.0368*
15% EG	$0.3605 \pm 0.09$	5	2503	1.868	0.0248*
15% GLY & 15% EG	$0.3926 \pm 0.16$	8	4788	4.04	0.0080*

**Table 2.6:** Pairwise comparison of temperature within PBS treatment groups (Tukey). Statistically significant groups are marked with \*.

0.5xPBS					
comparison	estimate	SE	df	t-ratio	p-value
37 °C - 4 °C	0.24395	0.27	45	0.905	0.6399
37 °C - 22 °C	0.72875	0.249	45	2.924	0.0146*
4 °C - 22 °C	0.48479	0.27	45	1.799	0.1816
1xPBS (control)					
comparison	estimate	SE	df	t-ratio	p-value
37 °C - 4 °C	0.25673	0.359	45	0.716	0.7553
37 °C - 22 °C	-0.132	0.249	45	-0.53	0.8572
4 °C - 22 °C	-0.38873	0.359	45	-1.084	0.5286
2xPBS					
comparison	estimate	SE	df	t-ratio	p-value
37 °C - 4 °C	-0.22893	0.312	45	-0.733	0.7452
37 °C - 22 °C	-0.04826	0.249	45	-0.194	0.9795
4 °C - 22 °C	0.18067	0.312	45	0.579	0.8322
5xPBS					
comparison	estimate	SE	df	t-ratio	p-value
37 °C - 4 °C	-0.01761	0.312	45	-0.056	0.9982
37 °C - 22 °C	-0.02424	0.307	45	-0.079	0.9966
4 °C - 22 °C	-0.00663	0.321	45	-0.021	0.9998

Post-hoc analysis of PBS treatments by pairwise comparison shows that for the control concentration, 1xPBS, there was no statistically significant effect of temperature. For 2xPBS as well as 5xPBS there was no significant difference between different temperatures. Surprisingly, in hypoosmotic media, 0.5xPBS, there was no statistically significant difference between 37 °C and 4 °C or 22 °C and 4 °C but there was a significant difference between 22 °C and 37 °C (Tukey method post-hoc,  $t(45) = 2.924$ ,  $p = 0.0146$ ) see Table 2.6.

Dunnett test comparisons between permeating CPAs and control show TZP scores for all CPA treatments are significantly different than control, see Table 2.5. Pairwise comparison shows that EG, GLY and EG with GLY were not significantly different from each other in TZP score ( $p > 0.05$ ), see Table 2.7. The mean TZP scores at 22 °C for EG, GLY and EG with GLY was  $0.3605 \pm 0.09$ ,  $0.2341 \pm 0.09$  and  $0.3926 \pm 0.16$ , respectively.

**Table 2.7:** Results of pairwise comparison of permeating treatments using Tukey test. No significant differences were found in the normalized mean TZP scores between permeating cryoprotectants.

comparison	estimate	SE	df	t-ratio	p-value
EG - EG & GLY	-0.1291	0.148	15	-0.873	0.6651
EG-GLY	0.0833	0.155	15	0.538	0.8542
EG & GLY - GLY	0.2124	0.139	15	1.532	0.3046

Correlation was tested between circularity and TZP score, since inverse correlation was weak within PBS treatments (Kendall rank correlation coefficient,  $z = 0.959$ ,  $p = 0.3374$ ,  $\tau = -0.0866$ ) as well as stronger but still weak within permeability treatments (Kendall rank correlation coefficient,  $z = -2.0405$ ,  $p = 0.0413$ ,  $\tau = -0.3184$ ) no further tests were performed.

## 2.6 Discussion

This chapter’s experiments provide evidence that TZP damage is largely the result of CPA equilibration and provides several of the parameters necessary to inform a mathematical model of preantral ovarian follicles. I review these results and also suggests a number of further experiments.

Non-human primate (NHP) oocyte and ovarian follicle data in the cryopreservation literature is very

limited. NHPs all exhibit very similar reproductive systems both anatomically and chemically to that of humans, yet only three studies provide volumetric data in response to CPAs for NHPs; those three studies were conducted on rhesus monkey (*Macaca mulatta*) [179], cynomolgus monkey (*Macaca fascicularis*) [215] and rhesus monkey (*Macaca mulatta*) [108]. This is the only study so far directly linking TZP damage to volumetric response in non-human primates, however a very recent publication by Kawai and Shimada shows very osmotically active solutions damage these connections in mouse ovarian tissue [111]. This recent study supports our current results, that is, a connection between volume change and damage to the connections between oocytes and granulosa within a follicle. This combined with the lack of additional damage seen during equilibration back to holding media suggests that the damage to TZPs is mechanical and a result of loss of volume; if the damage was the result of toxicity, which is usually exposure time-dependent, I would expect to see further damage with the increased duration of exposure during equilibration back to holding media. While the data on hypoosmotic treatments indicate that exposure to 0.5xPBS results in damage, which could be from swelling; the fact that this damage was only observed at 22 °C but not at 4 °C or 37 °C suggests this may be an artifact of noise in the data. If this is the case, then I anticipate further experimentation to support the results that substantial TZP damage does not occur in hypoosmotic media.

The estimated  $L_p$  for PBS at 22 °C was 0.013  $\mu\text{m/s/atm}$  in my study, this is in relatively good alignment with the results previously reported by Karlsson et al. for immature denuded rhesus monkey oocytes of an estimated  $L_p$  for PBS of 0.0135  $\mu\text{m/s/atm}$  at 23.5 °C [108]. Similarly, the estimated volumetric data parameters for oocytes within follicles are in relatively good agreement for previously reported permeability values for EG with my study having shown an  $L_p$  and  $P_s$  value of 0.014  $\mu\text{m/s/atm}$  and 0.077  $\mu\text{m/s}$  at 22 °C, respectively, with the studies by Karlsson et al. giving an  $L_p$  and  $P_s$  value of 0.0167  $\mu\text{m/s/atm}$  and 0.12  $\mu\text{m/s}$  at 23.5 °C, respectively, in immature oocytes from rhesus monkeys [108]. However, due to the difficulty of obtaining these measurements the permeability parameters were estimated with small sample sizes and large error, this puts these measurements in question and further studies should be done to verify these parameters.

There was disagreement between our measurements of glycerol permeability and those previously published. In this experiment, I estimated a relatively high, non-zero permeability for glycerol. It was previously shown that glycerol was largely impermeable to immature oocytes in non-human primates [179, 215]. Pre-

vious studies of non-human primate oocytes have found glycerol to be both damaging and impermeable [179, 215] causing a response more similar to that of non-permeating solutes. My estimated permeability parameter measurements came from a small sample size and exhibited a relatively large standard error; this suggests that previously determined values in the literature may be more accurate. Additionally, glycerol was reported to almost always cause non-spherical shrinkage of the oocyte and lasting deformation, thought possibly to be due to damage of the F-actin by glycerination [215]. Alternatively, in my data, when calculating circularity for glycerol treatments, only 3 of the 6 oocytes exhibited circularity less than 0.8; this value corresponds to half of the oocytes remaining relatively circular and suggests that glycerol may not always cause non-spherical shrinkage. Unfortunately, since circularity could not be measured at the same time as volume change, my measurement of volumetric change may be capturing non-spherical shrinkage, which can be misinterpreted as volume loss due to permeation of glycerol. Importantly, the closeness of the ethylene glycol and PBS permeability parameters, even with small sample sizes and high error, suggests that experimental data collected from cell suspensions, of which there is a great deal, may be used to inform tissue level models; however, more experimentation needs to be done.

Unexpectedly, in the case of the mixture of ethylene glycol with glycerol I observed a significant increase in permeability of both glycerol and ethylene glycol. In fact, I was unable to locate any study of oocyte or follicle volume response to mixtures of CPA, even though such mixtures are commonly used [2, 41, 120, 143, 158]. I was additionally unable to find any previous study where the multisolute two-parameter model with more than one permeating solute had been fit to experimental data. If mixtures of CPAs alter permeability characteristics, particularly increasing permeability while not substantially increasing damage, it could open new possibilities for cryopreservation. Another explanation for the estimation of the unusually high permeability parameters is that the volumetric measurements captured non-spherical, also referred to as non-isotropic, shrinkage. Given that it is difficult to visualize the entire oocyte membrane during the complete duration of the volume experiment and that glycerol has been shown previously, and in our work, to frequently cause aspherical shrinkage it is possible I was not accurately capturing the volumetric change. In this experimental set up there was no way to screen for oocytes that shrink non-spherically as prescreening can potentially alter the TZP score. Prescreening is commonly performed in experiments

with denuded or mature oocytes, but this does not always succeed in preventing non-spherical shrinkage as noted in previous studies [108, 179]. Given the incredibly high permeability parameters, small sample size, and high variability in measurements, it seems unlikely that these estimated parameters are accurate, and further experimentation is needed. Indeed this offers a potential explanation for why the mean TZP score for this highly concentrated treatment was in line with the other permeating CPA treatments despite the higher osmolality of this solution. Alternatively, the suspiciously large estimated permeability for EG and GLY could indicate that the multisolute two-parameter model (Equation (2.1)) might not extend to multiple solutes as well as previously thought, or that the combination of EG and GLY may have some unanticipated effect that is ultimately protective toward TZPs (i.e. makes them more flexible).

To my knowledge, no studies have attempted to measure whole secondary stage follicle volume change. However, a similar experiment with primordial follicles showed that change in whole follicle volume, when exposed to 1.0 mol/L EG, was about 27% [5], corresponding to a change in radius of about 10%. Note that additionally primordial follicles only have a single layer of flattened granulosa cells [197]. This amount of change in a larger structure with 3 to 4 layers of granulosa cells combined with the high variability of the data would likely be too small a change to be statistically significant with the experimental design used in the present study, but it seems likely that the whole secondary stage follicle volume change is relatively small. It is also possible that a longer duration of exposure is needed to capture the complete volume loss in the whole follicle, despite a very rapid predicted equilibration of granulosa cells. The previously mentioned experiment in primordial follicles required 5 minutes for complete volume reduction of a tissue with fewer granulosa layers than the secondary stage ovarian follicles observed in this study. It is additionally possible that the granulosa cells can compensate for the osmotic changes in the oocyte by stretching or deforming to some degree while remaining tightly attached to their neighbouring cells, thus dampening the amount of whole follicle volume change. Regardless of the amount of change in whole follicle volume, oocytes are visibly shrinking away from the granulosa cell layers that surround them. There are several possibilities for how some TZPs remain intact. These possibilities include gaps occurring between the granulosa cell layers that cannot be seen by light microscopy, TZPs may be highly elastic or become so during equilibration, there may be deformation of the basal lamina, there could be unequal forces on the TZPS, or there could be deformation of the granulosa

cells themselves.

When follicles that had been exposed to permeating CPAs were equilibrated back to holding media there was no statistically significant change in mean TZP score. This suggests that the volume reduction that occurs during CPA equilibration coincides with the measured damage and that volume increase is not contributing a significant increased damage.

Post-hoc analysis from the data set shows a non-statistically significant difference between 0.5xPBS and 1xPBS at room temperature, see Table 2.6; however, it does not show this in other temperature regimes suggesting that this is anomalous. Individual variation in TZP score between follicles and oocytes even within the same animal can be quite high; for example, the standard error in the 1xPBS was  $\pm 0.281$  on a mean of 0.90, this makes the analysis of reproductive tissue very difficult. Distinguishing the effects of treatments can be obscured by this naturally occurring variation. Extensive variation, both between individuals and even within the same individuals tissue, has been previously reported, but varies by species [22]. This large variation reported in these tissues may be partially explained by subpopulations of follicles due to anatomical differences that occur during development. Irving-Rodgers et al. found evidence that follicles may exhibit significant differences in their basal lamina, including alterations in the connectivity with the outer most granulosa cells; differences in the connectivity between the cells and the basement membrane could affect the overall “stiffness” of the tissue [94]. Irving-Rodgers et al. defined some follicles as “loopy” in which the basal lamina has actually looped into the follicle altering the shape and attachment of basal granulosa [93, 94]. Further studies that elicit better understanding of intra- and inter-animal variation of reproductive tissues have big implications for both cryobiology and reproductive medicine; currently, it proves a significant challenge that requires larger sample sizes and numbers of animals which can be particularly difficult to come by in primate and human studies.

This study involves equilibration of follicles in solution for 5 minutes, and due to the relatively slow equilibration of primate oocytes as compared to other model species such as mice, this equilibration does not have time to fully equilibrate to a maximum volume within the five minutes of experiment [108]. The reason for this partial equilibration in experiment is that the tissue is somewhat time sensitive and has a limited duration of viability outside of the ovaries [159]. Karlsson et al. measured the final equilibration volume

as taking more than 10 minutes in the presence of typical CPAs in both mature and immature denuded oocytes [108]. However, despite the lack of a complete expansion to the final cell volumes, it is still possible to estimate the  $L_p$  and  $P_s$  and to estimate the final volume as long as we have an accurate measure of the initial rapid change in volume. Determining this accurately in tissue is complicated by not having any way to determine when the CPA has been transported through the volume of media and granulosa cell layers to reach the oocyte exterior, in some data sets there appeared to be a delay before osmotic volume change occurred. In other data sets the volume change occurred rapidly. The differences between data sets made the initial oocyte volume measurement difficult. I accounted for these difficulties by either estimating the initial volume using the two-parameter equation or by assuming that the treatment reached the oocyte at the first time step where volume change was measured immediately afterwards.

As mentioned, I was unable to account for non-spherical shrinkage (also referred to as non-isotropic in some literature [215]) of the oocyte due to difficulty in visualizing the complete oocyte during the entire equilibration. It is extremely difficult to obtain volumetric measurements within this particular tissue type. The whole follicle exterior appears to exhibit very little shrinkage or swelling, likely due to tight bonds between the granulosa cell layers and to the basement membrane, the basal lamina. Granulosa cells, being too small to be seen under methods that do not require fixation, cannot be visualized experiencing volume change during the equilibration process. The oocyte is partially obscured by these granulosa layers and as cryoprotectant penetrates the tissue, the cells darken making visibility of the oocyte increasingly difficult, often rendering the oocyte temporarily or permanently invisible to the inverted microscope. Preferentially staining the oocyte to increase visibility would have required microinjection which is impossible to do without risking mechanical changes to the follicle via the syringe. Additionally, dyes may alter the osmotic response of the oocyte and some dyes can travel from the oocyte through the transzonal projections into the granulosa cells preventing selective staining [17]. Future studies may be able to take advantage of clever use of new staining techniques but would require extensive additional experimentation.

Future studies could be conducted with apparatus that can detect live changes in the volume of granulosa cells; although this presents many technical challenges due to the small size of granulosa cells, about 10  $\mu\text{m}$  in diameter. It would also be very useful from a modeling perspective to test several different concentrations

of a particular CPA to determine the concentration dependence on TZP damage. It is possible that the shrinkage of whole follicles occurs on a time scale much longer than that of the oocyte and longer duration equilibration may result in further TZP damage, although this seems unlikely based on the evidence that the volume loss in the oocyte is the predominant cause of TZP damage. Further studies could be conducted to examine the peculiar results encountered with a mixture of EG and GLY; the permeabilities of so-called multisolute solutions require further experimental validation to ensure the accuracy of the two-parameter model, as well as determine how such mixtures may offer protective effects on the TZPs.

The volumetric experiment provides evidence that permeability parameters from denuded oocytes can be used in tissue modeling; and that possibly tissue modeling in general can use permeability parameters determined from individual cells; however, this seems to contradict the findings of Higgins and Karlsson [86] when they compared two different cell types in both monolayers and cell suspensions. The data allow for the construction of a new cryobiologically relevant model that captures the mechanical intercellular forces induced by the osmotic effects of CPA equilibration. This is the first study that can be used to correlate the measured damage in transzonal projections with specific equilibration protocols. Additionally, this study provides evidence that damage to TZPs during equilibration is mechanical damage and occurs only during the “loading” of CPAs, and not during “unloading”. Combining data from this chapter with the model developed in Chapter 3 will allow us to predict methods of improved CPA equilibration that minimizes damage to the vital TZPs.

## 2.7 Conclusion

This study provides evidence that damage in this tissue type is mechanical in nature and establishes that permeability parameters from cell suspension data can be used in tissue modeling. This means that tissue models can be constructed from already existing literature values and fit to experimental data of damage to intercellular connections. In the next chapter I will construct such a model that specifically focuses on this tissue type and simulates *in silico* the results of this experiment for an average preantral ovarian follicle. Since this model has been constructed based on data from rhesus monkeys it should be possible to adapt it “off the shelf” for human tissues, which can be used to inform clinical models with further experimentation.

## 3 A 3D AGENT-BASED MODEL

### 3.1 Chapter Overview

This chapter presents a more detailed summary of cryopreservation modeling, agent-based modeling, and an introduction to the model I constructed. The following section then goes through all the model's components, followed by a roadmap for the model's construction and an overview of the final 3D preantral ovarian follicle model. After this is an exploration of the model with numerical testing and parameter fitting using the experimentally determined TZP score from Chapter 2. Following this section are simulations approximating the experimental data from chapter 2, some simulation data exploring the importance of having working mass transport and mechanics, and a presentation of a hypothetical equilibration to and from 15% (w/w) Ethylene glycol. Following this, the chapter explores the model more in-depth with some parameter sensitivity testing. After sensitivity testing, I present some simulations of hypothetical improved equilibration protocols. There is then a discussion of the model covering its advantages and drawbacks. Finally, the chapter ends in a concluding section to highlight what was covered, discuss the ramifications of the model, and give future directions.

### 3.2 Introduction

Modeling can be used to design cryopreservation protocols with improved post-thaw success rates [26, 107]. These models often focus on accurately capturing one of three parts of the cryopreservation process: cryoprotectant agent (CPA) equilibration, cooling/ice formation, and warming. In regard to models of CPA equilibration, significant progress has been made in understanding and accurately capturing the mass transport in single-cells in suspension. More recently, models of CPA equilibration have been extended to capture

mass transport in whole tissues [1, 27, 48] in an attempt to improve the storage of tissues for transplantation. There are several approaches to capturing mass transport in whole tissues which include but are not limited to; continuum models, network dynamic models, and cell-based transport models.

Continuum models are a class of models prominently featured in the tissue transport literature [8, 25, 96]. In continuum models, the tissue is usually treated as homogeneous, neglecting spatial variation in structure and transport parameters. Continuum models are governed by a system of partial differential equations (PDE) and associated boundary conditions. Compared to the agent-based approaches introduced in Chapter 1, continuum models are usually computationally less expensive in both memory and time-to-compute [168, 176]. Additionally, continuum models are well understood, and are widely found in scientific literature [168, 176, 205].

In cryobiology there has been a wide diversity of continuum models, most using the model based on Fick's law of diffusion [173], but other more sophisticated models include a triphasic (water, CPA, and solid fraction) articular cartilage model [1], and a one-dimensional porous media model [209]. Treating the tissue of interest as homogeneous makes model implementation simpler but loses critical cell-level details (i.e. cell-type specific toxicity) that may be important to understand cryopreservation related damage. To reach this level of detail, other mass transport models have been implemented including "network dynamics" models, [55, 65, 170], cell-based transport models [27], and other ad-hoc approaches [125] to try to capture details at an individual cell level features.

Agent-based modeling is a promising modeling approach new to cryobiology that can accurately capture transport as well as cell-level features. Agent-based modeling has been successfully demonstrated in cancer research [103], population ecology [79], economics [4], and molecular biology [78, 176]. Agent-based models can capture cell-level changes in mass transport, heat transfer, signaling pathways including necrosis and apoptosis, intercellular connections, toxicity, and even morphological changes. Agent-based models represent a new paradigm in capturing cell-oriented effects that permeate through tissues during the cryopreservation process [72].

In biological settings, the agents of an agent-based model behave autonomously, mimicking the responses of cells (or other biological units) to external and internal stimuli. Analogous to signaling pathways, the virtual

cell can detect changes in the environment and other agents, and analogous to other biological processes these agents have “states” and can alter their behaviour based on time, size, or proximity. The interaction between cell agents, their neighbors, and defined boundaries within the environment can be used to simulate intercellular and inter-tissue connections. Features such as vascular structure, availability of oxygen, or other substances can be simulated within the digital environment; this environment can vary to fit tissue morphology as well as temporal alterations. The placement or packing of cells can be used to simulate the interstitial spaces of non-homogeneous tissues or differently shaped tissue boundaries. The variety and flexibility of this modeling approach combined with increasing access to higher speed and higher memory computing has led to a large increase in the number of publications on agent-based models as well as the development of many different software platforms for running such simulations [154, 176].

A similar technique to agent-based modeling has been previously utilized in a cryobiological model by Benson et al. [27]. The Benson et al. model took advantage of the spherical geometry in hamster islets of Langerhans to capture mass transport at the cell-to-cell, cell-to-interstitium, and interstitial levels. However, to my knowledge the vast array of agent-based modeling tools is just beginning to be applied to cryopreservation. Beyond my own work, Jennings et al. of Newcastle University presented a poster at Cryo2019 [101] on CryoDynaMo an extension of BioDynaMo which utilizes agent-based modeling for predicting cooling and intercellular ice formation. Additionally, Jennings et al. presented further on this modeling platform at Cryo2020 [122]. However, to my knowledge they have not yet published any peer reviewed results. A feature that is insufficiently addressed in previous cryobiological models is merging the increasing understanding of cryopreservation relevant mass transport with the biophysics of intercellular connections. Several papers have demonstrated that the process of cryopreservation alters tissue structures and produces strain and stress on tissue connections during equilibration and cooling [15, 17, 111, 130].

The model presented in this chapter is concerned with capturing the first and last step in any cryopreservation protocol: the equilibration of cryoprotectants (CPAs). Cryoprotectants are a necessary component of cryopreservation, and are predominantly small, lightweight molecules that, when added to tissue or cell suspensions, permeate through the cells and surrounding fluid [151, 203]. The equilibration of CPAs typically involves the rapid movement of water out of cells as permeating CPAs move into the cell interior more slowly;

this happens on a time scale of minutes and is affected by the concentration of salts and other ions in the interior of the cells and in the cryopreservation media [70, 112]. Most cells, when exposed to the typically used concentrations of CPAs, behave as osmometers and respond immediately to the change in external solute concentration without osmoregulation. As such, the difference in permeability between water and CPAs most commonly results in an initial rapid volume loss as water flows out of cells and a slower recovery of volume as CPAs enter bringing a return of water to the cells interior; eventually, a new larger cell volume is reached at equilibrium [70, 116]. The permeability of water and CPAs varies across species and cell type [151]. In tissues comprised of heterogeneous cell types (i.e. ovarian tissue), the rate of equilibration can vary widely between the different cell types and can be exacerbated by large differences in the isosmotic volume of the cells. In particular this model attempts to capture the effects of CPA equilibration; namely, the change in cell volumes, the accumulation of cryoprotectant chemical toxicity, and the resultant forces induced by changing osmotic gradients.

This chapter examines the hypothesis that the differences in rates of change of volume for different cell types within a tissue can result in significant damage as intercellular connections must compress or stretch to accommodate changes to the sizes of cells. To wit, evidence of this is in the preservation of ovarian tissues; Kawai and Shimada [111], Navarro-Costa et al. [147] and Bus et al. [37] have shown that in mouse and bovine species respectively, damage occurs to the vital connections between oocytes and granulosa cells. Additionally, evidence presented in Chapter 2 describes damage to transzonal connections (TZPs) during CPA equilibration in non-human primates. Damage to TZPs may be a significant source for the lower post-cryopreservation survival and fertility of ovarian tissues in mammalian species and may be of importance to the cryopreservation of preantral ovarian follicles.

As introduced and discussed in Chapter 1, the cryopreservation of preantral ovarian follicles, is increasingly being studied as a potential fertility treatment. This tissue type has particular importance in providing a fertility option in juvenile cancer patients who are lacking mature oocytes or the ability to generate embryos and receiving gonadotoxic cancer treatments. This tissue may also serve as a treatment for patients that cannot undergo ovarian stimulation.

In order to design improved cryopreservation protocols for preantral ovarian follicles, and demonstrate

the utility of agent-based modeling in cryobiology, in this chapter I test the hypothesis that differential rates of change at the cell level, modeled via agent based modeling techniques, can explain observed damage to key mechanical connections within tissues. In this chapter I implement and inform a model of preantral secondary stage ovarian follicles with data from rhesus monkeys. The similarities between non-human primates, humans, and other mammalian tissues mean that this model should be easily adapted across species. Additionally, because this agent-based model uses cells as the agents, these models can be constructed using already determined single-cell parameters as supported in Chapter 2. The model built within the PhysiCell framework [72] consists of a finite volume diffusion solver paired with a custom cell level volume calculation using the cryobiologically relevant multisolute two-parameter equation. Cells were created *in silico* within a virtual cartesian microenvironment of uniform cubic voxels. Dirichlet boundary conditions simulate the addition or removal of CPAs and salts. I approximate intercellular connections as springs governed by Hooke’s law and fit for three spring constant parameters. Additionally, a toxicity cost function is calculated as described by Benson et al. [29], and a novel mechanical damage score is implemented.

### 3.3 Mathematical Model

This section provides a detailed explanation of the components of my model as well as the underlying assumptions.

#### 3.3.1 Assumptions

The model I constructed takes advantage of several features that make preantral ovarian follicles a “simple” tissue to capture using agent-based modeling. First, the tissue is relatively spherically symmetrical and has a centrally located oocyte. Second, oocytes themselves are spherical, and are surrounded by densely packed granulosa cells that are “cuboidal” and generally rounded in shape (Figure 3.1). As such, the geometry of the follicle is convenient to approximate within a Cartesian space. Third, theca cells can be excluded from the model as they are not essential for *in vitro* maturation (IVM) [206, 212]. Additionally, since theca cells are sparse and connected to the exterior of the basal lamina, they are assumed to have little effect on the intercellular forces within the follicle interior. The interior within the basal lamina which includes

the granulosa cells and oocyte, often called the cumulus oocyte complex, is considered the essential unit for cryopreservation [164] thus the focus of this model. Fourth, there are no blood vessels that enter the basal lamina, so tissue vasculature can be excluded from the model. Finally, a preantral follicle has relatively few cells, on the order of thousands, which makes the simulation with cell-agents computationally less expensive in comparison to larger tissues.

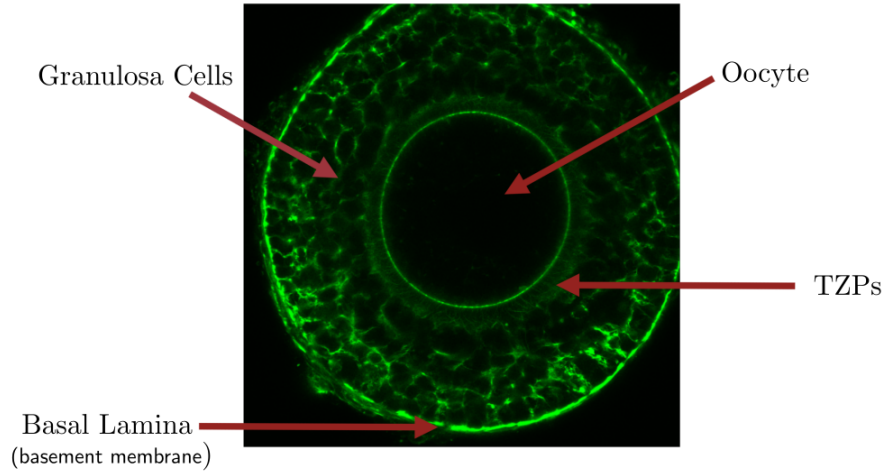


**Figure 3.1:** A labeled 2D cross section of a preantral ovarian follicle. Image is a Z-slice from a confocal microscopy imaging where F-actin has been stained green. Oocyte is  $\sim 115 \mu\text{m}$  in diameter.

### 3.3.2 PhysiCell: selection and comparison

The model I constructed is based on a pre-existing computational framework and software called PhysiCell [72] which allowed me to reduce construction and testing time. There are a tremendous number of software platforms for agent-based modeling due to the wide variety of models and their idiosyncratic needs [176, 191]. I used several criteria for selecting a software platform.

1) The software had to be open source. It is vital to peer review that large scale modeling and code-based research projects be open so that a complete understanding of the research can be reached. Proprietary code is difficult to analyze and can make reproducing results unduly expensive. Additionally, open-source platforms tend to be modifiable and extensible.

2) The software had to be able to run on a desktop computer. While I did have access to high performance computing resources on campus, part of the goal of my project was to develop modelling that is widely

accessible.

3) The platform needed to be parallelizable. Parallelization is essential for this research once the proof-of-concept model is developed as even thousands of cells can take computing time from hours to days based on the level of parallelization that is available and the sophistication of the model. Additionally, I hope to create a model that will be extended to the modelling of larger tissues.

4) The platform needed to be somewhat future proof, i.e. be in relatively high use, with support and updates as techniques and technology improve. It is important that the code base developed be useful in modelling for as long a time as possible and that the code, at least in general, be transferable to other systems and platforms down the line.

Based on this criteria PhysiCell was chosen. This project used PhysiCell version 1.6 written in C++11 and compiled with g++ version 9.

## Mass Transport

PhysiCell relies on a finite volume method diffusion solver which utilizes a fixed diffusion rate and uniform cartesian lattice for any given substance as detailed in Ghaffarizadeh et al. [72]. The finite volume solver PhysiCell utilizes called BioFVM [71], solves the transport PDEs by breaking the space into a discrete, three-dimensional, finite uniform grid and solving the diffusion numerically in each of these grid spaces. Each cube within the grid is referred to as a voxel. These voxels provide the microenvironment in which the cells exist and can be activated as sources and sinks of up to 124 substances.

In practice, BioFVM solves for the diffusion across each voxel through a combination of operator splitting and a Thomas algorithm approach. Details on how this is coded can be found in the supplementary material of the paper by Ghaffarizadeh et al [71].

Specifically, in my model, the outermost voxels in a sphere around the tissue are set to be an infinite source of the treatment solution at a defined concentration (i.e. Dirichlet nodes), and diffusivity is assumed to be constant for each solute in PhysiCell. In order to accommodate expansion of tissue during hypoosmotic treatments the diffusion of solutes from the Dirichlet boundary conditions to the edge of the tissue is  $\sim 36 \mu\text{m}$  (Figure 3.2).

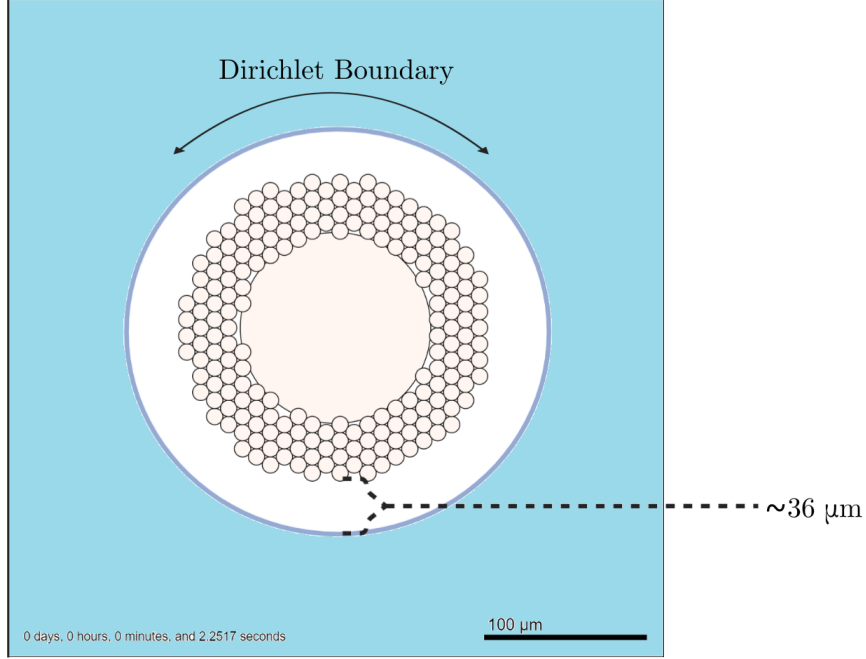


**Figure 3.2:** A 2D cross section of the simulated ovarian follicle. Region containing voxels set to Dirichlet conditions (initial boundary conditions) are indicated in blue.

To my knowledge, the exact CPA diffusivity parameters have not been determined for ovarian follicles, so I adapt parameters from previous work from Benson et al. [27], Maroudas et al. [132], and Page et al. [149] who modeled diffusion in similarly sized tissues and theoretical volumes. By default, PhysiCell implements the following reaction diffusion equation,

$$\frac{\partial \rho}{\partial t} = D \nabla^2 \rho - \lambda \rho + S(\rho^* - \rho) - U \rho + \sum_{\text{cells } k} \delta(x - x_k) W_k [S_k(\rho_k^* - \rho) - U_k \rho] \text{ in } \Omega. \quad (3.1)$$

This equation is discretized across a Cartesian mesh with domain  $\Omega$  and boundary  $\partial\Omega$ . In this equation  $\rho$  is the vector of chemical concentrations,  $\rho^*$  is the vector of saturation densities,  $t$  is time,  $\delta(x)$  is the Dirac delta function,  $x_k$  is the  $k$ th cell's position with volume  $W_k$ . Additionally,  $D$  is the diffusivity vector, and  $\lambda$  is the decay vector, and both of these remain constant throughout the domain. Lastly,  $S$  and  $U$  are the bulk supply rate and uptake function, respectively, and these can have different values in each voxel. The summation term that utilizes a Dirac delta function represents the built in cell uptake and secretion for the  $k$ th cell and is not used by my model; instead, I utilized custom uptake code paired with the two-parameter mass transport equation as described immediately below. In this equation, vector-vector products are Hadamard products and multiplied element-wise[72].

The uptake terms for cells in Equation 3.1 are not formulated to match what has become the standard transport model in cryobiological applications, the two-parameter model. To have the cell agents interact with the solute diffusion, I implement custom code in the PhysiCell package to model transport across the cell boundary with the generalized multisolute “two-parameter” (2P) [116, 219] model as given by:

$$\begin{aligned}
\frac{dV_w}{dt} &= -L_p ART \left( M_s^e + M_n^e - M_n^i - \frac{\sum_{n=1}^k \delta_n S_n}{V_w} \right), \\
\frac{dS_1}{dt} &= P_{s,1} A \left( M_s^e - \frac{\delta_1 S_1}{V_w} \right), \\
\frac{dS_2}{dt} &= P_{s,2} A \left( M_s^e - \frac{\delta_2 S_2}{V_w} \right), \\
&\vdots \\
\frac{dS_k}{dt} &= P_{s,k} A \left( M_s^e - \frac{\delta_k S_k}{V_w} \right).
\end{aligned} \tag{3.2}$$

Again, in this set of coupled equations  $L_p$  corresponds to the permeability parameter for water also known as the hydraulic conductivity, and  $P_{s,k}$  represents the permeability of solute  $k$ . The  $\frac{\sum_{n=1}^k \delta_n S_n}{V_w}$  term is the total internal osmolality of all  $k$  permeating solutes, where  $\delta_n$  is the conversion factor for molarity to osmolality for a given solute term. The remaining parameters are described in Table 3.1, Table 3.2, Table 3.4, and Table 3.3.

**Table 3.1:** Table of state parameters.

Parameter Symbol	Parameter Name	Units
$k_{\text{TZP}}$	spring constant for granulosa to oocyte attachment	kg/s <sup>2</sup>
$k_{\text{Basement}}$	spring constant for granulosa to basement membrane attachment	kg/s <sup>2</sup>
$k_{\text{Granulosa}}$	spring constant for granulosa to granulosa attachment	kg/s <sup>2</sup>
T	Temperature	K
S	moles of solute	mol
$\frac{dV_w}{dt}$	water flux	μm/s
$\frac{dS}{dt}$	solute flux	mol/μm <sup>2</sup> /s
$M_s^e$	external osmolality of permeating solutes	osmol/kg
$M_n^e$	external osmolality of nonpermeating solutes	osmol/kg
$M_s^i$	internal osmolality of permeating solutes	osmol/kg
$M_n^i$	internal osmolality of nonpermeating solutes	osmol/kg
$c_s^e$	external concentration of permeating solutes	mol/kg
$c_n^e$	external concentration of nonpermeating solutes	mol/kg
$c_s^i$	Internal concentration of permeating solutes	mol/kg
$c_n^i$	internal concentration of nonpermeating solutes	mol/kg
$\Delta x$	displacement of spring	μm
$v$	velocity	μm/s
$k$	spring constant	s <sup>-2</sup>
$m$	mass	kg
$a$	acceleration	μm/s <sup>2</sup>
$F$	force	kg μm/s <sup>2</sup>
$t$	time	s
$k_{\text{rel}} = km$	relative spring constant	kg/s <sup>2</sup>
$x_r = \Delta x - x$	rest length of spring	μm

**Table 3.2:** Table of cell specific parameters.

Cell Type	Parameter Symbol	Parameter Name	Value	Units
Oocyte	$V_0$	initial volume	817283	$\mu\text{m}^3$
	$V_b$	osmotically inactive fraction	0.29	unitless
	$R_0$	initial radius	58	$\mu\text{m}$
	$A$	surface area of an oocyte	42273.3	$\mu\text{m}^2$
Granulosa	$V_0$	initial volume	523.6	$\mu\text{m}^3$
	$V_b$	osmotically inactive fraction	0.2	unitless
	$R_0$	initial radius	5	$\mu\text{m}$
	$A$	surface area of a granulosa cell	314.159	$\mu\text{m}^2$

The multisolute two parameter model (Eq. 3.2) is solved for each simulated time step using a second order Adams-Bashforth method [18], initialized with a forward Euler step. For reference, the second order Adams-Bashforth method is

$$y_{n+1} = y_n + \frac{3}{2}hf(t_n, y_n) - \frac{1}{2}hf(t_{n-1}, y_{n-1}), \quad (3.3)$$

which is a numerical solution with step size  $h$  to the initial value problem

$$y' = f(t, y) \text{ with } y(t_0) = y_0. \quad (3.4)$$

This method is explicit and thus not always stable, however it has a relatively low computational cost and requires less custom code compared to the implicit second-order Adams-Moulton [95].

This formulation of the 2P model in PhysiCell requires osmolality values from the exterior of the cells; however, the built-in diffusion solver calculates values in molarity. This leads to a mismatch of units between the diffusion solver and the 2P model. In order to overcome this hurdle, I used a different form of the 2P model where I calculate the movement of water using approximated molar fractions. This formulation is

**Table 3.3:** Table of additional cell and system parameters used in my model.

Parameter Symbol	Parameter Name	Value	Units
D	diffusivity of CPA in tissue	530	$\mu\text{m}/\text{s}^2$
D	diffusivity of Salt in tissue	510	$\mu\text{m}/\text{s}^2$
dx,dy,dz	Voxel dimensions	10,10,10	$\mu\text{m}$
$dt$	time step size	0.1	s
omp_num_threads	number of processors used	8	unitless
R	gas constant	$0.08205 \times 10^{-3}$	J/mol K
$\overline{V}_w$	partial molar volume of water	0.018068	l/mol
$\overline{V}_n$	partial molar volume of NaCl	0.0271	l/mol
$\overline{V}_{EG}$	partial molar volume of EG	0.05577	l/mol
$\overline{V}_{GLY}$	partial molar volume of GLY	0.07368	l/mol

given by the set of equations:

$$\begin{aligned}
c_w^e &= \frac{1 - c_s^e \overline{V}_s - c_n^e \overline{V}_n}{\overline{V}_w}, \\
x_w^e &= \frac{c_w^e}{(c_w^e + c_s^e + c_n^e)}, \\
c_w^i &= \frac{1 - c_s^i \overline{V}_s - c_n^i \overline{V}_n}{\overline{V}_w}, \\
x_w^i &= \frac{c_w^i}{(c_w^i + c_s^i + c_n^i)}, \\
\frac{dV_w}{dt} &= L_p ART \left( \frac{1}{\overline{V}_w} \log \left( \frac{x_w^e}{x_w^i} \right) \right).
\end{aligned} \tag{3.5}$$

The parameters for this set of equations are described above in Table 3.1 and Table 3.3; note that in this formulation the  $L_p$  and  $P_s$  permeability parameters can be different than in other formulations of the 2P model. The 2P model requires that  $L_p$  and  $P_s$  be known for each cell type, and these parameters have been established for many cell types, however these values have been predominantly determined in cell suspensions or isolations and not within tissues [86, 172]. The experiment in Chapter 2 provided evidence that parameters measured in isolated cells can apply within tissues, at least for oocytes. However, to my knowledge, previous literature does not provide transport parameters for CPAs in granulosa cells in any mammalian species. The

**Table 3.4:** Table of cell specific permeability parameters.

Cell Type	Parameter	EG Values	GLY Values	PBS Values	Units
Oocyte	$L_p$	0.0167	0.007	0.0135	$\mu\text{m/s/atm}$
	$P_s$	0.12	0.107	N/A	$\mu\text{m/s}$
Granulosa	$L_p$	0.0029	0.0029	0.0114	$\mu\text{m/s/atm}$
	$P_s$	0.0345	0.0345		$\mu\text{m/s}$
Cell Type	Parameter	EG & GLY Values			Units
Oocyte	$L_p$	0.0053			$\mu\text{m/s/atm}$
	$P_{s,EG}$	0.798			$\mu\text{m/s}$
	$P_{s,GLY}$	1.15			$\mu\text{m/s}$
Granulosa	$L_p$	0.0029			$\mu\text{m/s/atm}$
	$P_{s,EG}$	0.0345			$\mu\text{m/s}$
	$P_{s,GLY}$	0.0345			$\mu\text{m/s}$

permeability of water and CPAs in granulosa cells likely follows a similar shrink-swell pattern seen in most cells; there is evidence of this in primordial follicles, which contain one layer of flattened granulosa cells, exhibit this shrink-swell [5]. Additionally, granulosa cells have been shown to exhibit mRNA indicating the presence of several types of aquaporins; aquaporins are the main pathway for the transport of water and a number of typical CPAs [167]. In my model I approximated the permeability parameters of granulosa cells as adherent endothelial cells [68]. Adherent endothelial cells are small, roughly spherical cells that have had their CPA permeability parameters measured and have been shown to be chemically and physiological similar to granulosa cells [10, 19]. Additionally, adherent endothelial cell CPA permeability parameters have been measured in monolayers [68] which could potentially have different permeability parameters than those measurements made in cell suspensions [86] despite evidence to the contrary for denuded oocytes from Chapter 2. Parameters measured in monolayers, if they are different than cell suspensions, are likely to be closer to their values within tissue [86]. However, there is a possible significant difference in adherent endothelial cells and granulosa cells permeability to glycerol. Amorim et al. [5] showed that in ovine primordial follicles the

**Table 3.5:** Table of simulation concentrations.

Solute	Dirichlet Boundary Concentration	Units
0.5xPBS	0.1861	mol/l
1xPBS	0.3206	mol/l
2xPBS	0.6346	mol/l
5xPBS	1.551	mol/l
HM (holding media)	0.2534	mol/l
15% (w/w) EG	2.2	mol/l
15% (w/w) GLY	1.868	mol/l

granulosa cells appear to be relatively permeable to glycerol as compared to the adherent endothelial cells in Fry et al. [68]. This difference suggests that granulosa cells could have a permeability to glycerol that is more similar to that of other common CPAs but the exact value is unknown; because of this, I used the same permeability values for ethylene glycol and glycerol in granulosa cells. Table 3.4 above contains all the experimental permeability parameters used in this model.

The interstitial (i.e. reaction-diffusion) and transmembrane transport (i.e. 2P model) models are coupled together via a reaction term in the diffusion code using custom code I wrote in PhysiCell to communicate the uptake and secretion between the diffusion solver and our custom two-parameter model. This is performed by assuming a conservation of mass between the voxels containing a granulosa cell or between the multiple voxels contained within the granulosa cell. In this model I assume that salts are impermeable on the time scale of CPA equilibration; this has been demonstrated as a reasonable assumption in oocytes as well as other cell types [27, 50, 70, 108].

Since this model contains two cells of very different size — granulosa cells are approximately 10  $\mu\text{m}$  in diameter, and the oocyte is on the order of 100  $\mu\text{m}$  in diameter, the larger oocyte cell type is considered to be made of multiple voxels (voxel rasterization), whereas the granulosa cell is approximately the same size of a single voxel. The voxel size is uniform and set to be just a little larger than a granulosa so that on average a single granulosa is contained within a single voxel. A granulosa cell is said to be located in the voxel whose

center is closest to that of the cell center (lattice-free, center based agents). Alternatively, the oocyte is said to be located in all the voxels contained within its boundary. In order to offset the effects of having multiple cells whose edges may be in the same voxel, external concentrations are averaged. While, cell boundaries may not fall exactly within one voxel, and granulosa cells could in theory occupy the same voxel, the amount of uptake (or secretion) per voxel in a single time step is thought to be sufficiently small that should multiple cells be considered part of the same voxel the error is still relatively small. Mass is always conserved; i.e. cells whose centers are in the same voxel would equally split the uptake of that voxel. Error due to how much of the voxel is occupied by a cell is partially accounted for in the model by multiplying the uptake in an occupied voxel by the fraction of cell volume to that voxel's volume. The oocyte's uptake is averaged over all the voxels contained within its cell boundary. The uptake in the  $i$ th voxel,  $U_i$ , is approximated with the following equation:

$$U_i = \begin{cases} \sum -S_n/V_i & \text{if granulosa cell,} \\ \sum (-S/N)/V_i & \text{if oocyte cell .} \end{cases} \quad (3.6)$$

Where  $S_n$  is the number of moles uptaken by the  $n$ th cell,  $N$  is the number of voxels within the oocyte,  $S$  is the number of moles uptaken by the oocyte and  $V_i$  is the volume of the  $i$ th voxel. For a granulosa cell, the  $i$ th voxel contains all the  $n$ th cells; for an oocyte  $N$  cells are contained within the oocyte boundary. Secretion is treated as a negative uptake.

Lastly, it is important to note that, while cells do change in volume, a standard assumption in the 2P model is that the surface area of the cell remains constant. This constant surface area is somewhat debated in the literature but is the standard approach previous models have used [27, 108, 116]. While it is relatively straightforward in theory to adapt a changing cell surface area in this model, the correct formulation is difficult to determine, particularly as spherical cells are only an approximation of the true cell shapes. As seen in microscopy images, like that in Figure 3.1, granulosa cells are only roughly spherical during CPA equilibration.

### 3.3.3 Mechanics

For the purpose of mechanics, I assumed that cells are connected to all of their immediate neighbours. In this case, this assumption results in roughly hexagonal neighborhoods [97]. The granulosa cell neighbourhood is assigned by connecting granulosa cells that are within 2 granulosa cell radii of each other, as measured along a path directly from the center of a granulosa cell to center of its potential granulosa neighbour. The oocyte neighbourhood is similar but instead of a neighbourhood distance extending 2 granulosa cell radii from the oocyte center, neighbours are located a distance that extends from the oocyte center outward a length of the oocyte radius plus  $10\ \mu\text{m}$  (the initial diameter of a granulosa cell). Any granulosa whose center falls within the oocyte's neighbourhood distance is connected to the oocyte. For clarity, in an ideal hexagonal neighbourhood of same sized rigid spheres, an interiorly located sphere would have 12 neighbours [46].

Cells located on the exterior of the follicle received a spring force directly outward from the center of the tissue such that the spring was attached to outermost point of the cell membrane (plasma membrane); the spring approximated the basement membrane (basal lamina), while all other connections were springs attached to neighbouring cells and extend directly along the shortest path between neighbouring cell centers. The cell-to-cell connections are approximated as an ideal frictionless springs governed by Hooke's law [89]. In order to account for the mass term in force calculations, I used a relative spring constant which contains the mass term (Equation 3.6, below). In order to account for the significant difference in mass between the oocyte and its neighbours without a mass term, the oocyte spring force was only applied to the oocyte's neighbours. Using a relative spring constant assumed a constant mass. While this is not biologically true, I assumed the change in mass would impact the force negligibly relative to the spring constant. The relative spring constants are  $k_{\text{TZP}}$ ,  $k_{\text{Granulosa}}$ , and  $k_{\text{Basement}}$  and correspond to the connection between the granulosa cells and the oocyte, the connection from granulosa-to-granulosa and the connection between the outermost granulosa and the basement membrane, respectively. The spring force is assumed constant during a simulation time step; this allows the relative spring constant to be translated directly into a per-time-step velocity as follows, where  $\Delta x$  is the distance the spring has been displaced from its rest length:

$$\begin{aligned}
F &= ma && \text{(Newton's Second Law),} \\
&= -k\Delta x && \text{(Hooke's Law),} \\
a &= -k\Delta x/m, \\
a &= -k_{\text{rel}}\Delta x, \text{ where } k_{\text{rel}} = k/m \text{ and } m \text{ is assumed constant.}
\end{aligned} \tag{3.7}$$

Assuming constant acceleration over the time step,  $dt$ , since

$$\begin{aligned}
a &= \frac{dv}{dt} \\
v_{n+1} &= v_n + a dt \text{ at the } n + 1 \text{ step then becomes} \\
v_{n+1} &= v_n + k_{\text{rel}}\Delta x dt \quad \left(\text{from } v_{n+1} = v_n + \frac{dv}{dt} dt\right).
\end{aligned} \tag{3.8}$$

Figure 3.3 shows a schematic of the spring set up.

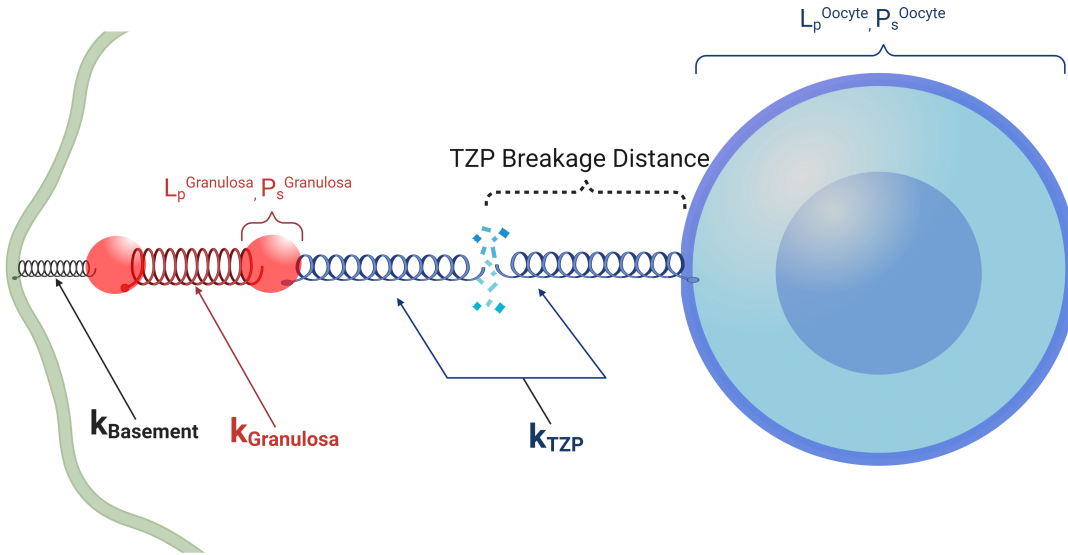


**Figure 3.3:** Schematic shows three springs with their corresponding spring constants. The wavy green line represents the basement membrane of the follicle. Red spheres are granulosa cells and the large blue spheres is the oocyte. The color of the parameters match the color of the cell type to which they correspond.

The basement membrane springs and granulosa-to-granulosa springs remained intact regardless of their displacement length but those between the granulosa cells and the oocyte were allowed to break. The granulosa-to-oocyte springs represent the TZPs and therefore had a fixed breakage distance set to  $10 \mu\text{m}$

which corresponded to both the isosmotic diameter of an average granulosa cell and the initial diameter of all granulosa cells in my model. Additionally, this breakage distance aligned with the TZP lengths measured in antral follicles by Baena and Terasaki [13]. By definition, the distance between two cell membranes,  $\epsilon$  is given by

$$\epsilon = \|\mathbf{x}_2 - \mathbf{x}_1\| - r_1 - r_2, \quad (3.9)$$

where  $x_1$  and  $x_2$  are the location of two neighbouring cells and  $r_1$  and  $r_2$  are the corresponding radii. The spring rest-length,  $x_r$  is set equal to epsilon at time  $t = 0$ . The  $x_r$  value can never be less than  $-0.2\mu\text{m}$ , the allowed cell overlap. This overlap represents approximately 20% of a granulosa cell's initial diameter. When  $\epsilon$  is larger than  $x_r$  the spring force is an attractive force between the two cells attached to the spring. Conversely, when  $\epsilon$  is smaller than  $x_r$  the force is repulsive. If  $\epsilon$  is equal to  $x_r$  then the spring force is 0, since this corresponds to no displacement of the spring from rest. Allowing the cells to overlap was a more realistic way to approximate compressible cell morphology. By adjusting the both the stiffness of the spring via the spring constant, and the amount of cell-to-cell overlap, different types of intercellular connectivity can be approximated.

In order to compare damage in TZPs between my model and experimental data, I computed a model TZP score. The model TZP score is the total number of intact TZP springs (granulosa-to-oocyte springs) at a given time divided by the initial number of TZP springs, where the initial number of TZP springs is equal to the number of granulosa cell neighbors the oocyte has at the start of a given simulation.

During simulation the position of the cells changes continuously (Figure 3.4). However, despite being continuous, this movement seems to grow smaller in magnitude as the cell volume reaches equilibrium.

It is important to note that while a cartesian mesh (lattice) is used for calculating diffusion and simulating the environment, this model is considered "lattice free" since agents do not need to fully occupy a particular voxel and in fact, can overlap or stretch over multiple voxels. While lattice-free modeling can complicate mass transport calculations it is vital for the accurate modeling of cellular motion.

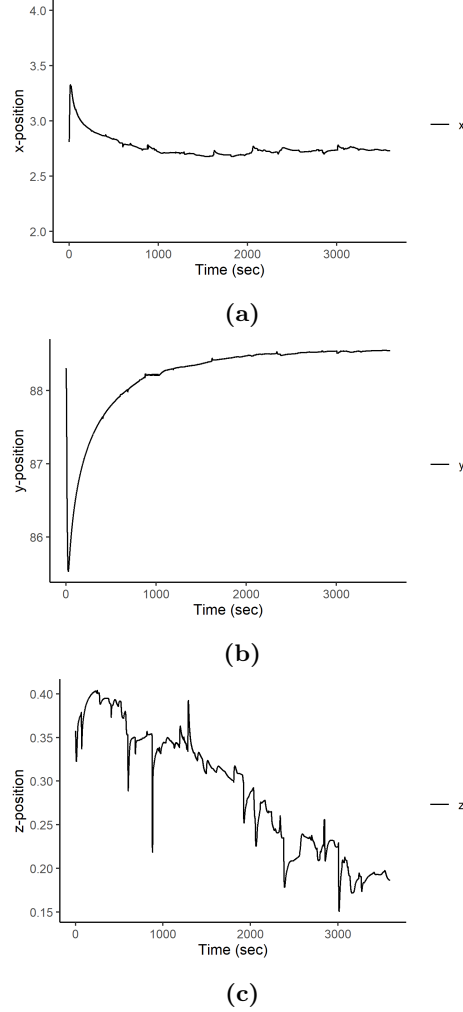


**Figure 3.4:** Change in position of a granulosa cell during an hour long simulation equilibrating in 15% ethylene glycol. (a) Shows x-coordinate, (b) y- coordinate, and (c) z-coordinate of the granulosa cell.

### 3.3.4 Toxicity Model

A significant portion of the cell damage that happens during CPA equilibration is the result of CPA toxicity. Previous work by Benson et al. [30] and Higgins et al. [85] has shown that the toxicity damage done by cryoprotective agents is concentration and time dependent and can be estimated with a toxicity cost function. This function relates a cell's history to accumulated damage due to CPA induced toxicity. The toxicity cost function is given as

$$J_{\text{tox}} = \int_0^{t_f} C_{\text{CPA}}^\alpha dt. \quad (3.10)$$

In this function the toxicity cost,  $J_{\text{tox}}$ , is dependent on the accumulated toxicity induced by the intracellular CPA concentration,  $C_{\text{CPA}}(t)$ , over time  $t = 0$  to  $t = t_f$ .  $C_{\text{CPA}}$  is the intracellular CPA concentration. While the toxicity parameters have not been measured for primate oocytes or granulosa cells,  $\alpha = 1.6$  has been shown to approximate the damage well in plated endothelial cells [51]. Thus I used this value as a placeholder until toxicity measurements can be made in this tissue type. By including a toxicity function my model could account for CPA toxicity as well as mechanical damage to TZPs when designing and simulating improved CPA equilibration protocols.

### 3.4 Testing and Construction of the Model: A road map for future agent-based models

Agent-based models of tissues are complex and involve multiple discrete components that can be built and tested individually before being combined into a single model. This modularity gives agent-based models a great deal of flexibility in customization but requires extensive testing of each piece before final implementation. In my model, I have constructed an “average” preantral ovarian follicle with 3-4 layers of granulosa cells. Theca cells and any tissue elements that would be outside of the follicles basal membrane are not included.

The first component of the model that I constructed was a single oocyte utilizing basic, built-in diffusion and with volume change governed by the 2P model. This oocyte was constructed using the parameters from Karlsson et al. for denuded oocytes from rhesus monkeys [108] and my model was able to match Karlsson et al.’s published results for a single denuded immature oocyte (data not shown). The oocyte constructed in this model was also tested with human metaphase II oocyte parameters (data not shown) [146].

After validating the 2P volume model with just a single cell, custom mechanics were constructed for the tissue. While PhysiCell does have built in cell-to-cell interactions, the default neighbour function assumes a general homogeneity of cell size in the tissue and takes advantage of adjacent mechanical voxels to determine these neighbors. Since the cell types in follicles are extremely different in size (i.e. oocyte vs granulosa) and PhysiCell assigns neighbours assuming similar sized cells a custom neighbour function was implemented.

This custom neighbour function required changing the core code of PhysiCell to add custom vectors to the cell-agent objects. I also constructed a custom velocity function that used these custom neighbours.

Note that PhysiCell is designed to update cell velocities at each time step, not cell forces, in order to simplify calculation, the assumption is made that during each time step the force remains constant (see equation 8). Since simulating many thousands of cells is computationally demanding and can make finding errors slow and difficult, I constructed a toy model to test the mechanics function. This toy model consists of a single oocyte and four granulosa cells lying along orthogonal axes such that all adjacent cells are neighbors (Figure 3.5). The implementation of the intercellular springs was tested using this toy model.

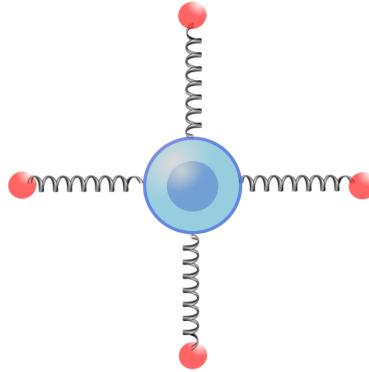


**Figure 3.5:** This set of 5 cells (1 oocyte in blue and 4 granulosa cells in red) serves to test the neighbourhoods and spring connections between cells. Cells are not to scale.

One difficulty in using Hooke’s law with a custom velocity function was accounting for the resting length of the springs. I opted to modify the core code of PhysiCell by adding a vector to store the initial distance between a cell and its neighbors and setting this distance to be the rest length. These modifications do make the initial set up phase of a given simulation significantly slower as they require looping through every cell and comparing it to every other cell to ascertain their relative positions. However, after this initial set up, velocity calculations and neighbour comparisons may be handled with some degree of parallelization which is quite rapid, since it is only restricted in speed by the number of neighbours attached to a given cell.

Next, I developed code to link the diffusion solver and two-parameter model for multiple cell types with multiple simultaneous permeating solutes. The 2P model was initially coded to be solved with a forward-Euler method, but I converted the 2P model to using an Adams-Bashforth second order method for increased

accuracy. Initially the 2P model handled only one permeating CPA, and this was rewritten as a vector version to simultaneously handle multiple CPAs and non-permeating treatments. Initial versions of the linked code between the diffusion solver and the 2P model were overly complex and difficult to parallelize. Eventually, I coded a simple mass balance between the 2P uptake and the voxel(s) containing the cell, with an error correction for volume differences between the voxel and cell (Equation 3.6).

Lastly, all of the model components were tested together in a 2D version of the follicle. This 2D model was a single cross section of the tissue and comprised of approximately 150 cells. The 2D model was relatively computationally slow due to a lack of consistent parallelization and the fact that the model relied on several large add-on arrays that made scaling difficult and did not correctly account for the 3D voxel uptake. As such, I further modified the core code of PhysiCell to allow additional new vectors to be attached to cell-agent objects, as well as to allow for complete parallelization of every custom function except for populating the vectors listing neighborhoods and the initial rest lengths of simulated intercellular connections. This allowed for a scaling of the 2D model into the fully functional 3D model.

### 3.5 Overview of 3D model

PhysiCell takes advantage of the fact that, within a single time step, computing the cell's state can be done in parallel as long as the information from the previous time step is fixed and stored. Almost all of the custom code I added to PhysiCell takes advantage of this parallelization by storing state values, and in some cases previous time step state values, as part of the cell object. Within each time step multiple states are being calculated by functions that must pass information between themselves before the final state for cell at that time is calculated. For example when calculating the amount of volume change that occurs in a cell, the volume state calculation requires determining the exterior concentration of solutes from the diffusion model, modifying the cell volume model and then passing that information back to the diffusion model before finally updating both the cell volume and the diffusion model. Because the code is trying to solve all of the different agent and microenvironment states before updating their new values its important that careful consideration be given to the order in which functions run. Figure 3.6 shows a schematic of the code run order.

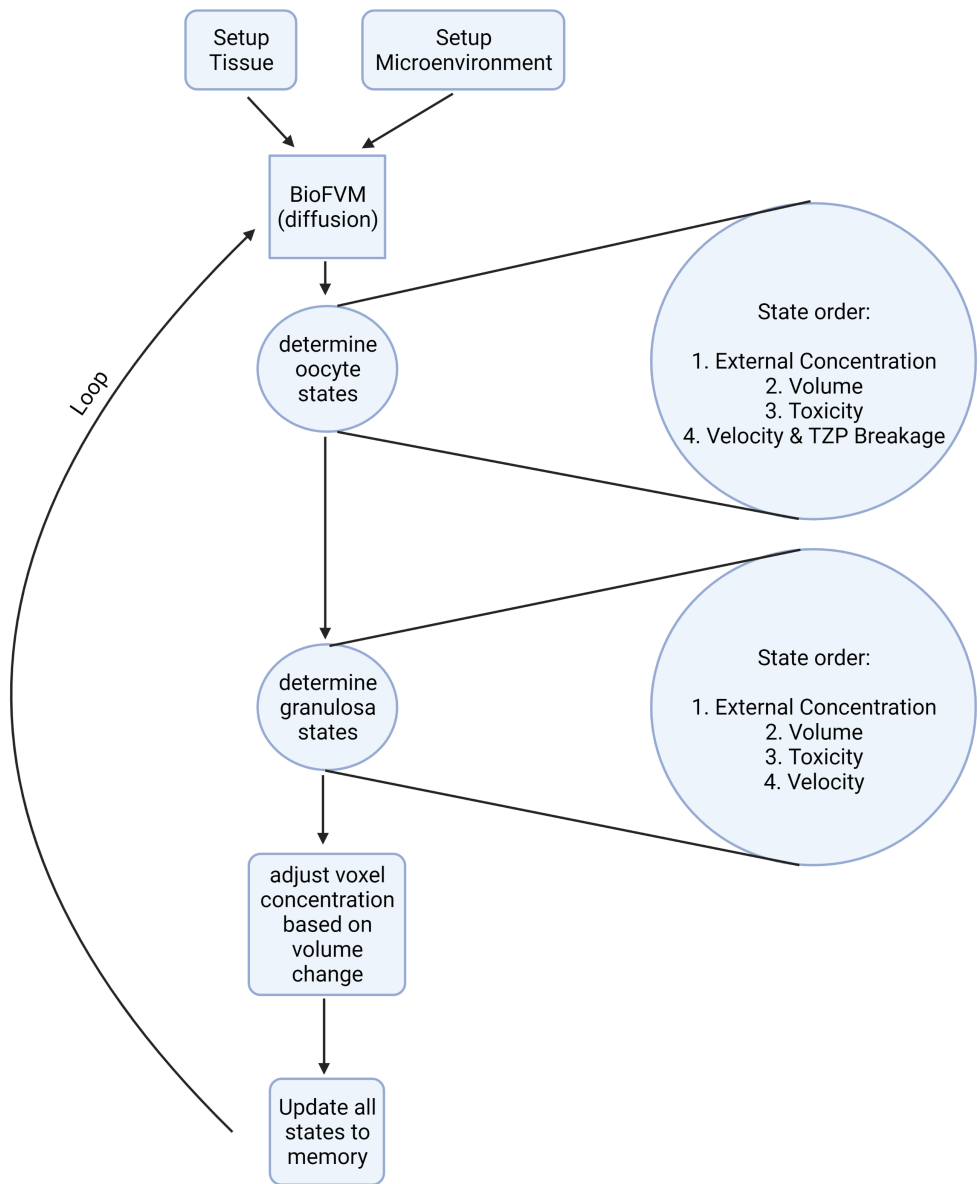


**Figure 3.6:** Flow chart of code run order. It is important to note that while each state is calculated in parallel, some states must be done before others (i.e. toxicity is calculated after volume).

In each simulation, the microenvironment is created first. This microenvironment is the virtual volume containing the tissue as well as surrounding media and boundary conditions. The microenvironment is a discretized space in which the simulation occurs and represents the simulation domain. The default discretization for PhysiCell assumes that voxels, the 3D cubes that make up a single discrete unit, are the same volume as all the simulated cells. In preantral ovarian follicles the default is not a valid assumption due to the large heterogeneity of size between different cell types and this is corrected for in my uptake code.

After, creating the microenvironment, cell-agents are created in the “set-up tissue” step. The cells are created using a custom cell definition that has all of the cell initial conditions already set. First, an oocyte is created and placed in the center of the simulation domain. Second, a spheroid of granulosa cells is created. The granulosa spheroid uses face-centered close-cubic packing to assign the position of cells. However, in order to simulate the compressibility of cells, a slightly smaller radius than the actual cell radius was used for this positioning; this means the cells initially are placed with a small amount of overlap simulating the dense compressed packing of real tissues. The granulosa spheroid code is a modified version of previously published hanging drop spheroid code for simulating tumor necrosis [72]. The spheroid code here was modified to contain a void in the central region where the oocyte has been placed (Figure 3.7).

After placing the cells, the neighbors are found and stored in memory along with the membrane-to-membrane initial distance between each neighbor; as previously mentioned, these distances serve as the spring rest length since all simulations are assumed to begin with tissue at an osmotic and mechanical equilibrium. Similarly, the cells attached to the basement membrane (basal lamina) are added to the basal lamina vector list. This is the only step where PhysiCell is forced to go through all of the cells in series.

During a simulation, after the set-up has completed, the main loop of the simulation begins (Figure 3.6). Briefly, this loop steps forward in time by the smallest defined  $dt$  until the simulation ends. During this main loop all the parallel cell functions run, followed by the cell and microenvironment state update functions. Data, such as the cell position and volume can be exported at any of these time steps. Additionally, PhysiCell has several prebuilt data visualization mechanisms that can be run during this loop.

In more detail, the functions that are called during the main loop are run in the following order: First, BioFVM handles the diffusion of solutes among voxels, then all the cell states are calculated, then corrections

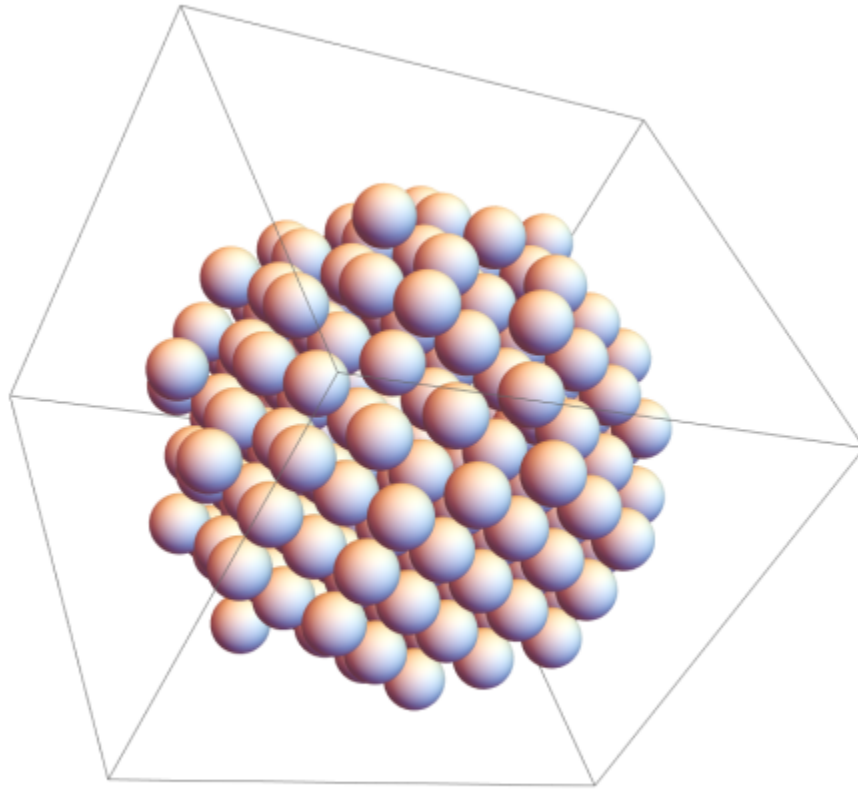


**Figure 3.7:** An exterior view of the simulated follicle (drawn using Wolfram Research, Inc., Mathematica, Version 12.3, Champaign, IL (2021)).

to the diffusion values are calculated and, finally, all the cell and microenvironment states are updated with these new calculated values. Cell states are determined in the following order: First, the mean concentration at the oocyte cell boundary is used to calculate the oocyte volume change and to update the toxicity cost function. Next, the velocities granulosa cells attached to the oocyte (TZP springs) are computed, and then the state change from the volume uptake is passed to the diffusion solver. Next, the same state calculations as done are done for the granulosa cells except here instead of TZP spring induced velocities the velocities from the granulosa-to-granulosa and granulosa-to-basement membrane springs are calculated instead. PhysiCell does allow for the calculation of diffusion, mechanics, and volume change to occur on slightly different time scales. However, there is no evidence to suggest that mass transport or cell movement happen on very

different time scales in the CPA equilibration of preantral ovarian follicles; so in the present model, all of the functions are run at each time step to simplify analysis and modeling.

### 3.6 Numerical Testing

Since agent-based models are often computationally expensive, even with parallelization, the development of accurate solvers and the correct selection of time and spatial step size is important. The core code of PhysiCell has been shown to be stable with second order convergence in time, and with satisfactory accuracy at time steps as large as 0.01 minutes [72]. The core code additionally has been shown to converge with spatial steps ( $dx$ ) as low as  $5\ \mu\text{m}$  and as high as  $40\ \mu\text{m}$ . Since granulosa cells are  $\sim 10\ \mu\text{m}$  in diameter this model conveniently uses a resolution  $dx$  that has been tested and shown to converge. The core code of PhysiCell can utilize multiple different time steps, for example diffusion can be updated every 0.01 seconds, while the cell mechanics is updated every 0.5 seconds.

In order to simplify the computation, I fixed all of the time steps in my code to a single time-step throughout all of the coded functions. I then ran multiple simulations of the whole follicle with  $dt$  at 0.01, 0.02, 0.04, 0.08, 0.1, 0.2, 0.4, 0.8 and 1.0 seconds the latter of which is slightly larger than the 0.1 minute time step shown to be accurate and stable in Ghaffarizadeh et al. [72]. In each simulation I compared oocyte volume as a proxy for measuring the error in my code. I assume that  $dt = 0.01\ \text{s}$  yields the true solution of  $V(dt)$ , the oocyte volume for a given  $dt$ , since the volume change of oocytes during model construction aligned with the literature data when using this  $dt$ . As such, the error in the volume can be computed as the mean absolute error (MAE):

$$\text{Err}(dt) = \frac{\sum_n^{i=1} |V(0.01) - V(dt)|}{n}, \quad (3.11)$$

where  $n$  is the number of simulated data points for a given  $dt$ . Results are presented in Table 3.6.

Here, it is clear to see that error remains extremely small and does not increase substantially under  $dt = 1.0\ \text{s}$ . Further, when cell volumes are plotted over time at these various time steps, the volume curves all show substantial overlap (Figure 3.8). In previous iterations of my model convergence held below 0.2 seconds, therefore 0.1 seconds was used as the time step; however, with the current code it may be possible for future simulations to use large time steps as the number of cell-agents demands.

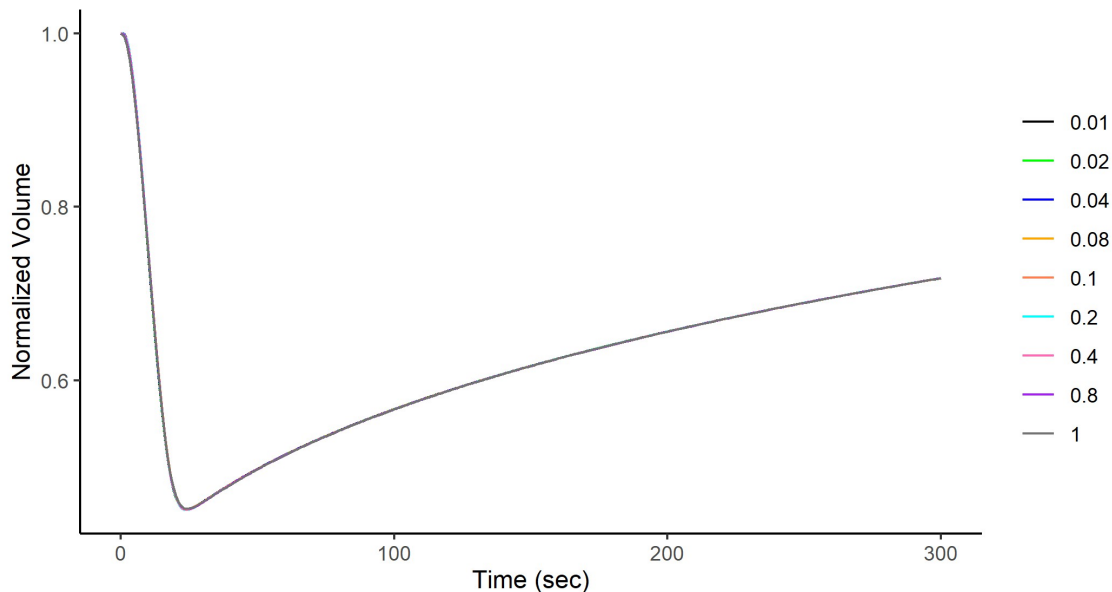


**Figure 3.8:** Normalized oocyte volume over time for different values of  $dt$  in seconds.

However, since rounding errors are a known issue in the current version of velocity calculations (Section 3.3) and this error increase as  $dt$  decreases (due to the multiplication of vector magnitudes much less than 1), there likely exists some optimal  $dt$  for the velocity function. Development of a velocity function without this numeric instability is already underway. The current velocity function results in a TZP score variation less than 1% at  $dt = 0.1$ . I did not attempt to adjust the  $dt$  further based on spring velocities.

### 3.7 Parameter Fitting

Using permeability parameters established in previous literature [68, 108, 215] and Chapter 2, I experimentally fit the model to determine three spring constants ( $k_{\text{Basement}}$ ,  $k_{\text{Granulosa}}$ , and  $k_{\text{TZP}}$ ) and their associate simulated TZP score to the experimentally determined mean TZP score as defined in Chapter 2 Section 2.4. As this would require a large computational time, an exhaustive search of all the possible parameters for all three spring constants was not possible. Instead, I searched smaller candidate regions of the parameter space with likely values. Based on the current parameter fitting, there are different spring parameters for single CPA treatments, multisolute treatments and nonpermeating treatments.

More specifically, fitting was done in multiple stages where two of the three spring parameters were held constant while the third was varied. Using a least sum of squares to fit spring parameters produced  $k_{\text{Granulosa}}$ ,

**Table 3.6:** Mean absolute error in oocyte volume calculated for different values of  $dt$ .

$dt$ (s)	Mean Absolute Error
0.01	0.0000000
0.02	0.0000483
0.04	0.0001316
0.08	0.0002568
0.1	0.0003077
0.2	0.0002802
0.4	0.0002781
0.8	0.0003536
1	0.0003864

$k_{TZP}$  and  $k_{Basement}$  values at 22 °C with exposure to permeating CPAs of 0.3, 0.05 and 0.6, respectively. A similar procedure was used to fit spring constants for the nonpermeating solution treatments, this produced  $k_{Granulosa}$ ,  $k_{TZP}$  and  $k_{Basement}$  values of 0.4, 0.045 and 0.6, respectively, at 22 °C. Non-permeating solution fitting followed the assumption that 0.5xPBS did not contribute significantly to TZP damage. This is a reasonable assumption despite this group showing damage in Chapter 2 since results were likely anomalous as 0.5xPBS did not show significantly more damage than control at either 37 °C or 4 °C. The multisolute mixture of ethylene glycol (EG) and glycerol (GLY) were simulated using the permeating CPA spring constants. The multisolute treatment was not included in fitting for the spring constants due to a high uncertainty in the multisolute permeability parameters. Upon fitting for the spring constants, the goodness of fit was assessed with an R-squared test, these results are presented below in Table 3.7.

**Table 3.7:** Results of R-squared for spring constant fitting. Note that for the nonpermeating spring fit, 0.5xPBS was given the same experimental TZP Score as 1xPBS.

	R <sup>2</sup>
Permeating Spring Fit	0.516
Nonpermeating Spring Fit	0.959

## 3.8 Simulation of Experimental Data

Using the fitted spring parameter values, I ran 300 second long simulated treatments of preantral ovarian follicles with my model. I simulated all of the room temperature protocols for ethylene glycol (EG), PBS, and glycerol (GLY) from the experiments in Chapter 2. Only room temperature treatments were simulated since the experimental results presented in Chapter 2 showed no statistically significant difference on TZP score for temperature. Additionally, previous literature did not report non-human primate permeability values for PBS near temperatures of 37 °C or 4 °C. In these simulations, I used published values for the oocyte hydraulic conductivity and solute permeability of PBS and ethylene glycol due to the small sample size and large variance in my experimental volumetric data [108]. I did however use the experimentally determined oocyte permeability values for glycerol from the experiments presented in Chapter 2. Again, granulosa permeability parameters were adopted from parameters for adherent endothelial cells based on the work presented by Fry and Higgins [68]. These parameters are listed above in Table 3.4.

The results of all the simulations using CPA equilibration data from Chapter 2 are presented in Figures 3.10–3.13; in each of these figures, I have included a grey dashed line in the plot of TZP score vs time showing the experimental TZP score as determined from the equilibration experiments in Chapter 2. In order to highlight typical granulosa cell volumetric change throughout the tissue, the normalized volume is presented from four sample granulosa cells along the simulation’s y-axis. Each sample granulosa cell is from a different granulosa cell layer moving from the most inward granulosa cell layer to most exterior, these granulosa are labeled (Figure 3.9). Figure 3.9 shows all the labeled volumes that can appear in the simulation volume plots in this chapter. Additionally, many of the simulation figures in this chapter show the mean TZP distance which I have defined as the average distance between the innermost surface of the innermost granulosa cells and the exterior surface of the oocyte; this length corresponds approximately to the distance that TZPs span.

Simulation of treatment in 15% (w/w) ethylene glycol showed a rapid shrink and then slower swell of both granulosa cell volume and oocyte volume. The granulosa cell volume change was more rapid than the oocyte. The whole follicle volume shrank and then swelled following the oocyte and granulosa cell response.

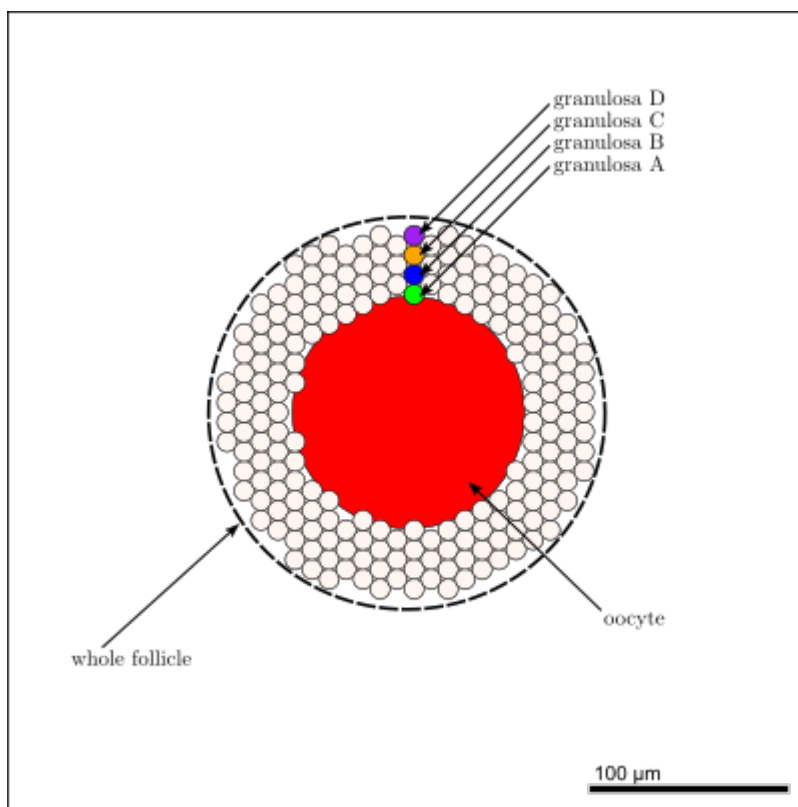
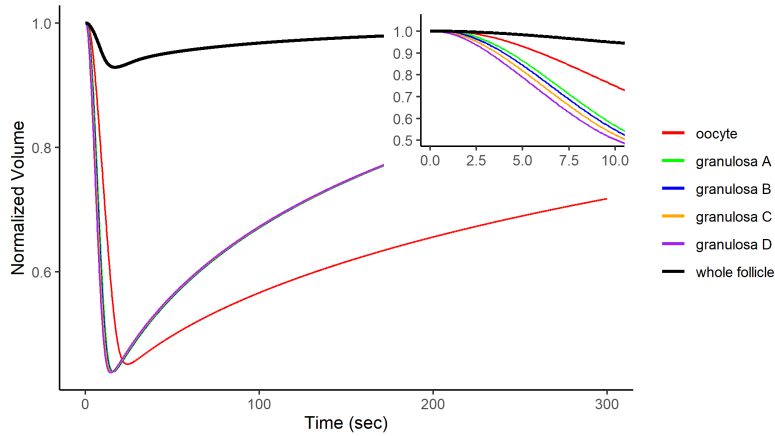


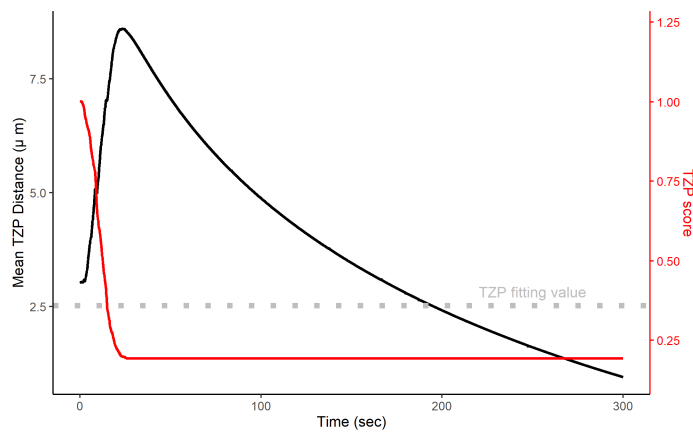
**Figure 3.9:** A 2D cross section of the simulated ovarian follicle that lies in the x-y plane (axis not shown). Sample granulosa cells, oocyte and whole follicle are marked in color.

However, the whole follicle volume reduction was much less than that of the cells having ended at a volume about 90% that of the initial volume. I observed that the delay in response between granulosa cell layers was small but detectable. The preantral ovarian follicle shrank symmetrically in the simulation, but the fit spring parameters substantially underestimated the experimental TZP score. The TZP breakage was based on the distance between the granulosa cell layers and the oocyte, with breakage predominantly ceasing once the minimum oocyte volume was reached. These results are shown in Figure 3.10.

Simulation of treatment in 15% (w/w) glycerol also showed a rapid shrink of both granulosa cell volume and oocyte volume however, the volume increase of the oocyte was slower than for the granulosa cells due to the permeability of the oocyte to the treatment being lower than for the granulosa cells. Whole follicle volume showed a similar response to treatment in ethylene glycol. The TZP breakage in the glycerol simulation occurred at about the same rate as initial decrease in volume, and the majority of breakage stopped when the oocyte reached its minimal volume; the minimum oocyte volume also corresponded closely to the maximum



(a)



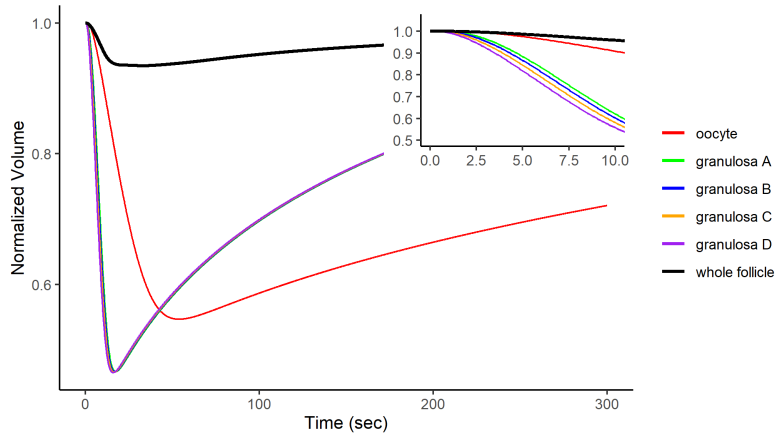
(b)

**Figure 3.10:** Simulation results for equilibration in 15% (w/w) ethylene glycol. (a) Shows the normalized change in volume for the whole follicle, oocyte and 4 test granulosa cells from each layer along the positive  $y$ -axis. (b) Shows the TZP distance and the mean TZP score where the dotted grey line is the associated experimental value for fitting mean TZP score under the same conditions.

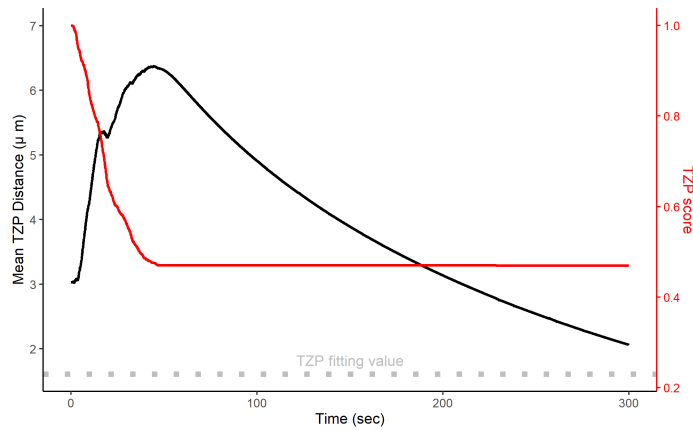
mean TZP distance. The simulated TZP score was substantially higher than the experimental mean TZP score. Simulation results are shown in Figure 3.11.

In this simulation the oocyte lost much less volume than in other simulations and began to return to isosmotic volume. The mean TZP distance remained relatively small. Using the experimentally determined permeability parameters from chapter 2, resulted in a much higher TZP score than the corresponding experimental results from the same chapter. Figure 3.12 shows results from a simulation of the combination of these two cryoprotectants using the spring constants found for permeating cryoprotectants.

The following simulations (Figures 3.13—3.16) represent equilibrations in varying concentrations of non-permeating solute. The nonpermeating solute used here was PBS. Equilibration with sucrose was not simu-



(a)



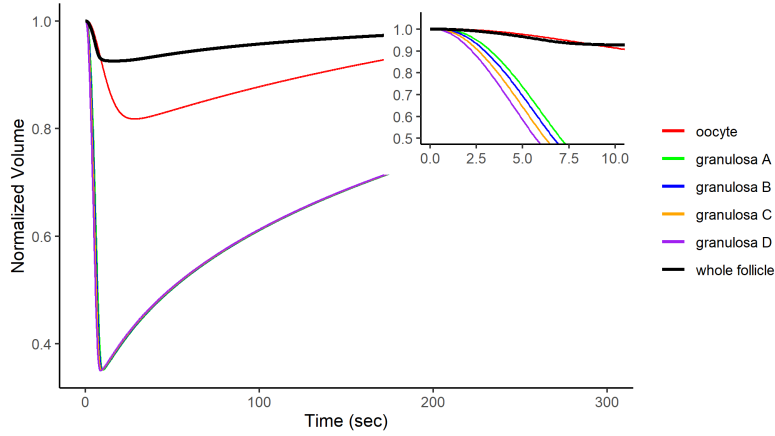
(b)

**Figure 3.11:** Simulation results for equilibration in 15% (w/w) glycerol. (a) Shows the normalized change in volume for the whole follicle, oocyte and 4 test granulosa cells from each layer along the positive  $y$ -axis. (b) Shows the TZP distance and the mean TZP score where the dotted grey line is the associated experimental value for fitting mean TZP score under the same conditions.

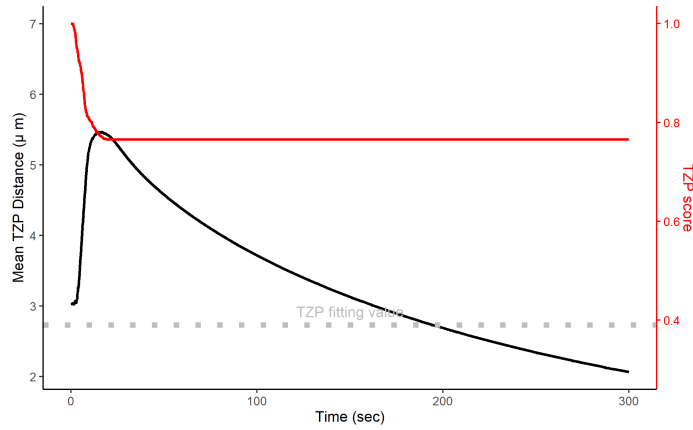
lated due to a lack of permeability parameters at the correct temperature.

In simulated treatment with 0.5xPBS the granulosa cells and oocyte swelled as predicted by the 2P model. The granulosa cells reached a maximum volume between 100 and 200 seconds in to the simulation. The maximum granulosa cell volume was slightly less than about 1.3 times the initial cell volume. The oocyte was still continuing to gain volume at the end of 300 seconds. The whole follicle volume increased slightly (less than 10%) and then decreased a very small amount. Additionally, this hypoosmotic media treatment simulation resulted in little to no damage to TZPs. The simulation results can be seen in Figure 3.13.

Simulated treatment with 1xPBS resulted in a fairly rapid shrinkage of the granulosa cells to between 80% and 85% of their original volume in less than 100 seconds afterwhich the granulosa cells remained at



(a)

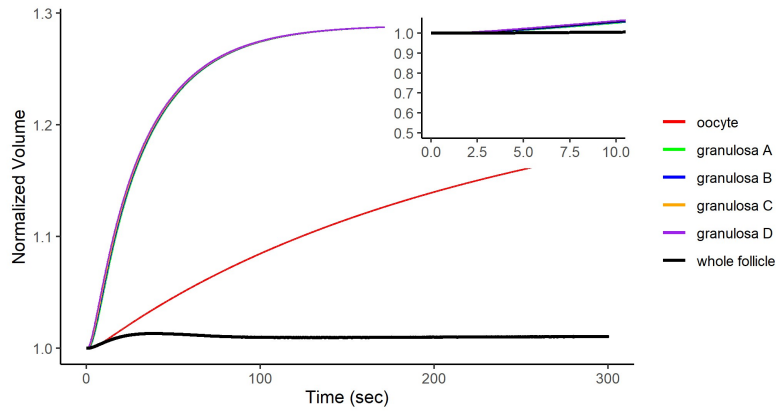


(b)

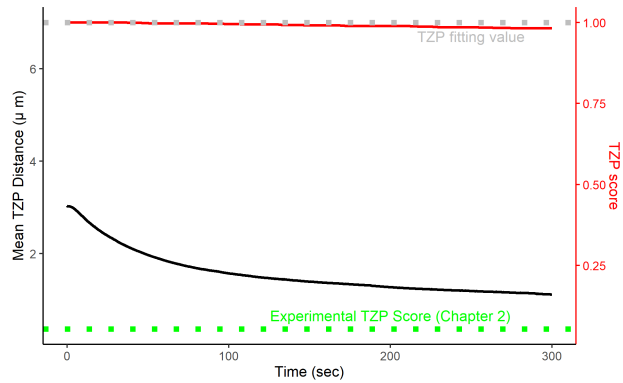
**Figure 3.12:** Simulation results for equilibration in a mixture of 15%et (w/w) glycerol and 15%et (w/w) ethylene glycol. (a) Shows the normalized change in volume for the whole follicle, oocyte and 4 test granulosa cells from each layer along the positive  $y$ -axis. (b) Shows the TZP distance and the mean TZP score where the dotted grey line is the associated experimental value for fitting mean TZP score under the same conditions.

this volume. The oocyte was still shrinking at 300 seconds, but had reached between 85% and 90% of the oocyte's original volume. Despite 1xPBS being the control, this treatment showed simulated volume change due to the difference between 1xPBS and holding media used in the experiment as presented in Chapter 2. TZP score is continuing down at the end of 300 seconds but is only slightly below 0.9 at the end of the simulation. Simulation results are shown in Figure 3.14

Simulated treatment in 2xPBS resulted in the whole follicle, oocyte, and granulosa cells reducing in volume to a minimum value and remaining there. The whole follicle shrank about 5% at a rate slower than that of either the oocyte or the granulosa cells. The oocyte reached a minimum volume slightly less than



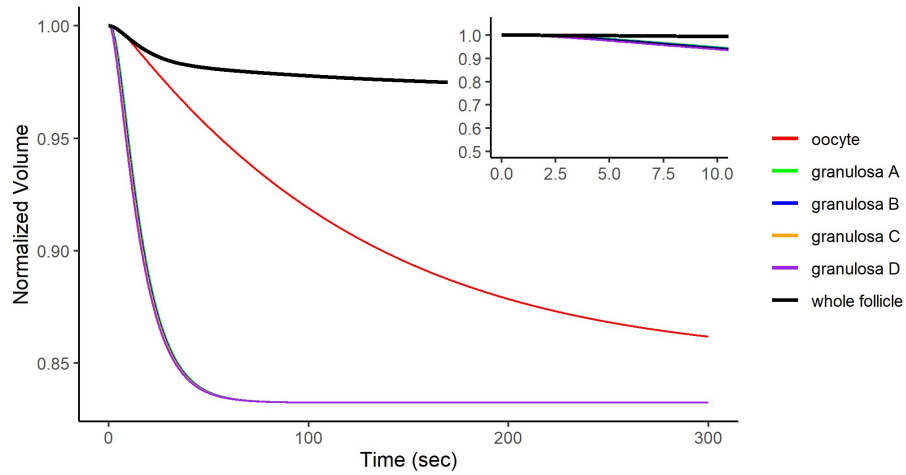
(a)



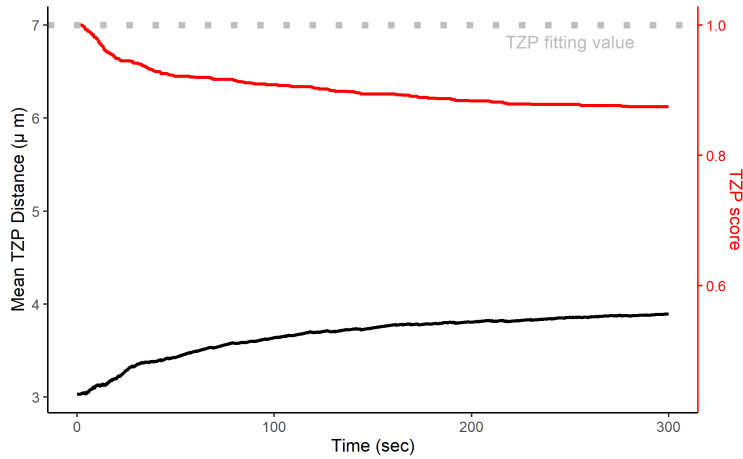
(b)

**Figure 3.13:** Simulation results for equilibration in 0.5xPBS. (a) Shows the normalized change in volume for the whole follicle, oocyte and 4 test granulosa cells from each layer along the positive  $y$ -axis. (b) Shows the TZP distance and the mean TZP score where the dotted grey line is the associated experimental value for fitting mean TZP score under the same conditions. Note that the green dashed line indicates the likely anomalously low mean TZP score from experiment (see Chapter 2); spring constants were fitted using the value at the grey dotted line.

60% of its initial volume between 100 and 200 seconds into the simulation. The granulosa cells reached a minimum volume between 50% and 55% of their initial volume in less than 60 seconds. The difference in volume response between the different layers of granulosa cells was very small but detectable. The mean TZP distance grew rapidly, shrank slightly at around 60 seconds then continued increasing till approximately the same time that the oocyte volume reached its minimum. Similarly, TZP score decreased until the maximum mean TZP distance was reached. The simulated TZP score was slightly higher than the experimental TZP score used for fitting.

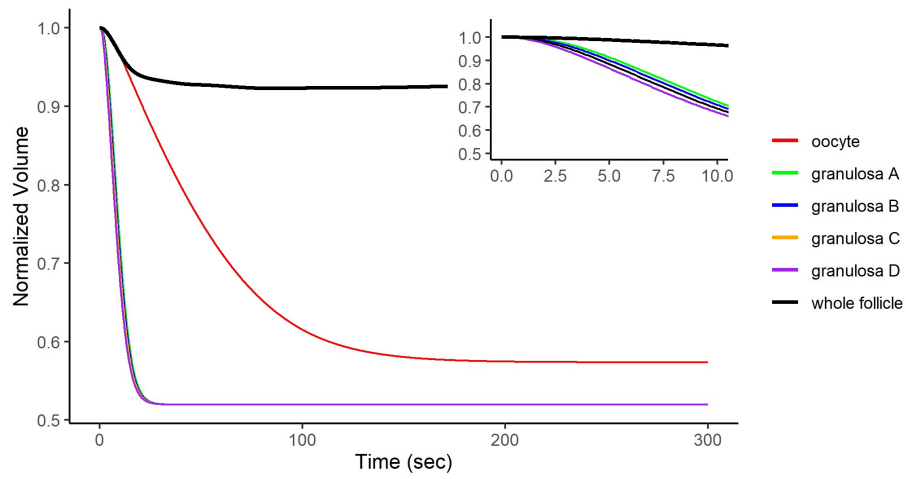


(a)

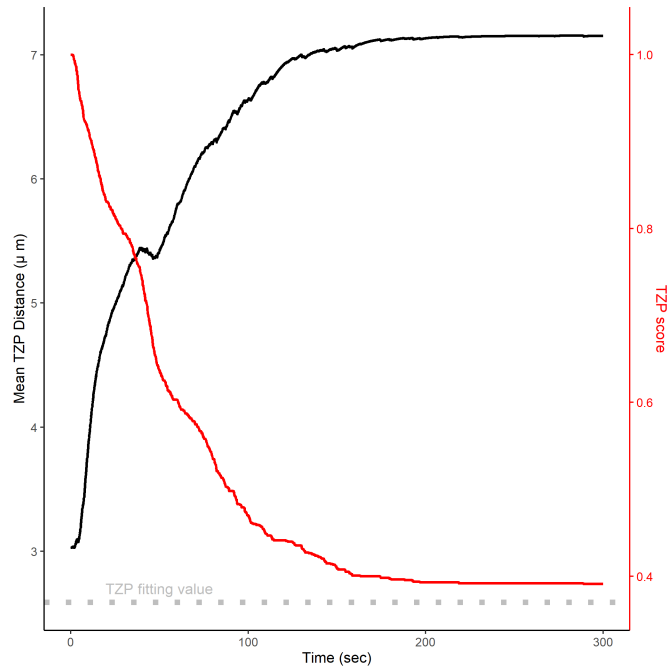


(b)

**Figure 3.14:** Simulation results for equilibration in 1xPBS. (a) Shows the normalized change in volume for the whole follicle, oocyte and 4 test granulosa cells from each layer along the positive  $y$ -axis. (b) Shows the TZP distance and the mean TZP score where the dotted grey line is the associated experimental value for fitting mean TZP score under the same conditions.



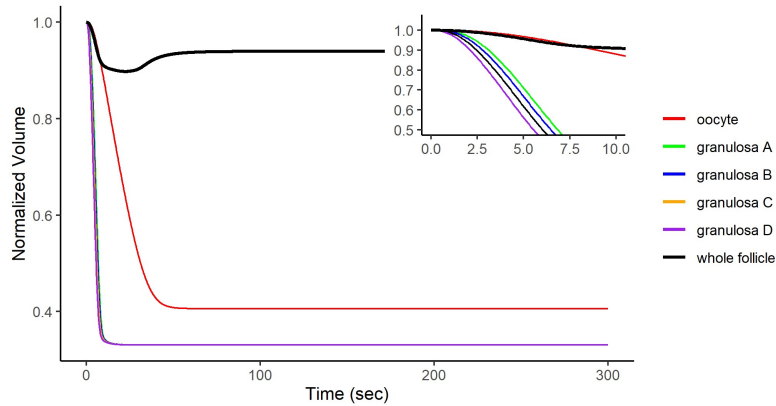
(a)



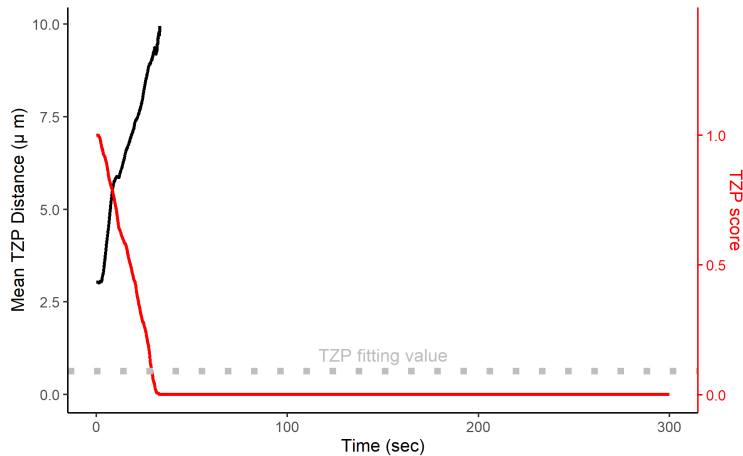
(b)

**Figure 3.15:** Simulation results for equilibration in 2xPBS. (a) Shows the normalized change in volume for the whole follicle, oocyte and 4 test granulosa cells from each layer along the positive  $y$ -axis. (b) Shows the TZP distance and the mean TZP score where the dotted grey line is the associated experimental value for fitting mean TZP score under the same conditions.

Simulated treatment of the follicle in 5xPBS produced a very rapid shrink in oocyte and granulosa cell volume. The oocyte reached a minimum volume of about 40% that of its initial volume in less than 60 seconds. The granulosa cells reached a minimum volume between 35% and 40% of their initial volume in less than 30 seconds. The whole follicle volume also rapidly shrank about 10% and then swelled slightly. The mean TZP distance exceeded the TZP breakage distance of 10  $\mu\text{m}$  rapidly resulting in all of the TZPs being broken. The TZP score was slightly lower than the non-zero mean experimental TZP score. Results of this simulation are in Figure 3.16.



(a)



(b)

**Figure 3.16:** Simulation results for equilibration in 5xPBS. (a) Shows the normalized change in volume for the whole follicle, oocyte and 4 test granulosa cells from each layer along the positive  $y$ -axis. (b) Shows the TZP distance and the mean TZP score where the dotted grey line is the associated experimental value for fitting mean TZP score under the same conditions.

Additionally, I used the toxicity parameter determined by Davidson et al. [51] and the toxicity cost function first presented by Benson et al. [30], to simulate accumulated toxicity induced by equilibration in

15% ethylene glycol. The accumulated toxicity increased steadily throughout the simulation and resulted in higher toxicity in the smaller volume of the granulosa cells than in the oocyte. The results are shown in Figure 3.17.

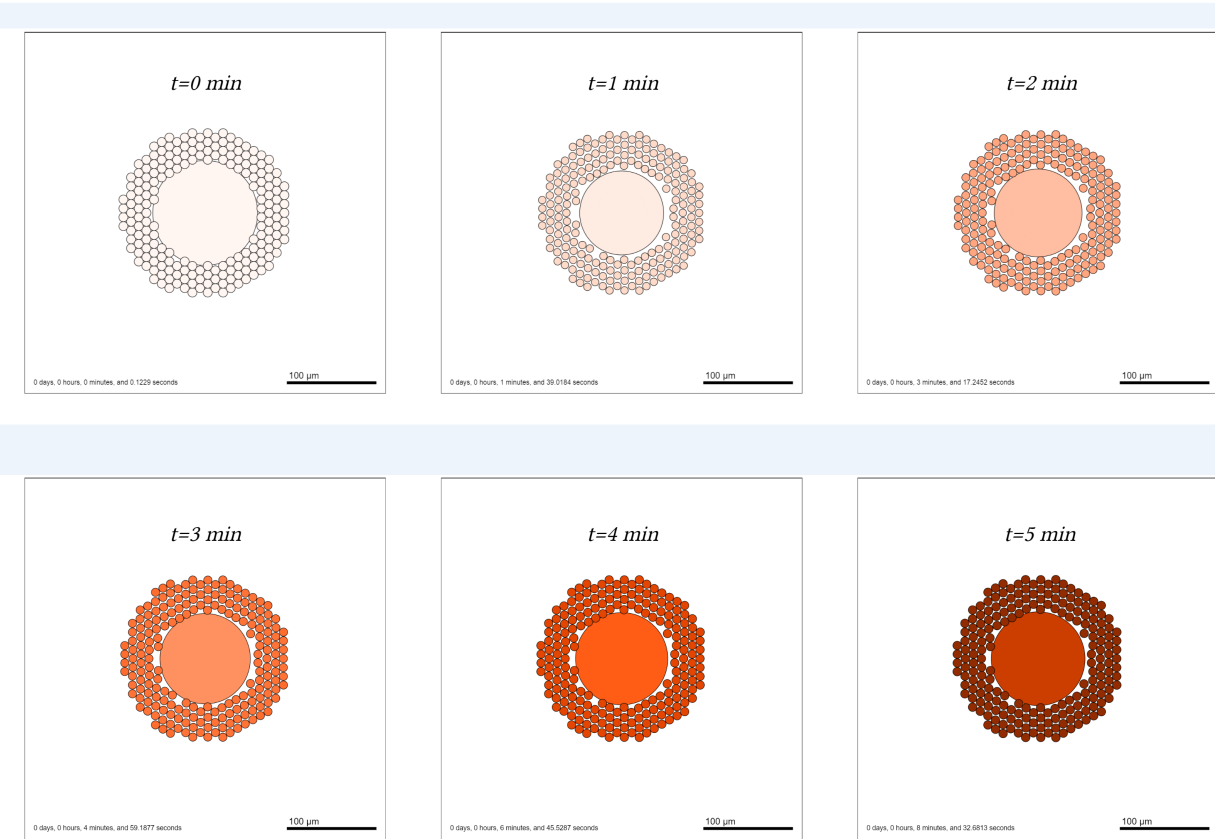


**Figure 3.17:** Time lapse cross section showing increasing toxicity (darkening color) in cells with time.

### 3.9 Further Modeling

In order to demonstrate why it is vital to include granulosa cells in modeling damage to TZPs, I simulated ethylene glycol equilibration with the granulosa cell uptake activated and deactivated as well as the granulosa mechanics activated and deactivated. The effect that granulosa cell uptake had on TZP score was small but detectable; deactivation of granulosa cell uptake appeared to very minutely lower the TZP score. Alternatively, deactivating granulosa cell mechanics, which involves deactivating the spring attachments to the basement membrane, the TZP springs, and the granulosa-to-granulosa springs resulted in a drastically

lower TZP score. The effects of these activations/deactivations are shown in Figure 3.18. In this tissue, the activation or deactivation of these features does not appear to alter the volume change despite altering the TZP score.

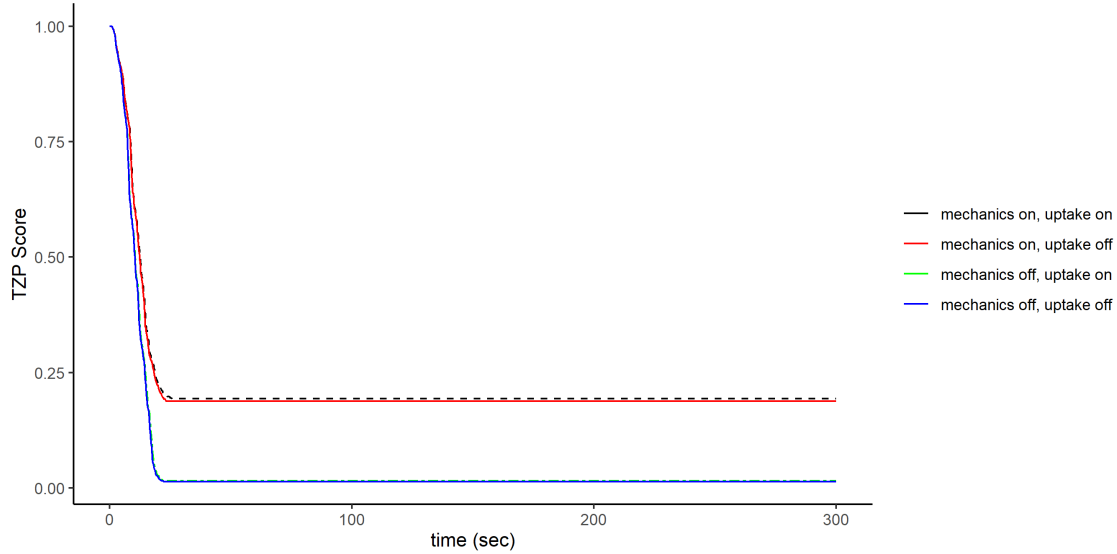
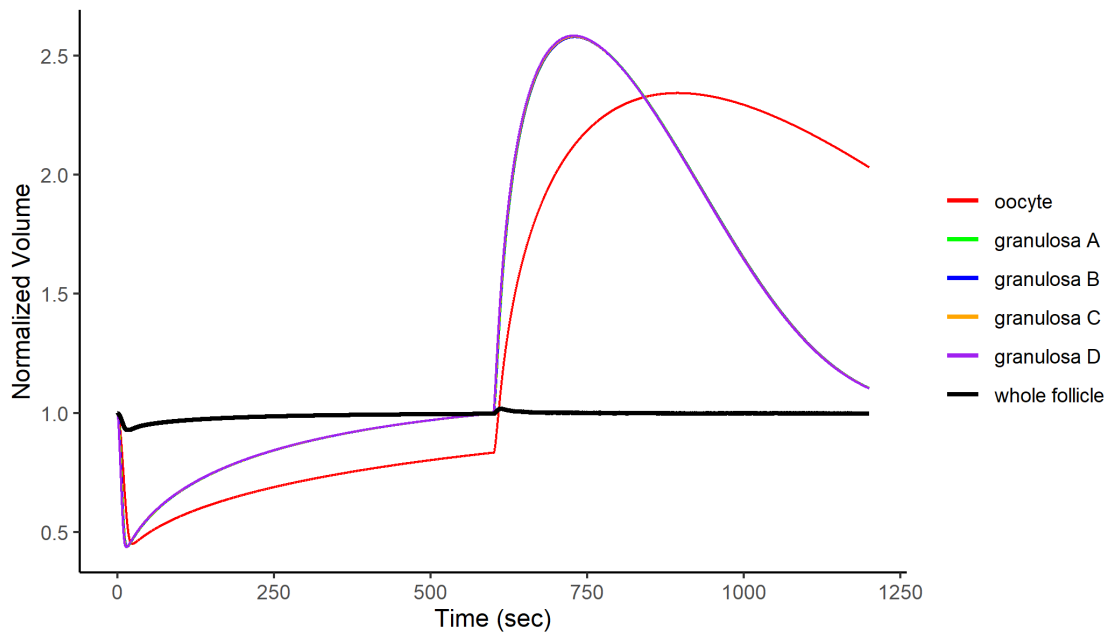
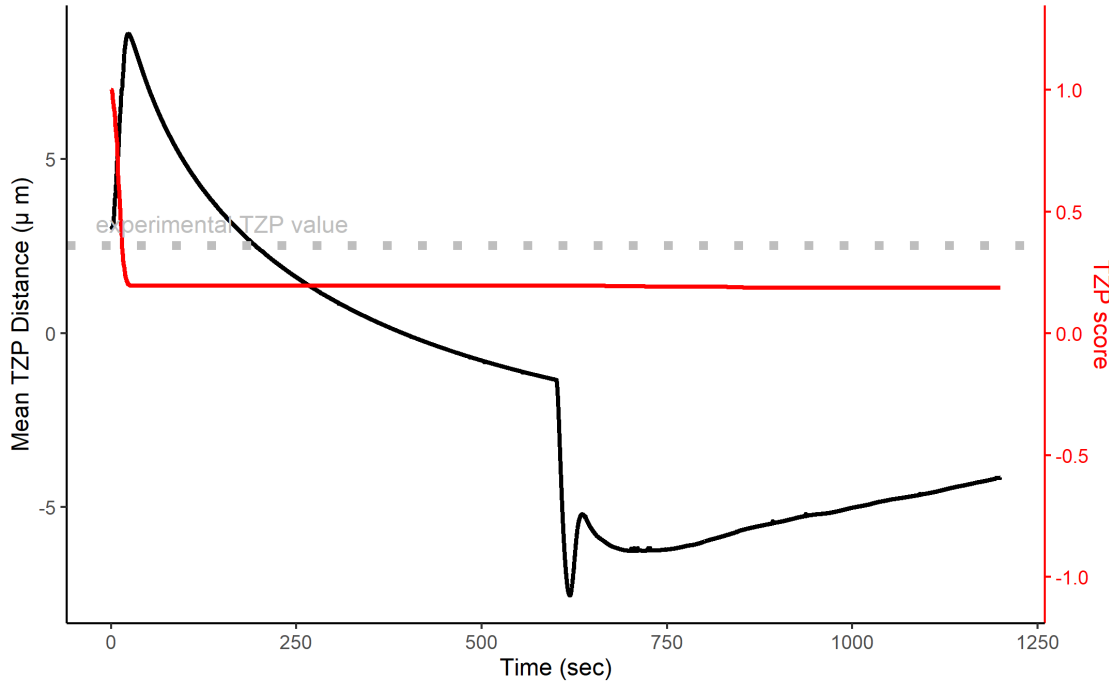


**Figure 3.18:** Changes in TZP score during equilibration in 15% ethylene glycol while activating/deactivating tissue mechanics as well as activating/deactivating tissue uptake.

In the experimental data collected and described in Chapter 2 it was highlighted that CPA equilibration resulted in all of the damage done to TZPs. In order to verify that this was the case in my model, I performed a simulated equilibration in 15% (w/w) ethylene glycol for 1200 seconds and then back to holding media concentration for an additional 1200 seconds. As shown in Figure 3.19, it is clear that TZP score decreased during the CPA equilibration and remained relatively constant while equilibrating back to holding media. The mean TZP distance increased as the oocyte shrank and then became negatively valued as the oocyte swelled into the granulosa cell layers. The swelled oocyte then began to push the granulosa cells outward. A number of granulosa cells in this simulation were pushed outside the basement membrane and “broke away” from the follicle.



(a)



(b)

**Figure 3.19:** Simulation of equilibration to Ethylene Glycol followed by equilibration in holding media. (a) Shows the normalized change in volume for the whole follicle, oocyte and 4 test granulosa cells from each layer along the positive y-axis. (b) Shows the mean TZP distance and TZP score, with a grey dashed line showing the expected TZP score from experiments.

### 3.10 Sensitivity of Parameters

To determine the sensitivity of the model to the permeability parameters I tested the model with hypothetical solutions of “high”, “low” and “normal” permeabilities for granulosa cells and the oocyte cell. The “normal” permeabilities are those used for simulating ethylene glycol while high permeabilities are double the typical literature values for ethylene glycol and the low permeabilities are half, these are given exactly in Table 3.8.

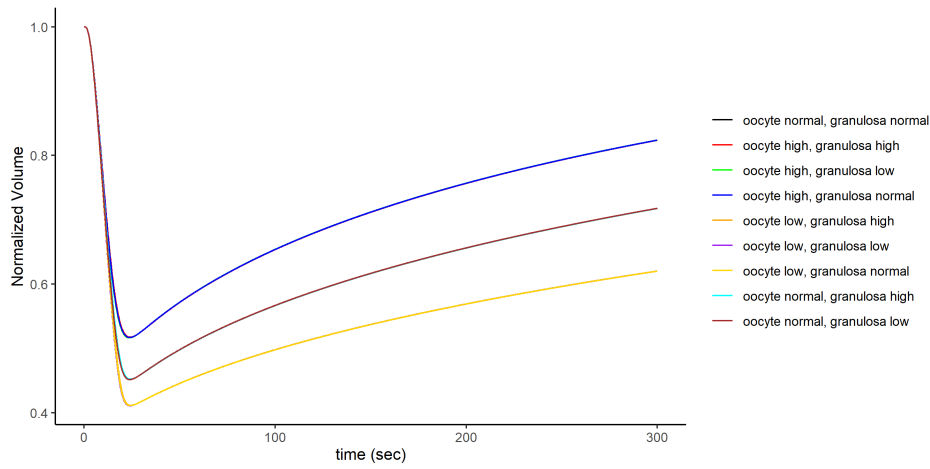
**Table 3.8:** The different permeability parameters that were tested to assess sensitivity.  $P_s$  was varied from typical ethylene glycol values by doubling (high) and halving (low) the value.

Cell Type	Parameter Symbol	Normal EG Value	High Value	Low Value	Units
Oocyte	$L_p$	0.0167			$\mu\text{m/s/atm}$
	$P_s$	0.12	0.24	0.06	$\mu\text{m/s}$
Granulosa	$L_p$	0.0029			$\mu\text{m/s/atm}$
	$P_s$	0.0345	0.069	0.01725	$\mu\text{m/s}$

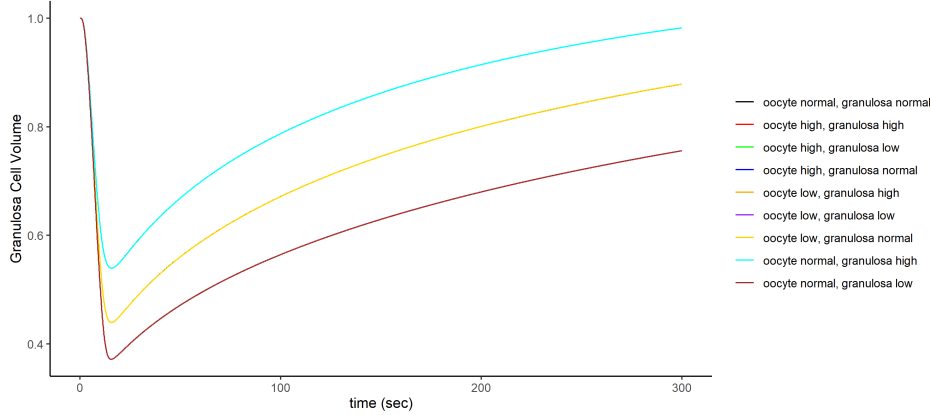
Permeability sensitivity tests showed that the volume change of the oocyte and granulosa cells were independent of each other (i.e., all “low” oocyte permeability volume curves overlap regardless of what the permeability of the granulosa cells are). TZP score depended on both the permeability of the oocytes as well as the permeability of the granulosa cells. Oocyte permeability had a larger effect on TZP score than granulosa cell permeability. Higher permeabilities for both granulosa cells and oocyte correlated with higher TZP scores. The following figure (Figure 3.20) shows the oocyte volume, a sample granulosa cell volume, and TZP score during the permeability sensitivity testing. Additionally, the final TZP scores for each of these sensitivity to permeability tests are presented in Table 3.9.

Increased permeability corresponded to a higher TZP score and decreased permeability corresponded with a decrease in TZP score. Changes in oocyte permeability had a stronger effect on TZP score values than did changes in granulosa cell permeability.

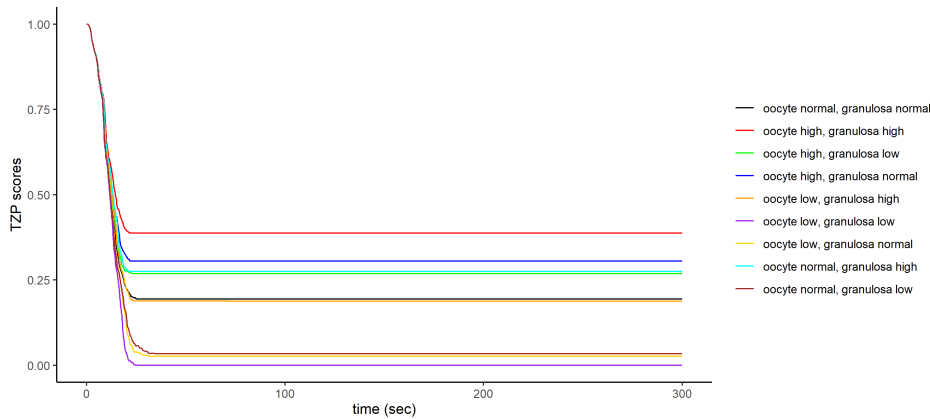
I also tested how sensitive my model was to variation in the spring constants. I measure the sensitivity as change in TZP score produced when the spring constants are altered. I performed several simulated equilibrations in 15% ethylene glycol, where two of the spring constants were held constant while the third



(a)



(b)



(c)

**Figure 3.20:** The oocyte and granulosa cell volume response and TZP score during equilibration in 15% ethylene glycol while  $P_s$  is halved (low), doubled (high) or remains the same (normal) for the granulosa cells and/or the oocyte. (a) Shows the oocyte volume response. (b) Shows granulosa cell volume response. (c) Shows change in TZP score.

**Table 3.9:** Table shows the TZP score of varying (or not varying) the solute permeability for the oocyte and/or granulosa cells up and down by 50%.

		Granulosa		
		normal $P_s$	High $P_s$	Low $P_s$
Oocyte	normal $P_s$	0.19	0.27	0.03
	High $P_s$	0.31	0.39	0.27
	Low $P_s$	0.03	0.19	0.00

was varied relative to the fitted values. TZP score increased non-linearly with decreasing  $k_{\text{Granulosa}}$ . Similarly, TZP score increased with decreasing  $k_{\text{Basement}}$ . TZP score decreased with decreasing  $k_{\text{TZP}}$ . Changes in  $k_{\text{TZP}}$  of 0.01 were on the same order as changes in the other two spring constants by 0.1. The results of these tests are presented in Table 3.10.

Phenomenological parameters such as overlap distance, neighbor radius and spring breakage distance are more difficult to test for sensitivity, because they alter the initial geometric conditions and initial neighborhoods of the tissue. Additionally, these parameters have cross effects with the spring constant parameters. A real cell can compress and stretch but that movement is captured in the TZP score by both the cell overlap and the spring constants. Additionally, real tissue connections in ovarian follicles are not necessarily to adjacent neighbors [13, 60]. TZP connections are actually more akin to complex “spaghetti”-like networks [13] (Figure 3.21). My model can only approximate these complex structures, and testing the sensitivity of these parameters is difficult to isolate and partially reflected in the sensitivity of the spring constants. As such, I did not test for sensitivity in regards to these other phenomenological parameters.

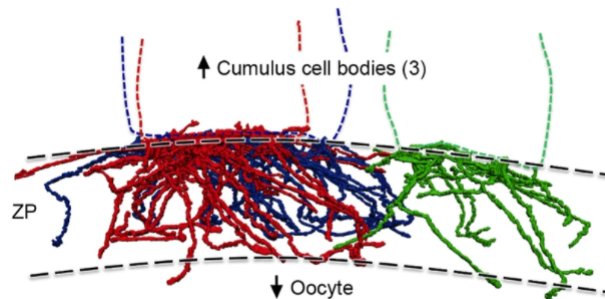


**Figure 3.21:** Reconstructed TZPs from electron micrographs. Figure used under Creative Commons licence from Baena and Teraski [13].

**Table 3.10:** TZP score varies as spring constants are varied from the fitted parameters. The dark band indicates the fitted spring constants. In each case, two spring constants were held fixed at the fitted value while the third was varied.

Vary $k_{\text{Granulosa}}$			
$k_{\text{Granulosa}}$	$k_{\text{Basement}}$	$k_{\text{TZP}}$	TZP Score
0.1	0.60	0.05	0.44
0.2			0.29
0.3			0.20
0.4			0.03
0.5			0.0
0.6			0.0
0.7			0.0
Vary $k_{\text{Basement}}$			
0.3	0.3	0.05	0.28
	0.4		0.25
	0.5		0.22
	0.6		0.20
	0.7		0.15
	0.8		0.00
	0.9		0.00
Vary $k_{\text{TZP}}$			
0.3	0.6	0.02	0.00
		0.03	0.00
		0.04	0.03
		0.05	0.20
		0.06	0.27
		0.07	0.31
		0.08	0.38

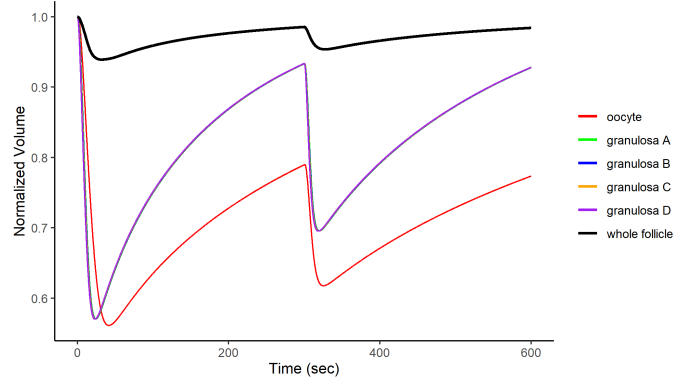
### 3.11 Theoretically Improved Protocols

Based on the simulations presented previously in this chapter, several different methods may be used for improving CPA equilibration by reducing TZP damage while maintain osmotic tolerance limits and reducing toxicity. One possible and standard method to find an improved protocol is to utilize multi-step equilibration. This can be done by adding CPAs in progressively higher concentrations. Varying the number and size of steps during equilibration results in different volumetric excursions between the granulosa and oocyte cells. Step-wise addition (equilibrating in increasing concentrations of CPAs) and step-wise CPA removal are common techniques in cryobiology [30, 99, 119, 195]. My simulations show that this method can be used to reduce damage to intercellular connections. I show examples of a 2-step CPA equilibration (Figure 3.22) where 15% ethylene glycol is reached in two 300 second steps; the first step is to half of the final concentration and the second step is to the final concentration. Additionally, I provide an example of a 4-step CPA equilibration where 15% ethylene glycol is reached in four steps of 300 seconds (Figure 3.23); in each step CPA concentration is increased by 1/4 of the final concentration. In the 2-step CPA equilibration TZP score did not substantially decrease after the first step which resulted in a TZP score of 0.50. In the 4-step CPA equilibration TZP score only decreased by less than 0.02 after the first step and the final TZP score was 0.74.

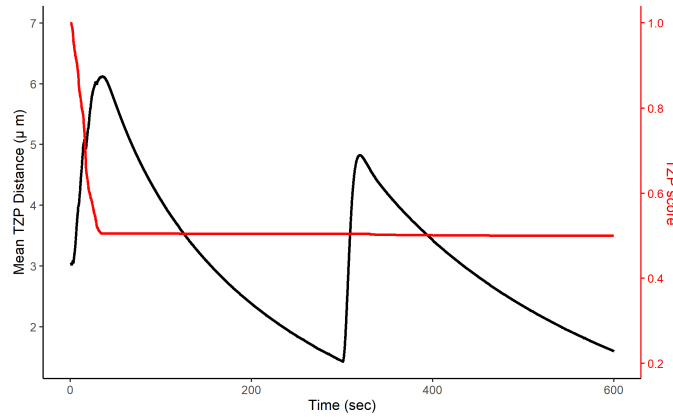
### 3.12 Discussion

The results presented in this chapter demonstrate that my model can capture the volumetric change and in some cases the TZP score for an average preantral ovarian follicle during hyperosmotic CPA equilibration. Using, these simulations I am able to generate hypothetical CPA equilibration protocols that can be used to reduce damage done to ovarian follicles via osmotic and/or mechanical damage and may additionally be able to minimize toxicity damage. In addition, as permeability and mechanical parameters are refined experimentally, theoretical model predictions can be improved.

Specifically, the simulations in this chapter suggest that minimizing the volume change of the oocyte is essential for minimizing the damage done to TZPs. Simulations in Section 3.8 and Section 3.10 show that TZP score, a proxy for TZP damage, is mostly highly correlated with the amount and rate of oocyte volume



(a)

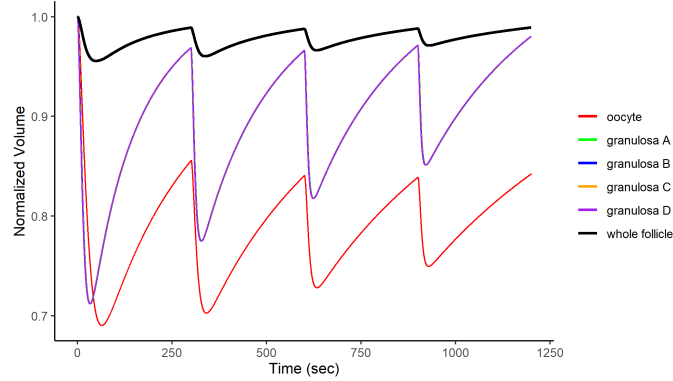


(b)

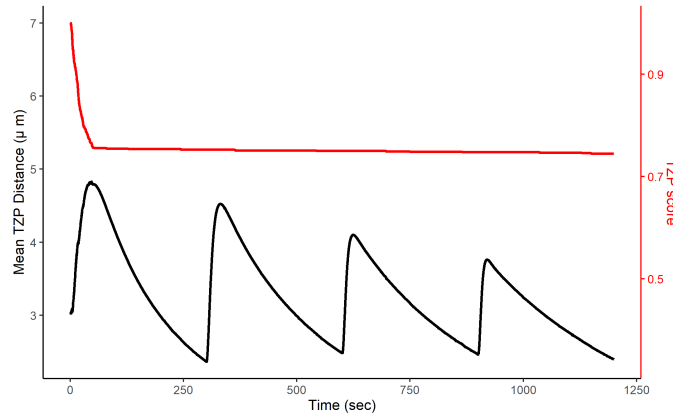
**Figure 3.22:** Simulation of 2-step CPA equilibration. (a) Shows the normalized change in volumes while (b) shows the mean TZP distance and TZP score.

change, and that TZP score decrease largely stops once the oocyte reaches its minimum volume. TZP damage appears to be highly influenced by oocyte volume however simulations show that capturing TZP damage during different protocols is not as straightforward as focusing solely on the oocyte. Accurate capture of TZP damage requires an understanding of the way in which granulosa cell layers move relative to the oocyte (Section 3.9) as well as the amount of volumetric change they experience. While granulosa cell movement is difficult to capture experimentally (Chapter 2), simulations suggest that TZPs are extremely sensitive to the connections between granulosa cells and the basal lamina, as well as between granulosa cells and the oocyte (Section 3.10).

A number of numeric issues emerged during the creation of my model that have been resolved or are in the process of being resolved. First, there is a slight variation of the TZP score between runs of less than 1% this is due to a rounding issue in the force calculation. Second, because custom variables in PhysiCell are



(a)



(b)

**Figure 3.23:** Simulation of 4-step CPA equilibration. (a) Shows the normalized change in volumes while (b) shows the mean TZP distance and TZP score.

not vectors it was difficult to track the initial distances between a cell and its neighbours. This meant either using an average rest-length, a rest length of zero where the cells are assumed to be just touching initially (i.e. no rest length), or modification to the core code of PhysiCell. While excluding a rest-length for each neighbour produced a workable model, the continuous oscillations of the springs contributed a fair amount of error to the movement of the cells. This highlights the fact that the springs in this model are undamped thus there will always be some motion of the cells. As mentioned earlier in this chapter the motion of the granulosa cells does seem to decrease as cell volume equilibrates. Third, during the setup phase of the tissue the neighbourhoods are assigned by code that runs through all the cells in order. However, since serially looping through all the cells is only done once, it does not create a significant computational bottleneck. Future versions of the code could be designed with a non-serial set-up phase but even testing with over 20,000 cells, far more than any preantral follicle, the set-up time is still relatively short (on the order of about

1-2 minutes on an average specification desktop computer).

Additionally, while the effect of granulosa cell uptake is relatively small within a small tissue like preantral ovarian follicles (Figure 3.18), the effect of cellular uptake on larger tissues scales with the size of the tissue (data now shown). This suggests that accounting for cell level mass transport is more significant the larger the tissue being modeled. While, this model does not account for other mass transport effects such as tortuosity as in Benson et al. [27], it is possible that these sorts of features may be an important addition to larger tissue models. Further testing on larger tissues could also indicate that a lumped tissue diffusivity term is sufficient to accurately capture these features with enough fidelity to make the model useful. With all modeling, there is a trade-off between computational resources and accuracy.

There are several important observations I made while fitting the spring constants. When fitting the spring parameters during any of the simulations, I observed that the majority of TZP breakage occurred before or at the minimum oocyte volume. I also observed a very rapid breakage during permeating CPA equilibration and a slightly slower but steady breakage for non-permeating solution exposure till the minimum oocyte volume was reached. If I set the  $k_{TZP}$  spring constant to a value that was too low relative to the basement membrane spring constant, all the TZPs broke within the first few seconds of simulation; alternatively if the inverse was true, hardly any TZPs broke resulting in a TZP score that was too high. My model was particularly sensitive to the ratio between the spring constants with the TZP springs being the most sensitive by about an order of magnitude (see sensitivity testing below).

Additionally, during experimental fitting it became clear that the appropriate spring constants to use for fitting varied between follicles exposed to a single permeating cryoprotectant, multiple cryoprotectants or solely equilibrated with non-permeating salts/solutes. Additionally, CPA spring constants fit far more poorly than the constants for non-permeating solutes. While surprising, there are a number of possible physiological reasons why this may be the case. First, since spring constants are phenomenological parameters describing what is actually a complex network of connections, it may be appropriate to have case-specific parameters. Second, previous work by Songsasen et al., Younis et al. and Karlsson et al. [108, 179, 215] has shown that non-spherical/non-symmetrical shrinkage occurs frequently in non-human primate oocytes during exposure to hypertonic, nonpermeating solutions as well as CPAs which may confound our experimental data; one

drawback of my model is that it lacks the ability to capture this non-spherical volume change. In Karlsson et al. [108] immature non-human primate oocytes showed greater non-spherical shrinkage when exposed to PBS than when exposed to ethylene glycol, however these sample sizes were very small. This non-spherical shrinkage in tissue may be caused by non-uniformity in the TZP connection strengths which my model cannot capture. Interestingly, Younis et al. was able to remove the occurrence of non-spherical shrinkage by pre-treating oocytes using EGTA [215], a calcium chelator. Additionally, the error in fitting CPA spring constants could be the result of my findings that glycerol was permeable. This finding is contrary to what Songsasen et al. and Younis et al. found [179, 215] and my sample size was small with high variability and could have been confounded by nonspherical shrinkage as elaborated on in Chapter 2. My CPA spring constants are extremely sensitive to the permeability values for either GLY or EG so any error in these values could potentially explain the poor fit. It will be essential in further work to examine these values more closely.

Fitting the combination of ethylene glycol and glycerol proved impossible in my my model. The extremely high permeability values I determined in my experiment resulted in substantially less damage than expected. One possible explanation for this could be non-spherical shrinkage in the estimation of these permeability values or it could be some kind of “toxic” effect of the CPA mixture directly on the connections that is not being accounted for in my model. Younis et al. showed that EGTA altered the cytoplasmic extensions that are part of cumulus-oocyte connections [215]. In this study Younis et al. also showed that glycerol affects F-actin networks, which can disrupt or alter multiple different components of the tissue, including TZPs and the cytoskeleton, and can affect “more stable” and “less stable” F-actin networks differently. This could in part explain the unusual results for the combination of ethylene glycol and glycerol, if there is a physical change occurring to the tissue elasticity. It is also possible, but unlikely, that a mixture of ethylene glycol and glycerol together have a dramatic effect on the oocytes permeability as measured in Chapter 2.

Despite the above mentioned possible shortcomings in fitting spring constants, for equilibration with a single CPA or PBS, the values align well with qualitative observations from the experiment in Chapter 2, and my model is able to be fit to the experimental data. Qualitatively, it makes sense that long string-like TZPs are likely to be “weaker/less stiff” connections than the shorter gap junctions between granulosa cells or the firm connections between granulosa cells and the basement membrane. In fact, Irving-Rodgers et al.

[93] showed that in some follicles the basement membrane envelops the outermost layer of granulosa cells, which would surely result in a very strong/stiff connection. Additionally, while the whole follicle does shrink due to osmotic and spring forces, in simulations that shrinkage is within the statistically non-significant range of whole follicle volume changes seen in Chapter 2. Furthermore, the spring forces do not result in any significant gaps between granulosa cell layers, something that has not been observed in the experimental data or previous literature.

Since computational resources have thus far been limited to desktop computing, it may be possible that there exists a set of spring constants that appropriately fit all of the data for permeating, non-permeating and multisolute treatments, and this region of parameter space is located in an unsearched region; however, this seems very unlikely in the case of treatment with both ethylene glycol and glycerol, whose TZP score was extremely high given the amount of volume change induced by such a high concentration of solutes. My lab has secured access to an on campus high performance computing and plans to test this in the near future.

The most substantial drawback of this model was my the failure to closely fit CPA predicted TZP scores. As previously, mentioned when discussing the inability to fit this data. There are a number of possible causes for why my model could not capture a simulated TZP score that was close to the experimental TZP score. One possibility is that the breakage distance is incorrect and should also be included as a fitting parameter. Another possibility as mentioned above is that the permeability values for glycerol may be incorrect, and this seems a likely explanation. Unfortunately, it is extremely difficult to measure these values inside tissue which is likely why such parameters have not been measured before within follicles. This particular drawback can likely be resolved with further experimentation and only minor refinement of the model.

Another drawback was the inability to capture multisolute equilibrations expected TZP score. To date, no reports of multisolute transport parameters exist for any cell-type in the literature and this makes comparison for these values difficult as only theoretical values exist. While, the TZP score was higher than expected in experiment, the simulated TZP score suggested very little damage to TZPs would occur which is not what was observed.

One drawback in my model was the inability to capture morphological changes at the individual cell level, particularly non-spherical shrinkage of the oocyte; cell-level morphological changes may be responsible for

some of the damage that intercellular connections experience not just in oocytes but in other tissues. As shown in Chapter 2, I observed and measured non-spherical shrinkage of the oocyte. Granulosa cells may also experience deformation or non-spherical shrinkage, there is some preliminary observational evidence of this in the confocal imagery taken for the experiments in Chapter 2 but it is not conclusive. To address this, currently, the developers of PhysiCell have been beta testing different cell morphologies.

A possible issue with the model presented in this thesis is that there are several estimated parameters that have not been directly measured experimentally. The breakage distance, cell overlap distance and cell packing are all first order approximations and have not been directly measured. Similar to changes in morphology, it's unclear exactly how much of the tissue elasticity is the result of elasticity in the cellular membrane, cellular structure or the intercellular connections themselves. While these parameters are only first order approximations, they may be sufficient for the purpose of improving preantral equilibration protocols. The estimation of compressibility of granulosa cells, and thus overlap distance, likely has a small effect on TZP score given that TZP damage seems to occur when strain is applied to connections that are stretching as opposed to compressing. The cell overlap distance and the closely related cell packing will effect the size of a cell's neighbourhood slightly but given that this packing regime is similar to ones used previously, this too is likely a small effect. Alternatively the breakage distance could have a very significant effect on the TZP score, but since this term is used both to establish the connections as well as determine where they break it is difficult to analyze.

Another potential drawback that could be corrected in my model is the inability to capture the large variability between individual follicles. Given how much follicles vary in the size, and distribution of cells, it is likely that using a "mean" follicle is not the most accurate approach possible. A stochastically varied set of cell sizes, connection lengths and spring constants could possibly capture this variability. However, a stochastic agent based model would significantly increase the complexity of the model and require knowledge of the statistical distribution of physical cell parameters. Unfortunately, to my knowledge, much of the data for this is not currently available in the literature, particularly for primate preantral ovarian follicles. However, this level of accuracy may not be required, if future equilibration protocols designed with my current model produce improved CPA equilibration survival rates, it would demonstrate that this model is sufficient

for its intended purpose.

Despite these drawbacks I have provided evidence in favour of my initial hypothesis that I could capture the damage to intercellular connections by agent-based model, particularly for non-permeating solutes. Future work could be directed to using models, such as the model presented in this thesis, to simulate and compare new cryopreservation protocols. Furthermore, the results of both experimental and simulated equilibration in the multisolute cocktail of ethylene glycol and glycerol suggest that further experimentation should be done on multisolute solutions as they may provide either a protective effect to TZPs, either by altering elasticity, by increase the permeability of the oocyte to CPAs, or some other unknown mechanism. Finally, the model presented here can be further developed to include heat transfer for changing temperatures, morphological changes, stochasticity of cell sizes and connection strengths, as well as more detailed mass transport features such as tortuosity/diffusion channels and changing rates of diffusivity; these improvements would allow for the simulation of larger tissues with higher accuracy and the ultimate goal of simulating an entire cryopreservation protocol from start to finish. This model in its current state may also be applied to a number of other cryobiologically relevant tissues such as islets of Langerhans, ovarian slices and early-stage embryos.

### **3.13 Conclusion**

Overall I have shown that agent-based modeling is a promising method for modeling preantral ovarian follicles. My current model has the potential to optimize CPA equilibration for toxicity, osmotic tolerance limits and TZP score. A variety of improved equilibration protocols can be rapidly tested and then experimentally verified. With each experimental verification, the model can be further refined making the new iteration better than the previous. This virtuous cycle is one of the reasons that modern computational modeling holds so much promise for improving cryopreservation.

More generally, results presented in this chapter also show that agent-based modeling can be used to produce cryobiologically relevant tissue simulations. This model has the ability to be modified to capture damage in ovarian cortical tissue slices as well as other tissues types. Additionally, if one added stochasticity to my model predictions based on the variability in experimental data via statistically relevant individual

variation could be made. Furthermore, agent-based models can be combined with continuum models to produce hybrid models [43, 52] where the speed of continuum models can be combined with the tissue and cell level accuracy of an agent-based model.

## 4 GENERAL DISCUSSION

In this thesis I present an experiment informed agent-based model of a secondary stage ovarian follicle. The model simulates the changing size and intercellular forces experienced during the osmotic event caused by CPA equilibration. This model can be used to generate further hypotheses to improve the CPA equilibration of this tissue by minimizing damage to transzonal projections, maintain osmotic tolerance limits and minimize toxicity. Additionally, this model serves as a proof-of-concept for increasingly sophisticated agent-based tissue models to be used in the rational design of cryopreservation protocols.

In chapter one, I presented a brief overview of cryopreservation and vitrification in terms of theory and practice; additionally, I relayed the basics of agent-based modelling and ovarian follicle anatomy. Agent-based models in cryobiology can significantly improve and help inform new cryopreservation protocols, not just of this vital reproductive tissue but for tissues in general. Agent-based modeling offers a scalable way to adapt previously determined cell parameters to increasingly larger tissue models; these parameters are reasonably available in the literature and are easier to experimentally measure than cells in situ. The cryopreservation of tissues has tremendous implications for a wide range of fields and is increasingly the focus of research in cryobiology.

In chapter two, I described the experiment used to inform this model and its analysis. This experiment suggests that, at least in part, damage to critical transzonal projections (TZPs) arises from the differences in mass transport between heterogeneous cells. This damage may be exacerbated by the comparatively tight bonds between a secondary stage follicles basement membrane and the interior granulosa cells as well as tight granulosa-to-granulosa bonds. This damage does not appear to be the result of the often observed non-isotropic shrinkage of oocytes; but this effect can likely result in noise in tissue volumetric data. I have also described an experimental procedure that can be used to quantify damage to TZPs from CPA equilibration experiments.

While obtaining volumetric data from this experiment proved difficult it did result in data that suggest that mechanical damage of TZPs occurs specifically during the initial shrinking of CPA equilibration. This shrinkage is known to be the result of rapid water movement out of the cell [136]. Future experiments could be done to quantify whether the rate of this shrinkage alters TZP damage. Further experiments could also be done to expand this data set and explore the counterintuitive results presented the a so-called CPA cocktail of EG and glycerol. Additionally, further experiments could be done to validate the accuracy of or model and use it to optimize a CPA equilibration protocol.

The experimental results show that it is likely that denuded oocytes have the same volume response as those in tissue, which suggests that previous experimental data, may be used to inform agent-based models. As mentioned in Chapter 1, one of the great potential promises of agent-based modeling may be its ability to use experimental data from single cell or cell suspension experiments that already exist in the literature and apply them to tissue models.

In the third chapter I describe the mathematical model and how PhysiCell software [72] can be adapted to model CPA equilibration, and in particular tissues with large size differences between cell-types. The ability to modify this open-source software allows for the development of tools that can be applied to many different tissue types and different aspects of the cryopreservation process. In my model I first show that we can recreate the mass transport data for immature non-human primate oocytes reported in the literature by Karlsson et al. [108]. Then I demonstrate how a combination of experimental data, previous literature data and astute estimates can inform a novel tissue model. This model is then fit for parameters that can be used to estimate the aforementioned TZP damage. Additionally, I explore the sensitivity and convergence of the model revealing some of its limitations. Lastly, I make predictions for an optimized CPA equilibration that minimizes TZP damage.

As this model is used to develop future hypotheses, more data will in turn be collected to refine the model. This virtuous cycle of refining computational models followed by ever better experimental hypothesis testing allows for marked improvements in the design of cryopreservation protocols in general. Future versions of this model can be expanded to run with a stochastically generated sets of cells and intercellular connections to see if such a model can capture some of the large individual variation typically associated with this

tissue type and the corresponding variation in TZP scores. The model can also be expanded to handle changing temperature conditions and possibly morphological changes. The model could be validated with the measurement intercellular forces using techniques such as atomic force microscopy [42, 126, 142]. It is also limited by the lack of any granulosa cell permeability parameters in the literature, although careful experimentation with Coulter counters may amend this in the future.

I hope this thesis and the work it contains serves as a starting point for an increased use of agent-based modeling in cryopreservation and cryobiology in general. This type of model is an invaluable tool for studying and understanding complex systems, generating new hypothesis and experiments, and improving the clinical preservation of tissues.

## REFERENCES

- [1] Abazari, A., Elliott, J. A. W., Law, G. K., McGann, L. E., and Jomha, N. M. (2009). A biomechanical triphasic approach to the transport of nondilute solutions in articular cartilage. *Biophys. J.*, 97(12):3054–3064.
- [2] Abazari, A., Jomha, N. M., Elliott, J. A. W., and McGann, L. E. (2013). Cryopreservation of articular cartilage. *Cryobiology*, 66(3):201–209.
- [3] Acker, J. P., Larese, A., Yang, H., Petrenko, A., and McGann, L. E. (1999). Intracellular ice formation is affected by cell interactions. *Cryobiology*, 38(4):363–371.
- [4] Agarwal, N. and Kwan, P. (2017). Pricing mergers & acquisitions using agent-based modeling. *Economics, Management and Financial Markets*, 12(1):55.
- [5] Amorim, C. A., Rondina, D., Lucci, C. M., Gonçalves, P. B. D., de Figueiredo, J. R., and Giorgetti, A. (2006). Permeability of ovine primordial follicles to different cryoprotectants. *Fertil. Steril.*
- [6] An, G., Mi, Q., Dutta-Moscato, J., and Vodovotz, Y. (2009). Agent-based models in translational systems biology. *Wiley Interdiscip. Rev. Syst. Biol. Med.*, 1(2):159–171.
- [7] Anderson, D. M., Benson, J. D., and Kearsley, A. J. (2014). Foundations of modeling in cryobiology-I: concentration, gibbs energy, and chemical potential relationships. *Cryobiology*, 69(3):349–360.
- [8] Anderson, D. M., Benson, J. D., and Kearsley, A. J. (2019a). Foundations of modeling in cryobiology-II: Heat and mass transport in bulk and at cell membrane and ice-liquid interfaces. *Cryobiology*, 91:3–17.
- [9] Anderson, D. M., Benson, J. D., and Kearsley, A. J. (2019b). Numerical solution of inward solidification of a dilute ternary solution towards a semi-permeable spherical cell. *Math. Biosci.*, 316:108240.

- [10] Antczak, M. and Van Blerkom, J. (2000). The vascular character of ovarian follicular granulosa cells: phenotypic and functional evidence for an endothelial-like cell population. *Hum. Reprod.*, 15(11):2306–2318.
- [11] Anzar, M. (2017). Cryopreservation of mammalian oocytes. In *Animal Models and Human Reproduction*, pages 519–556. wiley.
- [12] Armitage, W. J., Juss, B. K., and Easty, D. L. (1995). Differing effects of various cryoprotectants on intercellular junctions of epithelial (MDCK) cells. *Cryobiology*, 32(1):52–59.
- [13] Baena, V. and Terasaki, M. (2019). Three-dimensional organization of transzonal projections and other cytoplasmic extensions in the mouse ovarian follicle. *Sci. Rep.*, 9(1).
- [14] Bahr, D. B. and Bekoff, M. (1999). Predicting flock vigilance from simple passerine interactions: modelling with cellular automata. *Anim. Behav.*, 58(4):831–839.
- [15] Bakhach, J. (2009). The cryopreservation of composite tissues: Principles and recent advancement on cryopreservation of different type of tissues. *Organogenesis*, 5(3):119–126.
- [16] Balaban, B., Ata, B., Isiklar, A., Yakin, K., and Urman, B. (2008). Severe cytoplasmic abnormalities of the oocyte decrease cryosurvival and subsequent embryonic development of cryopreserved embryos. *Hum. Reprod.*, 23(8):1778–1785.
- [17] Barrett, S. L., Shea, L. D., and Woodruff, T. K. (2010). Noninvasive index of cryorecovery and growth potential for human follicles in vitro. *Biol. Reprod.*, 82(6):1180–1189.
- [18] Bashforth, F. and Adams, J. C. (1883). *An attempt to test the theories of capillary action : by comparing the theoretical and measured forms of drops of fluid. With an explanation of the method of integration employed in constructing the tables which give the theoretical forms of such drops.* Cambridge University Press, Cambridge [England].
- [19] Basini, G., Falasconi, I., Bussolati, S., Grolli, S., Di Lecce, R., and Grasselli, F. (2016). Swine granulosa cells show typical endothelial cell characteristics. *Reprod. Sci.*, 23(5):630–637.

- [20] Bays, C. (2010). Introduction to cellular automata and conway’s game of life. In Adamatzky, A., editor, *Game of Life Cellular Automata*, pages 1–7. Springer London, London.
- [21] Ben Youssef, B. (2016). Chapter 19 - cellular Automata-Based modeling of Three-Dimensional multi-cellular tissue growth. In Tran, Q. N. and Arabnia, H. R., editors, *Emerging Trends in Applications and Infrastructures for Computational Biology, Bioinformatics, and Systems Biology*, pages 287–303. Morgan Kaufmann, Boston.
- [22] Benson, C. T. and Critser, J. K. (1994). Variation of water permeability (lp) and its activation energy (ea) among unfertilized golden hamster and ICR murine oocytes. *Cryobiology*, 31(3):215–223.
- [23] Benson, J. and Macklin, P. (2015). 43. cell-based modeling of mechanical and chemical stress in tissues during cryoprotocols. *Cryobiology*, 71(1):176.
- [24] Benson, J. D. (2012). Some comments on recent discussion of the boyle van’t hoff relationship. *Cryobiology*.
- [25] Benson, J. D. (2015). Modeling and optimization of cryopreservation. In Wolkers, W. F. and Oldenhof, H., editors, *Cryopreservation and Freeze-Drying Protocols*, pages 83–120. Springer New York, New York, NY.
- [26] Benson, J. D. (2021). Mathematical modeling and optimization of cryopreservation in single cells. In Wolkers, W. F. and Oldenhof, H., editors, *Cryopreservation and Freeze-Drying Protocols*, pages 129–172. Springer US, New York, NY.
- [27] Benson, J. D., Benson, C. T., and Critser, J. K. (2014). Mathematical model formulation and validation of water and solute transport in whole hamster pancreatic islets. *Math. Biosci.*, 254:64–75.
- [28] Benson, J. D., Chicone, C. C., and Critser, J. K. (2005). Exact solutions of a two parameter flux model and cryobiological applications. *Cryobiology*.
- [29] Benson, J. D., Higgins, A. Z., Desai, K., and Eroglu, A. (2018). A toxicity cost function approach to optimal CPA equilibration in tissues. *Cryobiology*.

- [30] Benson, J. D., Kearsley, A. J., and Higgins, A. Z. (2012). Mathematical optimization of procedures for cryoprotectant equilibration using a toxicity cost function. *Cryobiology*, 64(3):144–151.
- [31] Bissoyi, A., Nayak, B., Pramanik, K., and Sarangi, S. K. (2014). Targeting cryopreservation-induced cell death: a review. *Biopreserv. Biobank.*, 12(1):23–34.
- [32] Blikstein, P. and Wilensky, U. (2009). An atom is known by the company it keeps: A constructionist learning environment for materials science using Agent-Based modeling. *Int. J. Comput. Math. Learn.*, 14(2):81–119.
- [33] Borges, E. N., Silva, R. C., Futino, D. O., Rocha-Junior, C. M. C., Amorim, C. A., Bao, S. N., and Lucci, C. M. (2009). Cryopreservation of swine ovarian tissue: Effect of different cryoprotectants on the structural preservation of preantral follicle oocytes. *Cryobiology*, 59(2):195–200.
- [34] Boutron, P. and Mehl, P. (1990). Theoretical prediction of devitrification tendency: determination of critical warming rates without using finite expansions. *Cryobiology*, 27(4):359–377.
- [35] Brambillasca, F., Guglielmo, M. C., Coticchio, G., Mignini Renzini, M., Dal Canto, M., and Fadini, R. (2013). The current challenges to efficient immature oocyte cryopreservation. *J. Assist. Reprod. Genet.*, 30(12):1531–1539.
- [36] Bus, A., Langbeen, A., Martin, B., Leroy, J. L. M. R., and Bols, P. E. J. (2019). Is the pre-antral ovarian follicle the ‘holy grail’ for female fertility preservation? *Anim. Reprod. Sci.*, 207:119–130.
- [37] Bus, A., Szymanska, K., Pintelon, I., Leroy, J. L. M. R., Leybaert, L., and Bols, P. E. J. (2021). Preservation of connexin 43 and transzonal projections in isolated bovine pre-antral follicles before and following vitrification. *J. Assist. Reprod. Genet.*, 38(2):479–492.
- [38] Caballero, L., Hodge, B., and Hernandez, S. (2016). Conway’s “game of life” and the epigenetic principle. *Front. Cell. Infect. Microbiol.*, 6:57.
- [39] Cakmak, H. and Rosen, M. P. (2013). Ovarian stimulation in cancer patients. *Fertil. Steril.*, 99(6):1476–1484.

- [40] Cecconi, S., Capacchietti, G., Russo, V., Berardinelli, P., Mattioli, M., and Barboni, B. (2004). In vitro growth of preantral follicles isolated from cryopreserved ovine ovarian tissue. *Biol. Reprod.*, 70(1):12–17.
- [41] Cha, S. K., Kim, B. Y., Kim, M. K., Kim, Y. S., Lee, W. S., Yoon, T. K., and Lee, D. R. (2011). Effects of various combinations of cryoprotectants and cooling speed on the survival and further development of mouse oocytes after vitrification. *Clin. Exp. Reprod. Med.*, 38(1):24–30.
- [42] Choi, J. K., Yue, T., Huang, H., Zhao, G., Zhang, M., and He, X. (2015). The crucial role of zona pellucida in cryopreservation of oocytes by vitrification. *Cryobiology*, 71(2):350–355.
- [43] Cilfone, N. A., Kirschner, D. E., and Linderman, J. J. (2015). Strategies for efficient numerical implementation of hybrid multi-scale agent-based models to describe biological systems. *Cell. Mol. Bioeng.*, 8(1):119.
- [44] Clarke, K. C. (2014). Cellular automata and Agent-Based models. In Fischer, M. M. and Nijkamp, P., editors, *Handbook of Regional Science*, pages 1217–1233. Springer Berlin Heidelberg, Berlin, Heidelberg.
- [45] Cohen, Y., St-Onge-St-Hilaire, A., Tannus, S., Younes, G., Dahan, M. H., Buckett, W., and Son, W.-Y. (2018). Decreased pregnancy and live birth rates after vitrification of in vitro matured oocytes. *J. Assist. Reprod. Genet.*, 35(9):1683–1689.
- [46] Conway, J. H. and Sloane, N. J. A. (1999). *Sphere Packings, Lattices and Groups*. Springer, New York, NY.
- [47] Craig, J., Orisaka, M., Wang, H., Orisaka, S., Thompson, W., Zhu, C., Kotsuji, F., and Tsang, B. K. (2007). Gonadotropin and intra-ovarian signals regulating follicle development and atresia: the delicate balance between life and death. *Front. Biosci.*, 12:3628–3639.
- [48] Cui, Z. F., Dykhuizen, R. C., Nerem, R. M., and Sembanis, A. (2002). Modeling of cryopreservation of engineered tissues with one-dimensional geometry. *Biotechnol. Prog.*, 18(2):354–361.
- [49] Dalmaso, G., Marin Zapata, P. A., Brady, N. R., and Hamacher-Brady, A. (2017). Agent-Based modeling of mitochondria links Sub-Cellular dynamics to cellular homeostasis and heterogeneity. *PLoS One*, 12(1):e0168198.

- [50] Davidson, A. F., Benson, J. D., and Higgins, A. Z. (2014). Mathematically optimized cryoprotectant equilibration procedures for cryopreservation of human oocytes. *Theor. Biol. Med. Model.*
- [51] Davidson, A. F., Glasscock, C., McClanahan, D. R., Benson, J. D., and Higgins, A. Z. (2015). Toxicity minimized cryoprotectant addition and removal procedures for adherent endothelial cells. *PLoS One*, 10(11):1–22.
- [52] de Montigny, J., Iosif, A., Breitwieser, L., Manca, M., Bauer, R., and Vavourakis, V. (2021). An in silico hybrid continuum-/agent-based procedure to modelling cancer development: Interrogating the interplay amongst glioma invasion, vascularity and necrosis. *Methods*, 185:94–104.
- [53] Delvigne, A. and Rozenberg, S. (2003). Review of clinical course and treatment of ovarian hyperstimulation syndrome (OHSS). *Hum. Reprod. Update*, 9(1):77–96.
- [54] Devireddy, R. V., Amorim, C. A., and Leibo, S. P. (2006). Permeability characteristics of ovine primordial follicles calculated with two parameter Kedem-Katchalsky formulation. *Cell Preserv. Technol.*, 4(3):188–198.
- [55] Diller, K. R. and Raymond, J. F. (1990). Water transport through a multicellular tissue during freezing—a network thermodynamic modeling analysis. *Cryo-Letters*, 11(2):151–162.
- [56] Dinikina, Y., Belogurova, M., Zaritskey, A., Govorov, I., Tsibizova, V., Gamzatova, Z., Pervunina, T., and Komlichenko, E. (2019). Ovarian tissue cryopreservation in prepubertal patients with oncological diseases: multidisciplinary approach and outcomes. *J. Matern. Fetal. Neonatal Med.*, pages 1–8.
- [57] Dolmans, M.-M. and Amorim, C. A. (2019). FERTILITY PRESERVATION: Construction and use of artificial ovaries. *Reproduction*, 158(5):F15–F25.
- [58] Durant, M. R. (1990). Cryopreservation of human embryos: A scientific advance, a judicial dilemma. *Suffolk UL Rev.*, 24:707.
- [59] Edashige, K. (2017). Permeability of the plasma membrane to water and cryoprotectants in mammalian oocytes and embryos: Its relevance to vitrification. *Reprod. Med. Biol.*, 16(1):36–39.

- [60] El-Hayek, S., Yang, Q., Abbassi, L., FitzHarris, G., and Clarke, H. J. (2018). Mammalian oocytes locally remodel follicular architecture to provide the foundation for Germline-Soma communication. *Curr. Biol.*, 28(7):1124–1131.e3.
- [61] Elliott, G. D., Wang, S., and Fuller, B. J. (2017). Cryoprotectants: A review of the actions and applications of cryoprotective solutes that modulate cell recovery from ultra-low temperatures. *Cryobiology*, 76:74–91.
- [62] Fahy, G. M., Lilley, T. H., Linsdell, H., Douglas, M. S., and Meryman, H. T. (1990). Cryoprotectant toxicity and cryoprotectant toxicity reduction: in search of molecular mechanisms. *Cryobiology*, 27(3):247–268.
- [63] Fahy, G. M. and Wowk, B. (2015). Principles of cryopreservation by vitrification. *Methods Mol. Biol.*, 1257:21–82.
- [64] Fasouliotis, S. J. and Schenker, J. G. (1996). Cryopreservation of embryos: medical, ethical, and legal issues. *J. Assist. Reprod. Genet.*, 13(10):756–761.
- [65] Fidelman, M. L. and Mikulecky, D. C. (1988). Network thermodynamic analysis and simulation of isotonic solute-coupled volume flow in leaky epithelia: An example of the use of network theory to provide the qualitative aspects of a complex system and its verification by simulation. *J. Theor. Biol.*, 130(1):73–93.
- [66] Fletcher, A. G., Osterfield, M., Baker, R. E., and Shvartsman, S. Y. (2014). Vertex models of epithelial morphogenesis. *Biophys. J.*, 106(11):2291–2304.
- [67] Friedler, S., Giudice, L. C., and Lamb, E. J. (1988). Cryopreservation of embryos and ova. *Fertil. Steril.*, 49(5):743–764.
- [68] Fry, A. K. and Higgins, A. Z. (2012). Measurement of cryoprotectant permeability in adherent endothelial cells and applications to cryopreservation. *Cell. Mol. Bioeng.*, 5(3):287–298.
- [69] Fuller, B. and Paynter, S. (2004). Fundamentals of cryobiology in reproductive medicine. *Reprod. Biomed. Online*, 9(6):680–691.

- [70] Fuller, B. J., Lane, N., and Benson, E. E., editors (2004). *Life in the Frozen State*. CRC Press, 0 edition.
- [71] Ghaffarizadeh, A., Friedman, S. H., and MacKlin, P. (2016). BioFVM: An efficient, parallelized diffusive transport solver for 3-D biological simulations. *Bioinformatics*, 32(8):1256–1258.
- [72] Ghaffarizadeh, A., Heiland, R., Friedman, S. H., Mumenthaler, S. M., and Macklin, P. (2018). Physi-Cell: An open source physics-based cell simulator for 3-D multicellular systems. *PLoS Comput. Biol.*, 14(2):e1005991.
- [73] Ghetler, Y., Yavin, S., Shalgi, R., and Arav, A. (2005). The effect of chilling on membrane lipid phase transition in human oocytes and zygotes. *Hum. Reprod.*, 20(12):3385–3389.
- [74] Gilbert, N. and Bankes, S. (2002). Platforms and methods for agent-based modeling. *Proc. Natl. Acad. Sci. U. S. A.*, 99 Suppl 3:7197–7198.
- [75] Giwa, S., Lewis, J. K., Alvarez, L., Langer, R., Roth, A. E., Church, G. M., Markmann, J. F., Sachs, D. H., Chandraker, A., Wertheim, J. A., Rothblatt, M., Boyden, E. S., Eidbo, E., Lee, W. P. A., Pomahac, B., Brandacher, G., Weinstock, D. M., Elliott, G., Nelson, D., Acker, J. P., Uygun, K., Schmalz, B., Weegman, B. P., Tocchio, A., Fahy, G. M., Storey, K. B., Rubinsky, B., Bischof, J., Elliott, J. A. W., Woodruff, T. K., Morris, G. J., Demirci, U., Brockbank, K. G. M., Woods, E. J., Ben, R. N., Baust, J. G., Gao, D., Fuller, B., Rabin, Y., Kravitz, D. C., Taylor, M. J., and Toner, M. (2017). The promise of organ and tissue preservation to transform medicine. *Nat. Biotechnol.*, 35(6):530–542.
- [76] Glass, G. V., Peckham, P. D., and Sanders, J. R. (1972). Consequences of failure to meet assumptions underlying the fixed effects analyses of variance and covariance. *Rev. Educ. Res.*, 42(3):237–288.
- [77] Glen, C. M., Kemp, M. L., and Voit, E. O. (2019). Agent-based modeling of morphogenetic systems: Advantages and challenges. *PLoS Comput. Biol.*, 15(3):e1006577.
- [78] Griffié, J., Peters, R., and Owen, D. M. (2020). An agent-based model of molecular aggregation at the cell membrane. *PLoS One*, 15(2):e0226825.
- [79] Grow, A. and Van Bavel, J., editors (2017). *Agent-Based Modelling in Population Studies: Concepts, Methods, and Applications*. Springer, Cham.

- [80] Harada, M. and Osuga, Y. (2019). Fertility preservation for female cancer patients. *Int. J. Clin. Oncol.*, 24(1):28–33.
- [81] Hasegawa, A., Mochida, N., Ogasawara, T., and Koyama, K. (2006). Pup birth from mouse oocytes in preantral follicles derived from vitrified and warmed ovaries followed by in vitro growth, in vitro maturation, and in vitro fertilization. *Fertil. Steril.*, 86(4 Suppl):1182–1192.
- [82] Hatırnaz, Ş., Ata, B., Hatırnaz, E. S., Dahan, M. H., Tannus, S., Tan, J., and Tan, S. L. (2018). Oocyte in vitro maturation: A systematic review. *Turk J Obstet Gynecol*, 15(2):112–125.
- [83] Heath, B., Hill, R., and Ciarallo, F. (2009). A survey of agent-based modeling practices (january 1998 to july 2008). *Journal of Artificial Societies and Social Simulation*, 12(4):9.
- [84] Herraiz, S., Novella-Maestre, E., Rodríguez, B., Díaz, C., Sánchez-Serrano, M., Mirabet, V., and Pellicer, A. (2014). Improving ovarian tissue cryopreservation for oncologic patients: slow freezing versus vitrification, effect of different procedures and devices. *Fertil. Steril.*, 101(3):775–784.
- [85] Higgins, A. Z., Eroglu, A., and Benson, J. D. (2018). Extension of cellular toxicity cost functions to tissues. *Cryobiology*, 80:160.
- [86] Higgins, A. Z. and Karlsson, J. O. M. (2012). Comparison of cell membrane water permeability in monolayers and suspensions. *Cryo Letters*, 33(2):96–107.
- [87] Ho, J. R., Woo, I., Louie, K., Salem, W., Jabara, S. I., Bendikson, K. A., Paulson, R. J., and Chung, K. (2017). A comparison of live birth rates and perinatal outcomes between cryopreserved oocytes and cryopreserved embryos. *J. Assist. Reprod. Genet.*, 34(10):1359–1366.
- [88] Ho, V. N. A., Pham, T. D., Le, A. H., Ho, T. M., and Vuong, L. N. (2018). Live birth rate after human chorionic gonadotropin priming in vitro maturation in women with polycystic ovary syndrome. *J. Ovarian Res.*, 11(1):70.
- [89] Hooke, R. (1678). *Lectures de potentia restitutiva or of spring explaining the power of springing bodies*. London.

- [90] Hoshino, Y. (2018). Updating the markers for oocyte quality evaluation: intracellular temperature as a new index. *Reprod. Med. Biol.*, 17(4):434–441.
- [91] Hunter, J. E., Bernard, A., Fuller, B. J., McGrath, J. J., and Shaw, R. W. (1992). Measurements of the membrane water permeability (lp) and its temperature dependence (activation energy) in human fresh and failed-to-fertilize oocytes and mouse oocyte. *Cryobiology*, 29(2):240–249.
- [92] Hussein, R. S., Khan, Z., and Zhao, Y. (2020). Fertility preservation in women: Indications and options for therapy. *Mayo Clin. Proc.*, 95(4):770–783.
- [93] Irving-Rodgers, H. F., Morris, S., Collett, R. A., Peura, T. T., Davy, M., Thompson, J. G., Mason, H. D., and Rodgers, R. J. (2009). Phenotypes of the ovarian follicular basal lamina predict developmental competence of oocytes. *Hum. Reprod.*, 24(4):936–944.
- [94] Irving-Rodgers, H. F. and Rodgers, R. J. (2000). Ultrastructure of the basal lamina of bovine ovarian follicles and its relationship to the membrana granulosa. *J. Reprod. Fertil.*, 118(2):221–228.
- [95] Iserles, A. (1996). *A first course in the numerical analysis of differential equations*. Cambridge University Press, USA.
- [96] Ishihara, S., Marcq, P., and Sugimura, K. (2017). From cells to tissue: A continuum model of epithelial mechanics. *Phys Rev E*, 96(2-1):022418.
- [97] Iwasaki, W. M. and Innan, H. (2017). Simulation framework for generating intratumor heterogeneity patterns in a cancer cell population.
- [98] Jamnongjit, M. and Hammes, S. R. (2005). Oocyte maturation: the coming of age of a germ cell. *Semin. Reprod. Med.*, 23(3):234–241.
- [99] Jee, B. C., Chen, H. Y., Chian, R.-C., Suh, C. S., Kim, S. H., and Moon, S. Y. (2009). Vitrification of immature mouse oocyte using stepwise equilibration before or after in vitro maturation. *Fertil. Steril.*, 92(3):1153–1157.
- [100] Jenkins, E. C., Ye, L., and Silverman, W. P. (2012). Does the cryogenic freezing process cause shorter telomeres? *Cryobiology*, 65(1):72–73.

- [101] Jennings, J., Bauer, R., and Breitwieser, L. (2019). Computational modelling of slow freezing using the biodynamo software package cryodynamo. *Cryobiology*, 91:191–192.
- [102] Jin, B., Kleinhans, F. W., and Mazur, P. (2014). Survivals of mouse oocytes approach 100% after vitrification in 3-fold diluted media and ultra-rapid warming by an IR laser pulse. *Cryobiology*, 68(3):419–430.
- [103] Kang, G., Márquez, C., Barat, A., Byrne, A. T., Prehn, J. H. M., Sorribes, J., and César, E. (2017). Colorectal tumour simulation using agent based modelling and high performance computing. *Future Gener. Comput. Syst.*, 67:397–408.
- [104] Karlsson, J. O. (2001). A theoretical model of intracellular devitrification. *Cryobiology*, 42(3):154–169.
- [105] Karlsson, J. O., Eroglu, A., Toth, T. L., Cravalho, E. G., and Toner, M. (1996). Fertilization and development of mouse oocytes cryopreserved using a theoretically optimized protocol. *Hum. Reprod.*, 11(6):1296–1305.
- [106] Karlsson, J. O. M. (2010). Effects of solution composition on the theoretical prediction of ice nucleation kinetics and thermodynamics. *Cryobiology*, 60(1):43–51.
- [107] Karlsson, J. O. M., Szurek, E. A., Higgins, A. Z., Lee, S. R., and Eroglu, A. (2014). Optimization of cryoprotectant loading into murine and human oocytes. *Cryobiology*, 68(1):18–28.
- [108] Karlsson, J. O. M., Younis, A. I., Chan, A. W. S., Gould, K. G., and Eroglu, A. (2009). Permeability of the rhesus monkey oocyte membrane to water and common cryoprotectants. *Mol. Reprod. Dev.*, 76(4):321–333.
- [109] Kashuba, C. M., Benson, J. D., and Critser, J. K. (2014). Rationally optimized cryopreservation of multiple mouse embryonic stem cell lines: I—Comparative fundamental cryobiology of multiple mouse embryonic stem cell lines and the implications for embryonic stem cell cryopreservation protocols. *Cryobiology*, 68(2):166–175.
- [110] Katkov, I. I. (2000). A two-parameter model of cell membrane permeability for multisolute systems. *Cryobiology*, 40(1):64–83.

- [111] Kawai, T. and Shimada, M. (2020). Pretreatment of ovaries with collagenase before vitrification keeps the ovarian reserve by maintaining cell-cell adhesion integrity in ovarian follicles. *Sci. Rep.*, 10(1):6841.
- [112] Kedem, O. and Katchalsky, A. (1961). A physical interpretation of the phenomenological coefficients of membrane permeability. *J. Gen. Physiol.*, 45:143–179.
- [113] Khalili, M. A., Shahedi, A., Ashourzadeh, S., Nottola, S. A., Macchiarelli, G., and Palmerini, M. G. (2017). Vitrification of human immature oocytes before and after in vitro maturation: a review. *J. Assist. Reprod. Genet.*, 34(11):1413–1426.
- [114] Kim, H., Kim, H., and Ku, S.-Y. (2018). Fertility preservation in pediatric and young adult female cancer patients. *Ann Pediatr Endocrinol Metab*, 23(2):70–74.
- [115] Kim, T. J., Laufer, L. R., and Hong, S. W. (2010). Vitrification of oocytes produces high pregnancy rates when carried out in fertile women. *Fertil. Steril.*, 93(2):467–474.
- [116] Kleinhans, F. W. (1998). Membrane permeability modeling: Kedem-Katchalsky vs a two-parameter formalism. *Cryobiology*, 37(4):271–289.
- [117] Kleinhans, F. W. and Mazur, P. (2009). Determination of the water permeability (lp) of mouse oocytes at -25 degrees C and its activation energy at subzero temperatures. *Cryobiology*, 58(2):215–224.
- [118] Koch, J. and Ledger, W. (2013). Ovarian stimulation protocols for onco-fertility patients. *J. Assist. Reprod. Genet.*, 30(2):203–206.
- [119] Kuwayama, M., Fujikawa, S., and Nagai, T. (1994). Ultrastructure of IVM-IVF bovine blastocysts vitrified after equilibration in glycerol 1,2-propanediol using 2-step and 16-step procedures. *Cryobiology*, 31(5):415–422.
- [120] Lawson, A., Ahmad, H., and Sambanis, A. (2011). Cytotoxicity effects of cryoprotectants as single-component and cocktail vitrification solutions. *Cryobiology*, 62(2):115–122.
- [121] Lawson, A., Mukherjee, I. N., and Sambanis, A. (2012). Mathematical modeling of cryoprotectant addition and removal for the cryopreservation of engineered or natural tissues. *Cryobiology*, 64(1):1–11.

- [122] Lee Jennings, J. and Bauer, R. (2020). Cryodynamo: A computational platform for cryopreservation optimisation. *Cryobiology*, 97:295.
- [123] Len, J. S., Koh, W. S. D., and Tan, S.-X. (2019). The roles of reactive oxygen species and antioxidants in cryopreservation. *Biosci. Rep.*, 39(8).
- [124] Letort, G., Montagud, A., Stoll, G., Heiland, R., Barillot, E., MacKlin, P., Zinovyev, A., and Calzone, L. (2019). PhysiBoSS: A multi-scale agent-based modelling framework integrating physical dimension and cell signalling. *Bioinformatics*, 35(7).
- [125] Levin, R. L., Cravalho, E. G., and Huggins, C. E. (1977). Water transport in a cluster of closely packed erythrocytes at subzero temperatures. *Cryobiology*, 14(5):549–558.
- [126] Li, M., Zhang, C., Wang, L., Liu, L., Xi, N., Wang, Y., and Dong, Z. (2013). Investigating the morphology and mechanical properties of blastomeres with atomic force microscopy: Cell morphology and mechanics. *Surf. Interface Anal.*, 45(8):1193–1196.
- [127] Lin, C. and Tsai, S. (2012). The effect of cryopreservation on DNA damage, gene expression and protein abundance in vertebrate. *Ital. J. Anim. Sci.*, 11(1):e21.
- [128] Liu, D., Yan, J., and Qiao, J. (2020). Effects of malignancies on fertility preservation outcomes and relevant cryobiological advances. *Sci. China Life Sci.*, 63(2):217–227.
- [129] Lotz, L., Dittrich, R., Hoffmann, I., and Beckmann, M. W. (2019). Ovarian tissue transplantation: Experience from germany and worldwide efficacy. *Clin Med Insights Reprod Health*, 13:1179558119867357.
- [130] Luciano, A. M., Chigioni, S., Lodde, V., Franciosi, F., Luvoni, G. C., and Modina, S. C. (2009). Effect of different cryopreservation protocols on cytoskeleton and gap junction mediated communication integrity in feline germinal vesicle stage oocytes. *Cryobiology*, 59(1):90–95.
- [131] Macal, C. M. and North, M. J. (2005). Tutorial on agent-based modeling and simulation. In *Proceedings of the Winter Simulation Conference, 2005.*, pages 14 pp.–. [ieeexplore.ieee.org](http://ieeexplore.ieee.org).
- [132] Maroudas, A. (1970). Distribution and diffusion of solutes in articular cartilage. *Biophys. J.*, 10(5):365–379.

- [133] Marques, C. C., Santos-Silva, C., Rodrigues, C., Matos, J. E., Moura, T., Baptista, M. C., Horta, A. E. M., Bessa, R. J. B., Alves, S. P., Soveral, G., and Pereira, R. M. L. N. (2018). Bovine oocyte membrane permeability and cryosurvival: Effects of different cryoprotectants and calcium in the vitrification media. *Cryobiology*, 81:4–11.
- [134] Martins, J. L. A., Lopes, M. D., de Souza, F. F., Possebon, F. S., Wibbelt, G., and Jewgenow, K. (2018). Cat preantral follicle survival after prolonged cooled storage followed by vitrification. *Cryobiology*, 81:94–100.
- [135] Mazur, P. (1963). Studies on rapidly frozen suspensions of yeast cells by differential thermal analysis and conductometry. *Biophys. J.*, 3:323–353.
- [136] Mazur, P. (1984). Freezing of living cells: mechanisms and implications. *Am. J. Physiol.*, 247(3 Pt 1):C125–42.
- [137] Mazur, P., Leibo, S. P., and Chu, E. H. (1972). A two-factor hypothesis of freezing injury. evidence from chinese hamster tissue-culture cells. *Exp. Cell Res.*, 71(2):345–355.
- [138] Mazur, P. and Paredes, E. (2016). Roles of intracellular ice formation, vitrification of cell water, and recrystallisation of intracellular ice on the survival of mouse embryos and oocytes. *Reprod. Fertil. Dev.*
- [139] Mazur, P. and Schneider, U. (1986). Osmotic responses of preimplantation mouse and bovine embryos and their cryobiological implications. *Cell Biophys.*, 8(4):259–285.
- [140] Metzcar, J., Wang, Y., Heiland, R., and Macklin, P. (2019). A review of Cell-Based computational modeling in cancer biology. *JCO Clin Cancer Inform.*, 3:1–13.
- [141] Michelmann, H. W. and Nayudu, P. (2006). Cryopreservation of human embryos. *Cell Tissue Bank.*, 7(2):135–141.
- [142] Mieda, S., Amemiya, Y., Kihara, T., Okada, T., Sato, T., Fukazawa, K., Ishihara, K., Nakamura, N., Miyake, J., and Nakamura, C. (2012). Mechanical force-based probing of intracellular proteins from living cells using antibody-immobilized nanoneedles. *Biosens. Bioelectron.*, 31(1):323–329.

- [143] Moawad, M., Hussein, H. A., Abd El-Ghani, M., Darwish, G., and Badr, M. (2019). Effects of cryoprotectants and cryoprotectant combinations on viability and maturation rates of camelus dromedarius oocytes vitrified at germinal vesicle stage. *Reprod. Domest. Anim.*, 54(1):108–117.
- [144] Morris, G. J. and Acton, E. (2013). Controlled ice nucleation in cryopreservation—a review. *Cryobiology*, 66(2):85–92.
- [145] Mouttham, L. and Comizzoli, P. (2016). The preservation of vital functions in cat ovarian tissues during vitrification depends more on the temperature of the cryoprotectant exposure than on the sucrose supplementation. *Cryobiology*, 73(2):187–195.
- [146] Mullen, S. F., Li, M., Li, Y., Chen, Z.-J., and Critser, J. K. (2008). Human oocyte vitrification: the permeability of metaphase II oocytes to water and ethylene glycol and the appliance toward vitrification. *Fertil. Steril.*, 89(6):1812–1825.
- [147] Navarro-Costa, P., Correia, S. C., Gouveia-Oliveira, A., Negreiro, F., Jorge, S., Cidadão, A. J., Carvalho, M. J., and Plancha, C. E. (2005). Effects of mouse ovarian tissue cryopreservation on granulosa cell-oocyte interaction. *Hum. Reprod.*, 20(6):1607–1614.
- [148] Pacheco, F. and Oktay, K. (2017). Current success and efficiency of autologous ovarian transplantation: A Meta-Analysis. *Reprod. Sci.*, 24(8):1111–1120.
- [149] Page, E. and Bernstein, R. S. (1964). CAT HEART MUSCLE IN VITRO. v. DIFFUSION THROUGH a SHEET OF RIGHT VENTRICLE. *J. Gen. Physiol.*, 47:1129–1140.
- [150] Parks, S. C., Garifullin, M., and Dronzek, R. (2005). Argus invasive species spread model constructed using agent-based modeling approach and cellular automata. In *Proceedings of the Winter Simulation Conference, 2005.*, pages 5 pp.–.
- [151] Pegg, D. E. (2007). Principles of cryopreservation. *Methods Mol. Biol.*, 368:39–57.
- [152] Pegg, D. E. (2015). Principles of cryopreservation. In Wolkers, W. F. and Oldenhof, H., editors, *Cryopreservation and Freeze-Drying Protocols*, pages 3–19. Springer New York, New York, NY.

- [153] Pegg, D. E., Wusteman, M. C., and Boylan, S. (1997). Fractures in cryopreserved elastic arteries. *Cryobiology*, 34(2):183–192.
- [154] Pérez-Rodríguez, G., Pérez-Pérez, M., Fdez-Riverola, F., and Lourenço, A. (2016). High performance computing for three-dimensional agent-based molecular models. *J. Mol. Graph. Model.*, 68:68–77.
- [155] Piras, A. R., Burrai, G. P., Ariu, F., Falchi, L., Zedda, M. T., Pau, S., Gadau, S. D., Antuofermo, E., Bebbere, D., Ledda, S., and Bogliolo, L. (2018). Structure of preantral follicles, oxidative status and developmental competence of in vitro matured oocytes after ovary storage at 4 °c in the domestic cat model. *Reprod. Biol. Endocrinol.*, 16(1):76.
- [156] Prickett, R. C., Elliott, J. A. W., Hakda, S., and McGann, L. E. (2008). A non-ideal replacement for the boyle van’t hoff equation. *Cryobiology*, 57(2):130–136.
- [157] Qiao, H., Ding, W., Sun, S., Gong, L., and Gao, D. (2014). Theoretical optimization of the removal of cryoprotective agents using a dilution-filtration system. *Biomed. Eng. Online*, 13:120.
- [158] Rabin, Y., Steif, P. S., Hess, K. C., Jimenez-Rios, J. L., and Palastro, M. C. (2006). Fracture formation in vitrified thin films of cryoprotectants. *Cryobiology*, 53(1):75–95.
- [159] Raffel, N., Dittrich, R., Orłowski, P., Tischler, H., Söder, S., Erber, R., Hoffmann, I., Beckmann, M. W., and Lotz, L. (2020). Is ovarian tissue transport at supra-zero temperatures compared to body temperature optimal for follicle survival? *In Vivo*, 34(2):533–541.
- [160] Rall, W. F., Mazur, P., and McGrath, J. J. (1983). Depression of the ice-nucleation temperature of rapidly cooled mouse embryos by glycerol and dimethyl sulfoxide. *Biophys. J.*, 41(1):1–12.
- [161] Rizzuto, I., Behrens, R. F., and Smith, L. A. (2019). Risk of ovarian cancer in women treated with ovarian stimulating drugs for infertility. *Cochrane Database Syst. Rev.*, 6:CD008215.
- [162] Rossi, G., Di Nisio, V., Macchiarelli, G., Nottola, S. A., Halvaei, I., De Santis, L., and Cecconi, S. (2019). Technologies for the production of fertilizable mammalian oocytes. *NATO Adv. Sci. Inst. Ser. E Appl. Sci.*, 9(8):1536.

- [163] Rudolph, A. S. and Crowe, J. H. (1985). Membrane stabilization during freezing: the role of two natural cryoprotectants, trehalose and proline. *Cryobiology*, 22(4):367–377.
- [164] Ruppert-Lingham, C. J., Paynter, S. J., Godfrey, J., Fuller, B. J., and Shaw, R. W. (2003). Developmental potential of murine germinal vesicle stage cumulus-oocyte complexes following exposure to dimethylsulphoxide or cryopreservation: loss of membrane integrity of cumulus cells after thawing. *Hum. Reprod.*, 18(2):392–398.
- [165] Salama, M., Isachenko, V., Isachenko, E., Rahimi, G., and Mallmann, P. (2016). Updates in preserving reproductive potential of prepubertal girls with cancer: Systematic review. *Crit. Rev. Oncol. Hematol.*, 103:10–21.
- [166] Salama, M. and Woodruff, T. K. (2019). From bench to bedside: Current developments and future possibilities of artificial human ovary to restore fertility. *Acta Obstet. Gynecol. Scand.*, 98(5):659–664.
- [167] Sales, A. D., Lobo, C. H., Carvalho, A. A., Moura, A. A., and Rodrigues, A. P. R. (2013). Structure, function, and localization of aquaporins: their possible implications on gamete cryopreservation. *Genet. Mol. Res.*, 12(4):6718–6732.
- [168] Schaller, G. and Meyer-Hermann, M. (2006). Continuum versus discrete model: a comparison for multicellular tumour spheroids. *Philos. Trans. A Math. Phys. Eng. Sci.*, 364(1843):1443–1464.
- [169] Schindelin, J., Arganda-Carreras, I., Frise, E., Kaynig, V., Longair, M., Pietzsch, T., Preibisch, S., Rueden, C., Saalfeld, S., Schmid, B., Tinevez, J.-Y., White, D. J., Hartenstein, V., Eliceiri, K., Tomancak, P., and Cardona, A. (2012). Fiji: an open-source platform for biological-image analysis. *Nature Methods*, 9(7):676–682.
- [170] Schreuders, P. D., Diller, K. R., Beaman, Jr, J. J., and Paynter, H. M. (1994). An analysis of coupled multicomponent diffusion in interstitial tissue. *J. Biomech. Eng.*, 116(2):164–171.
- [171] Sciorio, R. and Anderson, R. A. (2020). Fertility preservation and preimplantation genetic assessment for women with breast cancer. *Cryobiology*, 92:1–8.

- [172] Shaik, S. M. and Devireddy, R. (2018). Heat and mass transfer models and measurements for Low-Temperature storage of biological systems. In *Handbook of Thermal Science and Engineering*, pages 2417–2454. Springer International Publishing, Cham.
- [173] Shardt, N., Chen, Z., Yuan, S. C., Wu, K., Laouar, L., Jomha, N. M., and Elliott, J. A. W. (2020). Using engineering models to shorten cryoprotectant loading time for the vitrification of articular cartilage. *Cryobiology*, 92:180–188.
- [174] Smith, K. L., Gracia, C., Sokalska, A., and Moore, H. (2018). Advances in fertility preservation for young women with cancer. *Am Soc Clin Oncol Educ Book*, 38:27–37.
- [175] Smitz, J., Dolmans, M. M., Donnez, J., Fortune, J. E., Hovatta, O., Jewgenow, K., Picton, H. M., Plancha, C., Shea, L. D., Stouffer, R. L., Telfer, E. E., Woodruff, T. K., and Zelinski, M. B. (2010). Current achievements and future research directions in ovarian tissue culture, in vitro follicle development and transplantation: implications for fertility preservation. *Hum. Reprod. Update*, 16(4):395–414.
- [176] Soheilypour, M. and Mofrad, M. R. K. (2018). Agent-Based modeling in molecular systems biology. *Bioessays*, 40(7):1800020.
- [177] Solocinski, J., Osgood, Q., Wang, M., Connolly, A., Menze, M. A., and Chakraborty, N. (2017). Effect of trehalose as an additive to dimethyl sulfoxide solutions on ice formation, cellular viability, and metabolism. *Cryobiology*, 75:134–143.
- [178] Son, W.-Y., Henderson, S., Cohen, Y., Dahan, M., and Buckett, W. (2019). Immature oocyte for fertility preservation. *Front. Endocrinol.*, 10:464.
- [179] Songsasen, N., Ratterree, M. S., VandeVoort, C. A., Pegg, D. E., and Leibo, S. P. (2002). Permeability characteristics and osmotic sensitivity of rhesus monkey (*macaca mulatta*) oocytes. *Hum. Reprod.*, 17(7):1875–1884.
- [180] Stouffer, R. L. and Woodruff, T. K. (2017). Nonhuman primates: A vital model for basic and applied research on female reproduction, prenatal development, and women’s health. *ILAR J.*, 58(2):281–294.

- [181] Taylan, E. and Oktay, K. (2019). Chapter 30 - autologous transplantation of human ovarian tissue. In Leung, P. C. K. and Adashi, E. Y., editors, *The Ovary (Third Edition)*, pages 493–500. Academic Press.
- [182] Telfer, E. E. and Zelinski, M. B. (2013). Ovarian follicle culture: advances and challenges for human and nonhuman primates. *Fertil. Steril.*, 99(6):1523–1533.
- [183] Terren, C., Fransolet, M., Ancion, M., Nisolle, M., and Munaut, C. (2019). Slow freezing versus vitrification of mouse ovaries: from ex vivo analyses to successful pregnancies after Auto-Transplantation. *Sci. Rep.*, 9(1):19668.
- [184] Ting, A. Y., Yeoman, R. R., Campos, J. R., Lawson, M. S., Mullen, S. F., Fahy, G. M., and Zelinski, M. B. (2013). Morphological and functional preservation of pre-antral follicles after vitrification of macaque ovarian tissue in a closed system. *Hum. Reprod.*, 28(5):1267–1279.
- [185] Ting, A. Y., Yeoman, R. R., Lawson, M. S., and Zelinski, M. B. (2011). In vitro development of secondary follicles from cryopreserved rhesus macaque ovarian tissue after slow-rate freeze or vitrification. *Hum. Reprod.*, 26(9):2461–2472.
- [186] Tomao, F., Spinelli, G. P., Panici, P. B., Frati, L., and Tomao, S. (2010). Ovarian function, reproduction and strategies for fertility preservation after breast cancer. *Crit. Rev. Oncol. Hematol.*, 76(1):1–12.
- [187] Troisi, A., Wong, V., and Ratner, M. A. (2005). An agent-based approach for modeling molecular self-organization. *Proc. Natl. Acad. Sci. U. S. A.*, 102(2):255–260.
- [188] Tucker, M., Morton, P., and Liebermann, J. (2004). Human oocyte cryopreservation: a valid alternative to embryo cryopreservation? *Eur. J. Obstet. Gynecol. Reprod. Biol.*, 113 Suppl 1:S24–7.
- [189] Vajta, G. (2012). Vitrification: Research in animal models. In Nagy, Z. P., Varghese, A. C., and Agarwal, A., editors, *Practical Manual of In Vitro Fertilization: Advanced Methods and Novel Devices*, pages 517–521. Springer New York, New York, NY.
- [190] Van den Abbeel, E., Schneider, U., Liu, J., Agca, Y., Critser, J. K., and Van Steirteghem, A. (2007). Osmotic responses and tolerance limits to changes in external osmolalities, and oolemma permeability characteristics, of human in vitro matured MII oocytes. *Hum. Reprod.*, 22(7):1959–1972.

- [191] Van Liedekerke, P., Palm, M. M., Jagiella, N., and Drasdo, D. (2015). Simulating tissue mechanics with agent-based models: concepts, perspectives and some novel results. *Computational Particle Mechanics*, 2(4):401–444.
- [192] Vanderzwalmen, P., Zech, N. H., Ectors, F., Panagiotidis, Y., Papatheodorou, A., Yannis, P., and Wirleitner, B. (2015). Vitrification of oocytes and embryos: Finally a recognized technique, but still a source of concern and debate. In *Vitrification in Assisted Reproduction, Second Edition*, pages 23–34. CRC Press.
- [193] Vandevort, C. A., Shirley, C. R., Hill, D. L., and Leibo, S. P. (2008). Effects of cryoprotectants and cryopreservation on germinal vesicle-stage cumulus-oocyte complexes of rhesus monkeys. *Fertil. Steril.*, 90(3):805–816.
- [194] Waimey, K. E., Smith, B. M., Confino, R., Jeruss, J. S., and Pavone, M. E. (2015). Understanding fertility in young female cancer patients. *J. Womens. Health*, 24(10):812–818.
- [195] Wang, X., Al Naib, A., Sun, D.-W., and Lonergan, P. (2010). Membrane permeability characteristics of bovine oocytes and development of a step-wise cryoprotectant adding and diluting protocol. *Cryobiology*, 61(1):58–65.
- [196] Wang, Z., Butner, J. D., Kerketta, R., Cristini, V., and Deisboeck, T. S. (2015). Simulating cancer growth with multiscale agent-based modeling. *Semin. Cancer Biol.*, 30:70–78.
- [197] Williams, C. J. and Erickson, G. F. (2012). Morphology and physiology of the ovary. In Feingold, K. R., Anawalt, B., Boyce, A., Chrousos, G., de Herder, W. W., Dungan, K., Grossman, A., Hershman, J. M., Hofland, J., Kaltsas, G., Koch, C., Kopp, P., Korbonits, M., McLachlan, R., Morley, J. E., New, M., Purnell, J., Singer, F., Stratakis, C. A., Trencce, D. L., and Wilson, D. P., editors, *Endotext*. MDText.com, Inc., South Dartmouth (MA).
- [198] Wiweko, B., Soebijanto, S., Boediono, A., Mansyur, M., Siregar, N. C., Suryandari, D. A., Aulia, A., Djuwantono, T., and Affandi, B. (2019). Survival of isolated human preantral follicles after vitrification: Analyses of morphology and fas ligand and caspase-3 mRNA expression. *Clin. Exp. Reprod. Med.*, 46(4):152–165.

- [199] Wolfe, J. and Bryant, G. (2001). Cellular cryobiology: thermodynamic and mechanical effects. *Int. J. Refrig*, 24(5):438–450.
- [200] Wolfram, S. (1984). Cellular automata as models of complexity. *Nature*, 311(5985):419–424.
- [201] Wolfram Research, I. (2021). Mathematica 12.3.1. Champaign, IL, 2021.
- [202] Woodruff, T. K. (2008). Making eggs: is it now or later? *Nat. Med.*, 14(11):1190–1191.
- [203] Wowk, B. (2010). Thermodynamic aspects of vitrification. *Cryobiology*, 60(1):11–22.
- [204] Wu, Y.-G., Liu, Y., Zhou, P., Lan, G.-C., Han, D., Miao, D.-Q., and Tan, J.-H. (2007). Selection of oocytes for in vitro maturation by brilliant cresyl blue staining: a study using the mouse model. *Cell Res.*, 17(8):722–731.
- [205] Xiong, M., Lees, M., Cai, W., Zhou, S., and Low, M. Y. H. (2010). Hybrid modelling of crowd simulation. *Procedia Comput. Sci.*, 1(1):57–65.
- [206] Xu, M., Fazleabas, A. T., Shikanov, A., Jackson, E., Barrett, S. L., Hirshfeld-Cytron, J., Kiesewetter, S. E., Shea, L. D., and Woodruff, T. K. (2011). In vitro oocyte maturation and preantral follicle culture from the luteal-phase baboon ovary produce mature oocytes. *Biol. Reprod.*, 84(4):689–697.
- [207] Xu, M., West-Farrell, E. R., Stouffer, R. L., Shea, L. D., Woodruff, T. K., and Zelinski, M. B. (2009). Encapsulated three-dimensional culture supports development of nonhuman primate secondary follicles. *Biol. Reprod.*, 81(3):587–594.
- [208] Xu, X., Cowley, S., Flaim, C. J., James, W., Seymour, L., and Cui, Z. (2010). The roles of apoptotic pathways in the low recovery rate after cryopreservation of dissociated human embryonic stem cells. *Biotechnol. Prog.*, 26(3):827–837.
- [209] Xu, X. and Cui, Z. F. (2003). Modeling of the co-transport of cryoprotective agents in a porous medium as a model tissue. *Biotechnol. Prog.*, 19(3):972–981.
- [210] Yanez, L. Z., Han, J., Behr, B. B., Pera, R. A. R., and Camarillo, D. B. (2016). Human oocyte developmental potential is predicted by mechanical properties within hours after fertilization. *Nat. Commun.*, 7.

- [211] Yang, D. Z., Yang, W., Li, Y., and He, Z. (2013). Progress in understanding human ovarian folliculogenesis and its implications in assisted reproduction. *J. Assist. Reprod. Genet.*, 30(2):213–219.
- [212] Yang, Y., Kanno, C., Sakaguchi, K., Katagiri, S., Yanagawa, Y., and Nagano, M. (2020). Theca cells can support bovine oocyte growth in vitro without the addition of steroid hormones. *Theriogenology*, 142:41–47.
- [213] Yong, K. W., Laouar, L., Elliott, J. A. W., and Jomha, N. M. (2020). Review of non-permeating cryoprotectants as supplements for vitrification of mammalian tissues. *Cryobiology*, 96:1–11.
- [214] Youn, J. R. and Song, Y. S. (2012). Vitrification and devitrification of micro-droplets. *J. Micromech. Microeng.*, 22(11):115018.
- [215] Younis, A. I., Toner, M., Albertini, D. F., and Biggers, J. D. (1996). Cryobiology of non-human primate oocytes. *Hum. Reprod.*, 11(1):156–165.
- [216] Yu, Z.-W. and Quinn, P. J. (1998). Solvation effects of dimethyl sulphoxide on the structure of phospholipid bilayers. *Biophys. Chem.*, 70(1):35–39.
- [217] Zeron, Y., Tomczak, M., Crowe, J., and Arav, A. (2002). The effect of liposomes on thermotropic membrane phase transitions of bovine spermatozoa and oocytes: implications for reducing chilling sensitivity. *Cryobiology*, 45(2):143–152.
- [218] Zhang, M., Oldenhof, H., Sieme, H., and Wolkers, W. F. (2016). Freezing-induced uptake of trehalose into mammalian cells facilitates cryopreservation. *Biochim. Biophys. Acta*, 1858(6):1400–1409.
- [219] Zhang, S. Z. and Chen, G. M. (2002). Analytical solution for the extremums of cell water volume and cell volume using a two-parameter model. *Cryobiology*, 44(3):204–209.
- [220] Zheng, S., Xia, Y., Bidthanapally, A., Badar, F., Ilsar, I., and Duvoisin, N. (2009). Damages to the extracellular matrix in articular cartilage due to cryopreservation by microscopic magnetic resonance imaging and biochemistry. *Magn. Reson. Imaging*, 27(5):648–655.
- [221] Zheng, Y., Zhao, G., Zhang, Y., and Gao, R. (2018). On-chip loading and unloading of cryoprotectants facilitate cell cryopreservation by rapid freezing. *Sens. Actuators B Chem.*, 255:647–656.

# APPENDIX A

**Table A0:** This figure shows the mean max volume change of whole follicle volume as well as the Dunnett test p-value comparing the 1xPBS control for each respective temperature. No max change in whole follicle volume differed significantly from control.

Non-permeating Addition Treatments at 22 °C						
Treatment	Mean Max Volume Change	n	molality (mmol/kg)	molarity (mol/L)	Dunnett Test p-value	
0.5xPBS	0.1379617 ± 0.02739728	3	187	0.1861	0.9967	
1xPBS	0.08215886 ± 0.01532878	3	323	0.3206	X	
2xPBS	0.1337449 ± 0.04931207	6	643	0.6346	0.9946	
5xPBS	0.2810633 ± 0.08843819	5	1600	1.551	0.1581	
1 M Sucrose	0.2432459 ± 0.05724232	7	X	1	0.2824	
Non-permeating Addition Treatments at 37 °C						
Treatment	Mean Max Volume Change	n	molality (mmol/kg)	molarity (mol/L)	Dunnett Test p-value	
0.5xPBS	0.06303601 ± 0.005084989	3	187	0.1861	1.0000	
1xPBS	0.07171233 ± 0.01654794	6	323	0.3206	X	
2xPBS	0.1369124 ± 0.03761273	6	643	0.6346	0.6091	
5xPBS	0.1611896 ± 0.04309305	6	1600	1.551	0.2839	
1 M Sucrose	0.181057 ± 0.02719241	7	X	1	0.1049	
Non-permeating Addition Treatments at 4 °C						
Treatment	Mean Max Volume Change	n	molality (mmol/kg)	molarity (mol/L)	Dunnett Test p-value	
0.5xPBS	0.1045653 ± 0.01889196	11	187	0.1861	0.2838	
1xPBS	0.05141731 ± 0.02191832	10	323	0.3206	X	
2xPBS	0.1080699 ± 0.02499451	11	643	0.6346	0.2374	
5xPBS	0.1167223 ± 0.04577974	5	1600	1.551	0.2987	
Permeating Addition Treatments at 22 °C						
Treatment	Mean Max Volume Change	n	molality (mmol/kg)	molarity (mol/L)	Dunnett Test p-value	
15% GLY	0.2733577 ± 0.06020668	6	2158	2.2	0.1629	
15% EG	0.2206745 ± 0.03328571	11	2503	1.868	0.3723	
15% GLY & 15% EG	0.2469055 ± 0.06542084	8	4788	4.04	0.2456	
Permeating Removal Treatments at 22 °C						
Treatment	Mean Max Volume Change	n	molality (mmol/kg)	molarity (mol/L)	Dunnett Test p-value	
15% GLY to HM	0.1738507 ± 0.03128415	6	2158	2.2	0.8365	
15% EG to HM	0.1017561 ±	5	2503	1.868	1.0000	
15% GLY & 15% EG to HM	0.1745486 ± 0.02811197	8	4788	4.04	0.8003	
Permeating Addition Treatments at 37 °C						
Treatment	Mean Max Volume Change	n	molality (mmol/kg)	molarity (mol/L)	Dunnett Test p-value	
15% GLY	0.1728163 ± 0.03590019	6	2158	2.2	0.1796	
15% EG	0.1722034 ± 0.05148093	4	2503	1.868	0.2796	
15% GLY & 15% EG	0.2120962 ± 0.03010522	3	4788	4.04	0.0994	
Non-permeating Removal Treatments at 22 °C						
Treatment	Mean Max Volume Change	n	molality (mmol/kg)	molarity (mol/L)	Dunnett Test p-value	
1 M Sucrose to HM	0.09434567 ± 0.02323709	6	X	1	1.0000	